Title

VCCI: A Potent CC Chemokine Inhibitor and A Silk Fibroin-Based Scaffold Study

Permalink

Author

Guan, Wenyan

Publication Date

2024

Peer reviewed|Thesis/dissertation

UNIVERSITY OF CALIFORNIA, MERCED

VCCI: A Potent CC Chemokine Inhibitor
and
A Silk Fibroin-Based Scaffold Study

A dissertation submitted in partial satisfaction of the

requirements for the degree of

Doctor of Philosophy

in

Materials and Biomaterials Science and Engineering

by

Wenyan Guan

Committee in charge:

Professor Kara E. McCloskey, Chair of Advisory Committee

Professor Michael E. Colvin

Professor Jennifer Lu

Professor Patricia J. LiWang, Supervisor

2024

Copyright

The Dissertation of Wenyan Guan is approved, and it is acceptable in quality and form
for publication on microfilm and electronically:

_____   Date _____

Professor Michael E. Colvin

_____   Date _____

Professor Jennifer Lu

Supervisor   _____   Date _____

Professor Patricia J. LiWang

Chair   _____   Date _____

Professor Kara E. McCloskey

University of California, Merced

2024

DEDICATION

To my supervisor, my lab mates, my friends and my family members that have supported me in this academic path.

Table of Contents

I. List of Abbreviations

BLI: biolayer interferometry

CBP: chemokine-binding proteins

CCL17: CC chemokine ligand 17

DTT: dithiothreitol

EDTA: ethylenediaminetetraacetic acid

EK: enterokinase

GAGs: glycosoaminoglycans

Grft: Griffithsin

GSH: reduced glutathione

GSSG: oxidized glutathione

His_6-Tag: hexahistidine tag

HIV: human immunodeficiency virus

HPMC: hydroxypropyl methylcellulose

HuAoSMC: human aortic smooth muscle cells

HUVEC: human umbilical vein endothelial cells

IPTG: isopropyl β-d-1-thiogalactopyranoside

LB: Luria broth

MD: molecular dynamics

NaCl: sodium chloride

NaOAc: sodium acetate

NaPi: sodium phosphate

NHLF: normal human lung fibroblasts

Ni-NTA: nickel-nitrilotriacetic acid

OD: optical density

PEG: polyethylene glycol

RA: rheumatoid arthritis

SDS-PAGE: sodium dodecyl sulfate polyacrylamide gel electrophoresis

SF: silk fibroin

TARC: thymus and activation-regulated chemokine

TBI: traumatic brain injury

TCA: trichloroacetic acid

Trx: thioredoxin

Trx-KaiC: residues 1–247 of KaiC from Thermosynechococcus elongatus, with mutations Arg41Ala and Lys173Ala, and an N-terminal thioredoxin fusion tag

Trx-vMIP: thioredoxin-vMIP-II

vCCI: viral CC chemokine inhibitor

vMIP-II: Herpesvirus-8 macrophage inflammatory protein-II

II. List of Figures

III. List of Tables

IV. Acknowledgments

V. Vita for Wenyan Guan

Education:

PhD & MS **University of California, Merced**

Materials and Biomaterials Science and Engineering

MS **East China University of Science and Technology**

Master of Bioengineering

BS **Southwest University for Nationalities**

Bachelor of Applied Chemistry

List of Publications:

1. **Guan W**, Zhang N, Bains A, Martinez A, LiWang PJ. Sustained Delivery of the Antiviral Protein Griffithsin and Its Adhesion to a Biological Surface by a Silk Fibroin Scaffold. Materials 2023;16:5547. https://doi.org/10.3390/ma16165547.
2. **Guan W**, Zhang N, Bains A, Sadqi M, Dupureur CM, LiWang PJ. Efficient production of fluorophore-labeled CC chemokines for biophysical studies using recombinant enterokinase and recombinant sortase. Biopolymers 2023:e23557. https://doi.org/10.1002/BIP.23557.
3. **Guan W**, Rodriguez AM, Guerrero R, Stark LE, Colvin ME, LiWang PJ. The interaction of CC chemokine binding protein vCCI with CCL17(TARC). BpJ 2023;122:42a. https://doi.org/10.1016/J.BPJ.2022.11.439.
4. Zhang N, **Guan W**, Cui S, Ai N. Crowded environments tune the fold-switching in metamorphic proteins. Communications Chemistry 2023 6:1 2023;6:1–7. https://doi.org/10.1038/s42004-023-00909-2.
5. Bains A, **Guan W**, LiWang PJ. The Effect of Select SARS-CoV-2 N-Linked Glycan and Variant of Concern Spike Protein Mutations on C-Type Lectin-Receptor-Mediated Infection. Viruses 2023, Vol 15, Page 1901 2023;15:1901. https://doi.org/10.3390/V15091901.
6. Bains A, Fischer K, **Guan W**, LiWang PJ. The Antiviral Activity of The Lectin Griffithsin Against SARS-CoV-2 Is Enhanced by The Presence Of Structural Proteins. Viruses 2023, Vol 15, Page 2452 2023;15:2452. https://doi.org/10.3390/V15122452.
7. Stark LE, **Guan W**, Colvin ME, LiWang PJ. The binding and specificity of chemokine binding proteins, through the lens of experiment and computation. Biomed J 2022;45:439–53. https://doi.org/10.1016/J.BJ.2021.07.004.
8. LiWang PJ, **Guan W**, Stark L, Showalter L, Colvin M. vCCI:Chemokine Interactions: Experimental Biochemistry Meets Computational Prediction. The FASEB Journal 2020;34:1–1. https://doi.org/10.1096/FASEBJ.2020.34.S1.07398.

Awards and Fellowships:

1. University of California, Merced, Outstanding Graduate Student Award in the MCB Department (2023-2024)
2. University of California, Merced, Dean's Dissertation Fellowship (2024)
3. The Biophysics Society Annual Meeting, Student Research Achievement Award (SRAA), Poster Competition Winner (2023)
4. University of California, Merced, MBSE Travel Fellowship (2023)
5. University of California, Merced, GSA Travel Award Fellowship (2023)
6. University of California, Merced, The Center for Advancing Diversity in Engineering Teaching Fellowship (2023)
7. University of California, Merced, The Center for Advancing Diversity in Engineering Teaching Fellowship (2022)
8. University of California, Merced, Principles of Pedagogy Certificate (2021)
9. University of California, Merced, MBSE Summer Fellowship (2020)
10. University of California, Merced, MBSE Travel Fellowship (2020)

VI. Abstract

vCCI: A potent CC chemokine inhibitor

and

Silk fibroin-based scaffolds study

Wenyan Guan

Doctor of Philosophy

University of California, Merced

2024

Supervisor: Prof. Patricia J. LiWang

Inflammation occurs when chemokines are secreted at a site of injury or infection, mediating a buildup of immune cells. Therefore, inhibiting chemokines in some cases could be an appealing target to control inflammation. Many viruses have evolved strategies to subvert the human chemokine system by producing chemokine binding proteins. Among them, poxviruses encode vCCI (viral CC chemokine inhibitor), which has been shown to bind more than 20 CC chemokines with high affinity. Therefore, understanding the mechanism of the high binding affinity between vCCI and CC chemokines could pave a way to develop vCCI as a new therapeutic candidate to treat inflammation related disease. In collaboration with the Prof. Michael Colvin group, combining an experimental approach and computational methodology, to unveil the possible key residues in the function of interaction between vCCI and chemokines, our work shows vCCI Y80, E143, and I184 residues are important for its binding to a chemokine vMIP-II (vCCL2). The vCCI mutation Y80R showed a loss of binding of 55 fold compared to the wild type of protein in BLI experiments, while E143K, I184R mutants decreased binding affinity of 37 and 25 fold respectively. We also found some key residues (G17, V44, Q45) of TARC (CCL17) involved in the interaction with vCCI. Highest affinity was achieved with the triple mutant CCL17 G17R/V44K/Q45R, which gave a Kd of 0.25 ± 0.13 µM for the vCCI:CCL17 variant complex, a 68 fold improvement in affinity compared to the complex with wild type CCL17.

Silk fibroin (SF or silk in abbreviation) derived from the species *Bombyx mori* has been recognized as a material for biomedical sutures for centuries. With excellent biocompatibility, biodegradability, and sufficient supply, silk fibroin has become a popular biomaterial in tissue engineering, drug delivery, and surgery. In addition, silk fibroin can be developed into a variety of shapes with multiple structures, such as 3D porous scaffolds, films, particulates, fibers, needle patches, etc. In this study, we investigated improving the adhesive property of SF scaffold to the wet tissue with the addition of polyethylene glycol (PEG) and glycerol, and realized the sustained release of an anti-HIV protein Griffithsin.

Chapter 1

Introduction

1.1 CC chemokines and vCCI

1.1.1 Introduction of CC chemokines

The human immune system plays a critical role in protecting us from harmful pathogens, including bacteria, viruses, fungi, and parasites, and battling against harmful cells, like cancer cells. It consists of a complex network of leukocytes, cytokines, tissues, and organs that work together to fight against infections and diseases. One of the most important processes engaged in the function of immune response is the migration of leukocytes to the infection sites [1]. The movement of leukocytes is mediated by a gradient of chemokines (Figure 1.1). Chemokines are chemotactic cytokines secreted by immune cells at the beginning of infection or injury, and leukocytes move up the chemokine gradient toward the site of injury or infection [2]. During the initiation of the infection, the chemokines interact with endothelial cells to trigger the secretion of more adhesion proteins and chemokines to facilitate the attachment of passing by leukocytes to the endothelial cell surface [3].

Chemokines bind relatively weakly with glycosoaminoglycans (GAGs) on the surface of the endothelial cells, and this chemokine retention increases the concentration of the localized chemokines in the vicinity of the infection or injury sites, which increases the chance of interaction between chemokines and leukocytes when they are passing the endothelium surface [4]. Chemokines bind tighter with their cognate G protein-coupled receptors on the surface of leukocytes compared with the

Figure 1.1 Chemokines induced the migration of leukocytes

Chemokines setting up a concentration gradient to guide leukocytes toward infection/tissue damage sites.

interactions with GAGs [5]. Once the chemokine binds to the receptors on leukocytes, it can lead to a conformational change of the receptor which triggers the activation of the heterotrimeric G-protein and leads to a downstream signal activation of phospholipase C (PLC) [5–7]. Then phosphatidylinositol 4,5-bisphosphate (PIP2) will be hydrolyzed by PLC and generate inositol 1,4,5-trisphosphate (IP3) to signal the migration of Ca^{2+} from the endoplasmic reticulum to an intracellular location which further activates the protein kinase

C (PKC) [8]. The PKC activates several GTPases related to the activation of actin and the release of Ca^{2+} activates the myosin, which results in the migration of leukocytes to move up the increasing chemokine gradient toward the site of infection or injury to battle against the pathogens [9,10].

The chemokine family is subdivided into four subfamilies: C, CC, CXC, CX3C, where "C" represents a cysteine residue near the N-terminus which can form a disulfide bond with another cysteine, and "X" means any amino acid between the cysteine residues. Among these, CC and CXC are the main and well-classified families of chemokines. Chemokines were originally named in relation to their functions. For example, TARC, stands for Thymus and Activation-Regulated Chemokine. Currently, however, there is an official naming system for chemokines which have chemokines name followed by "ligand" and a number, such as CCL17 (CC chemokine ligand 17, called TARC) [11]. Therefore, most chemokines have both a common name and an official nomenclature name.

Though chemokines function as the guiders to help leukocytes to move towards damaged tissues to keep the body healthy, disordered expression of chemokines can result in immune related diseases (Figure 1.2). For example, over expression of chemokines will cause an influx of immune cells, contributing to injury in damaged parts, as in traumatic brain injury (TBI). CC chemokines have been reported to be involved in a variety of inflammation-related diseases, especially chronic inflammation, such as rheumatoid arthritis (RA), asthma, crohn's disease, adipose inflammation, diabetes, atherosclerosis, multiple sclerosis, neuropathic pain, insulin resistance, etc [12]. In addition, a CC chemokine receptor, CCR5, plays a key role for HIV infection at the initial stage [13,14]. Studying CC chemokines will help the understanding of the role of these chemokines and chemokine receptors in the immune system.
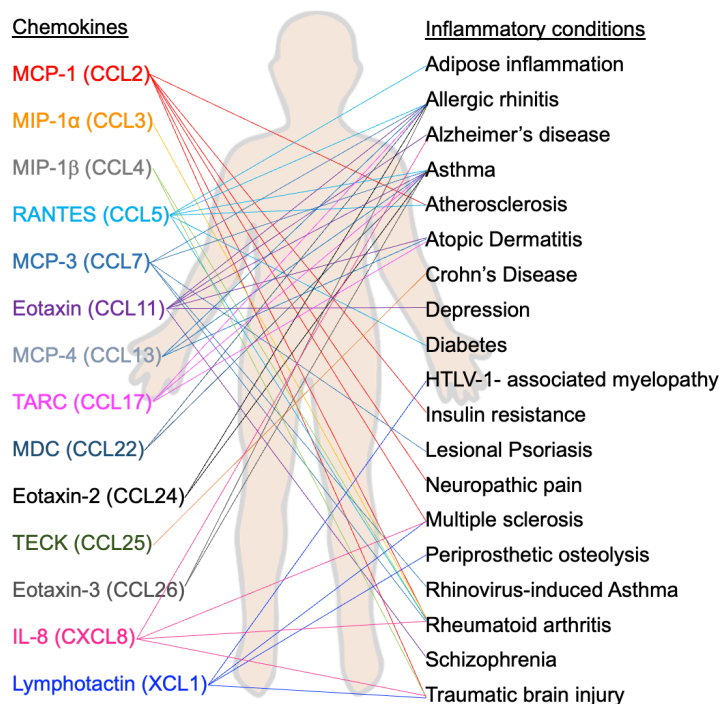
Figure 1.2 Chemokine induced inflammation

Many of chemokines cause the inflammation and healthy issues.

1.1.2 Introduction of chemokine binding protein

As part of viral evasion strategies, many viruses have evolved to cause the secretion of chemokine binding proteins to subvert the normal chemokine signal pathways, reducing leukocyte recruitment and activation at the site of infection [15]. There are three

classes of viral chemokine binding proteins: chemokine receptor homologs which bind a chemokine and prevent its interaction with its natural receptor, chemokine homologs which bind a receptor and block binding by the natural chemokine ligand, and chemokine-binding proteins (CBPs) which bind the chemokine and prevent it from binding to its receptor and/or GAGs [16]. CBPs have 3 classes: Class I which non-specifically binds all chemokines with a low affinity [17], Class II which binds CC chemokines [18,19], and Class III which binds C, CXC, and CX3C chemokines [20]. Among them, Class II CBPs specifically bind CC chemokines with high affinity which makes them potentially good therapeutic candidates targeting CC chemokine-related inflammation diseases.

One of the Class II CBP's is Viral CC chemokine inhibitor (vCCI, also known as 35K) which is a virally produced protein (originally discovered from poxvirus) that has been reported to bind more than eighty CC chemokines of various species, and about twenty of them with high affinity [6, 7]. Therefore, vCCI has been broadly studied as an anti-CC chemokine therapeutic candidate in inflammation related diseases [8-11] and making the mechanism behind its binding to the chemokines of great interest.
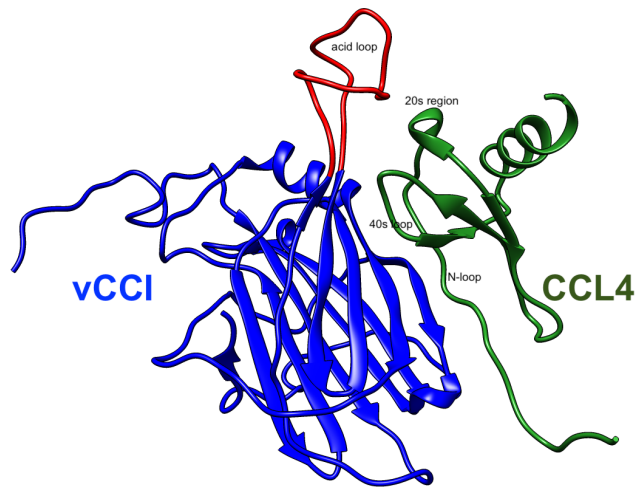
Figure 1.3 vCCI:CCL4 complex structure

The vCCI is on the left colored blue and its acidic loop is shown on red. The CCL4 is on the right colored with green. (PDB ID: 2ffk)

In 1999, Carfí et all first reported the structure of vCCI, showing contains a β-sandwich topology with one of the β-sheets having a strong negative charge; they hypothesized that it might interact with positively charged CC-chemokines [21]. In 2006, our group reported the structure of vCCI (encoded by rabbitpox virus rabbitpox virus) in complex with a chemokine, CCL4, through NMR experimental data analysis (Figure 1.3) [22]. vCCI has 11 β strands, one α helix, and several loops. The β strands form two β sheets, β sheet I (β5, β6, β1, β9, β10 and β11) and β sheet II (β2, β3, β4, β7 and β8). Between β2 and β3, there is a conserved loop (acidic loop in short) containing more than 50% negatively charged residues (Asp and Glu) which acts together with partially negatively charged β sheet II to interact with a chemokine's basic residues on the N-loop, 20s region and 40s loop, blocking the chemokine binding to its receptor and GAGs in order to reduce the inflammation caused by the expression of the chemokine [19].

1.2 Silk scaffold introduction

Silk is one of the most abundant and economical biomaterials in nature. More than 120,000 tons of Bombyx mori silkworm silk ("silk" in short in this thesis) are produced worldwide every year, and the main manufactures are in China, India, and Japan [23]. Additionally, owing to prominent biocompatibility, biodegradability, and mechanical properties, silk has been used as a surgical suture since 150 ACE [24]. Current US FDA approved clinical usage of silk fibroin biomedical materials includes surgical mesh called a SERI Surgical Scaffold for soft tissue support and repair, silk sutures, and silk clothing to treat dermatological conditions. Also, in China, the CFDA approved a silk fibroin film, Sidaiyi, for wound healing [25]. Moreover, with special hierarchical structure and versatility, many scientists have been investigating using silk as a model to design novel materials with customized properties and specific applications, including drug delivery vehicle/system [26], tissue engineering applications [27], biosensors [28], wearable electronic devices [29], and water ultrafiltration systems [30].
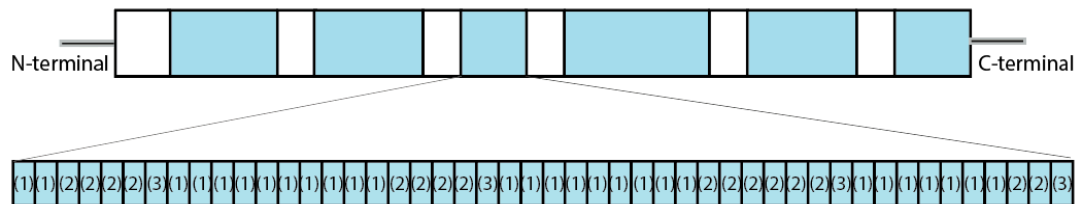
Figure 1.4 Bombyx mori silk fibroin heavy chain

The blue regions demonstrate repetitive blocks, while white regions represent amorphous regions. (1) highly repetitive GAGAGS; (2) a less repetitive sequence containing hydrophobic and/or aromatic residues, including GAGAGY, GAGAGV, GAGAGVGY; (3) like (1) but having AAS motif at the C-terminus.

1.2.1 Composition and structure

Silk's advantageous properties are attributed to its exclusive structure and components. Silk is composed of two primary proteins: silk fibroin (about 75%) and sericin (about 25%). Fibroin is the main component of silk and acts as the inner core (which provides mechanical strength), while sericin is the outer glue-like coating. Each silk fiber is composed of two silk fibroin filaments coated with sericin [31]. Silk fibroin is a very large protein, which could be subdivided into light chain (about 26 kDa), heavy chain (about 390 kDa), and glycoprotein P25 (about 25 kDa) [32]. The heavy chain and light chain are linked by a single disulfide bond at the C-terminus. P25 associated with the heavy-light chain complex via hydrophobic interactions, and the molar ratio of heavy chain, light chain, and P25 is 6:6:1 [33–35].

Yamada et al found that the silk fibroin heavy chain N terminus has two peptides, VITTDSDGNE and NINDFDED, which are thought to be able to promote fibroblast growth [36]. The mechanical properties of silk fibroin are due to the anti-parallel β sheets' arrangement of the heavy chain, which is comprised of 11 short hydrophilic regions and 12 hydrophobic blocks. The hydrophobic blocks mainly are composed of glycine-X (GX) repeats where X represents alanine (A) (65%), serine(S) (23%), or tyrosine(Y) (9%) [10]. The GX blocks could be further divided into three groups: (1) highly repetitive GAGAGS building blocks that contributes to the crystalline regions; (2) a less repetitive sequence

4

containing hydrophobic and/or aromatic residues, including GAGAGY, GAGAGV, GAGAGVGY, forming semi-crystalline regions (Figure 1.4); (3) like (1) but having AAS motif at the C-terminus and may function as sheet-breaking [32,37].

The GX repeating units form anti-parallel β sheets through intra- and inter-molecular hydrogen bonds, contributing to the generation of nano β sheet crystallites [38]. The nano β sheet crystallites are connected by amorphous peptide chains and cross-linked via hydrophobic interactions and hydrogen bonds, forming nanofibrils (Figure 1.5) [39]. Finally, a bundle of nanofibrils form silk fibers with 30-35 nm in diameter [39]. The macroscopic property of silk is determined by the three-dimensional hierarchical structures of crystal networks. The crystalline network consists of fibrils and "nodes" (individual crystal networks), and multi-domain networks of silk fiber, and the mechanical strength is determined by the interactions between domains, nodes, and synergy between the different levels of networks [39]. The multi-domain systems with weak or zero domain-domain interactions have lower mechanical properties, such as silk hydrogel. The multi-domain systems with strong inter-domain interactions have stronger hierarchical networks, contributing to stronger mechanical properties [39].

Fiber   Nano-fibril   Nano β-crystallite
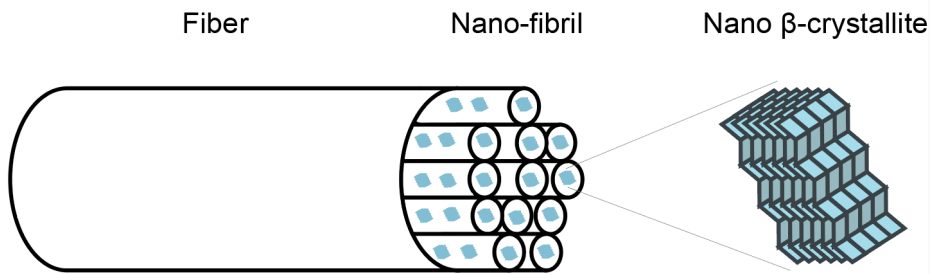
Figure 1.5 Silk fibers are composed of interlocking nanofibrils

Each nanofibril is consisted of nano β sheet crystallites which are connected by amorphous peptide chains. The overall hierarchical structure contributes to the unique biophysical properties of silk.

Silk fibroin modification is another way to adjust its properties which can be achieved via solvent or chemical treatment. Solvent treatment can adjust the secondary structural of silk fibroin. For example, immersion in alcohols or kosmotropic salts, or water annealing can increase β-sheets ratio and decrease the α-helix content. The increase of silk fibroin β-sheet crystalline structure could decrease its water solubility and enhance its aqueous stability of fibroin architecture [40]. Methanol treatment is frequently used to generate crystalline architectures, while water annealing could produce flexible matrix with reduced β-sheet content [41]. Chemical modification can improve and/or expand the functionalities of silk fibroin and sericin, including chemical modification of amino acid residues and insertion of chemical species [42]. For example, covalently attaching integrin-recognition sequence Arginine-Glycine-Aspartate (RGD) and parathyroid hormone (PTH) can improve cell compatibility of silk, and the modified silk fibroin shows higher osteoblast adhesion and overall calcification in vitro [43]. Treatment via diazonium coupling can covert tyrosine residues on silk fibroin into hydrophilic groups (such as carboxylic acid, ketones, sulfonic acid, and amines) to facilitate cell adhesion and proliferation, and the human bone marrow-derived mesenchymal stem cells (hMSCs) show a cellular growth rate that depends on scaffold hydrophilicity [44].

1.2.2 Silk fibroin- based materials

Owning to silk fibroin's hemostatic properties, low inflammatory potential, permeability to water and oxygen, and bacterial barrier functionality, silk fibroin-based biomaterials have been studied in the skin repair and regeneration field for decades. Current US FDA approved clinical usage of silk fibroin biomedical materials includes surgical mesh called a SERI Surgical Scaffold for soft tissue support and repair, silk sutures, and silk clothing to treat dermatological conditions. Also, in China the FDA approved a silk fibroin film, Sidaiyi, for wound healing [25].

Silk fibroin solution has been studied in preclinical animal models of eye disease, such as dry eye and corneal injuries, and it shows that silk fibroin treatment can (a) inhibit the detachment of corneal epithelial cells, (b) increase the number of conjunctive goblet cells, and (c) inhibit inflammatory factors in the lacrimal gland of the eye [45,46]. Further, the silk fibroin films support the adhesion and growth of human corneal epithelial cells [47].

There is an increasing investigating of silk fibroin-based scaffolds for use in the bone tissue engineering field. Porous scaffolds, 3D printing scaffolds, hydrogels, and films are the common forms for bone tissue engineering studies. Growth factors, drugs, and different stem cells have been incorporated into silk fibroin-based scaffolds to facilitate bone formation [48].

Silk fibroin microneedle patches are a painless transdermal drug delivery method gaining increased attention. The tip of a microneedle has quick-dissolve abilities, while the pedestal of the microneedles could release a drug continuously through the micropore, achieving a sustained release effect over time [48,49].

1.2.3 Silk-based scaffold for drug delivery

Silk fibroin has prominent mechanical properties, biocompatibility, slow degradation, moderate processing conditions, and the ability to maintain the stability and activity of biological molecules in its matrix, making it a promising drug delivery vehicle. One of the main drug release mechanisms from silk fibroin matrices is diffusion, and the speed of releasing is dependent on the treatment used to process the silk and the chemical properties of the drug [50]. Proteins and small molecules could be formulated into silk fibroin scaffolds, such as films, sponges, and microneedle patches, and released by passive diffusion.

Zhang et al showed that protein HIV inhibitors, 5P12-RANTES, 5P12-RANTES-L-C37, Grft, and Grft-L-C37, can be formulated into SF disks and remain functional for 14 months at 50°C and sustained release of functional inhibitor Grft for 4 weeks [51]. The SF disks showed strong inhibition against HIV in PBMC and human colorectal and cervical tissue explants without triggering inflammatory cytokine secretion. Crakes et al further explored the effect of SF disks on the mucosal tissues, cervical and colorectal, and the results showed effective Grft release and retention in mucosal tissues to protect against HIV without causing any inflammatory responses or changes in local microbiota [52]. Lammel et al reported silk fibroin particles can be applied to deliver small molecule model drugs, and they demonstrated that the secondary structure of the particles, crystalline or less crystalline directly affect the release kinetics of the drug [26].

Furthermore, drugs can covalently attach to silk fibroin/sericin matrix to decrease their diffusion rate and increase drugs' stability. For example, L-asparaginase covalently

linked with silk fibroin scaffold by glutaraldehyde showed an increased activity and reduced immunogenicity than L-asparaginase alone [50]. Zhang et al covalently attached insulin onto sericin peptides with cross-linking reagent glutaraldehyde, and the stability in vitro and in vivo of insulin was enhanced more than twice as they covalently linked insulin to silk sericin; the immunogenicity and antigenicity were not observed in both rabbits and mice [53].

1.3 Chapter introduction

In Chapter 2, "The binding and specificity of chemokine binding proteins, through the lens of experiment and computation", we describe the critical role of chemokines for immune function, and many viruses as well as parasitic arthropods have evolved to secrete proteins to bind chemokines, mimic chemokines, or produce analogs of chemokine receptors in order to disrupt natural chemokines' function and bypass the human immune response. The main content of this chapter is summarizing the structural properties of a diverse set of CBPs produced by mammalian viruses, such as vCCI, A41, ORFV CKBP, SECRET Domain, M3, R17, Evasins, M-T1 and M-T7. Based on the information above, we describe the current and emerging capabilities of combining computational simulation, structural analysis, and biochemical/biophysical experimentation to understand, and possibly re-engineer, protein-protein interactions. This article was published in Biomedical Journal in 2021 [19].

In Chapter 3, "Efficient production of fluorophore-labeled CC chemokines for biophysical studies using recombinant enterokinase and recombinant sortase", we carry out experiments to measure the binding affinity vCCI and chemokine by a biophysical technique, namely a fluorescence anisotropy assay. We first designed a fusion-tagged (thioredoxin) chemokine gene and expressed it in *Escherichia coli*. After purification of the protein, the N-terminal fusion partner is cleaved by a lab-produced enterokinase, and then covalently labeled with a fluorophore mediated by the lab-produced sortase A enzyme. The process of producing enterokinase and sortase A enzyme used in this research reduces the need for expensive commercial enzymatic reagents. This work demonstrates an efficient method of production and fluorescent labeling of chemokines for study across a broad range of concentrations. This work was published in Biopolymers in 2023 [54].

In Chapter 4, "A combined molecular dynamics and biophysical approach to studying the chemokine binding properties of viral protein vCCI", we studied the key residues involved in the interaction between vCCI and chemokine via the analysis of the data of fluorescence anisotropy, NMR, biolayer interferometry (BLI), and molecular dynamics. We used vMIP-II, a virally expressed chemokine homolog, as a binding partner for vCCI since it has high affinity for vCCI [55]. Our results show that despite previous reports of poor binding, the Y80A vCCI variant still retains sub-nanomolar binding. Other mutations predicted to impair binding (Y80R, E143K, I184R) did indeed show a loss of binding compared to the wild type protein in BLI experiments, although each still bound the chemokine at nanomolar levels. Only a combination of mutations, rather than a single variant, was able to fully abrogate binding to vMIP-II. Overall, this work is a combination of biophysical techniques and molecular dynamics to pinpoint sites in vCCI that are involved in chemokine binding, including those that are indirectly involved due to allowing control of the active site loop of vCCI. This work is useful as part of a strategy to understand and design specific chemokine binding ability. This phase of the work has finished, and the manuscript is in preparation.

In Chapter 5, "Design of higher affinity interaction between CC chemokine binding protein vCCI and CCL17/TARC", we investigate the interaction between vCCI and CCL17 which has been reported to only make a low-affinity complex [55]. We did an analysis of the molecular dynamics simulation of a model of the vCCI:CCL17 complex, along with a sequence comparison of CCL17 with other chemokines, and found several sites of interest (G17, V44, and Q45) in CCL17. These were judged to be important to binding vCCI such that their mutation to a more suitable amino acid was hypothesized to improve binding to vCCI. These sites in CCL17 were mutated and the proteins expressed and purified. Highest affinity was achieved with the triple mutant CCL17 G17R/V44K/Q45R, which gave a Kd of 0.25 ± 0.13 μM for the vCCI:CCL17 variant complex, a 68 fold improvement in affinity compared to the complex with wild type CCL17. It was found that single point mutants V44K and Q45R modestly increased binding affinity to vCCI, and their combination into a double mutant provided further improved affinity. A final quadruple mutant CCL17 G17R/V44K/Q45R/R57W showed high affinity, but did not improve upon the triple mutant. Overall, this work shows that structural analysis can lead to mutations that improve the binding of the vCCI:CCL17 complex, which could lead to development of specificity in vCCI binding that could be useful as an anti-inflammatory therapy. This work has finished, and the manuscript is in preparation.

In chapter 6, "Sustained Delivery of the Antiviral Protein Griffithsin and Its Adhesion to a Biological Surface by a Silk Fibroin Scaffold", we improved the adhesive property of silk-based scaffold on wet tissue and realized the sustained release of the HIV-1 inhibitor, Griffithsin (Grft) (Figure 1.6). We show that silk fibroin can be formulated with adhesive properties using the nontoxic polymer hydroxypropyl methylcellulose (HPMC) and glycerol, and that the resulting silk scaffold can both adhere to biological surfaces and release Grft over the course of at least one week. This work advances the possible use of silk fibroin as an anti-viral insertable device to prevent infection by sexually transmitted viruses, including HIV-1.
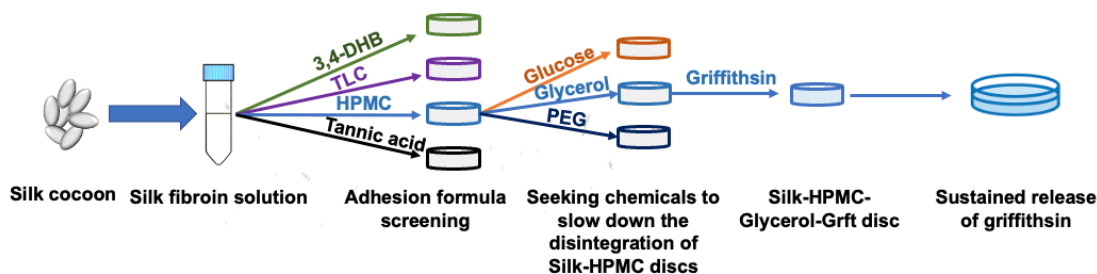
Figure 1.6 Improving silk-based scaffold's adhesion for drug delivery

Screening the best candidate to improve silk-based scaffold's adhesion on wet tissue and realize sustained release of Grft.

Chapter 2

The Binding and Specificity of Chemokine Binding Proteins, Through The Lens of Experiment and Computation

2.1 Abstract

Chemokines are small proteins that are critical for immune function, being primarily responsible for the activation and chemotaxis of leukocytes. As such, many viruses, as well as parasitic arthropods, have evolved systems to counteract chemokine function in order to maintain virulence, such as binding chemokines, mimicking chemokines, or producing analogs of transmembrane chemokine receptors that strongly bind their targets. The focus of this review is the large group of chemokine binding proteins (CBP) with an emphasis on those produced by mammalian viruses. Because many chemokines mediate inflammation, these CBPs could possibly be used pharmaceutically as anti-inflammatory agents. In this review, we summarize the structural properties of a diverse set of CBP and describe in detail the chemokine binding properties of the poxvirus-encoded CBP called vCCI (viral CC Chemokine Inhibitor). Finally, we describe the current and emerging capabilities of combining computational simulation, structural analysis, and biochemical/biophysical experimentation to understand, and possibly re-engineer, protein-protein interactions.

2.2 Introduction

This is an exciting time in molecular immunology. Increasing capabilities in areas like structural biology and molecular simulation are providing powerful new scientific tools for deciphering the immune system. At the same time, there is a critical need for new therapies against emerging infectious diseases, such as that caused by the virus SARS-CoV-2, and other diseases associated with a dysregulated immune response. This review describes current results and future directions in the study of the molecular function of the soluble chemokine binding proteins (CBP, sometimes called CKBP), with a focus on the poxvirus-encoded protein vCCI (viral CC Chemokine Inhibitor). As described below, these proteins are one component in the strategy used by mammalian viruses and various organisms to suppress their host's immune response. These proteins have the interesting property that they bind with high specificity to entire classes of immune-signaling chemokines. Elucidating how these proteins specifically recognize their various chemokine ligands could allow the re-engineering of CBP for use as therapeutics.

This review begins by giving a brief background on chemokines and the different tools that viruses use to reduce the infected host's chemokine effectiveness. Then we describe the structural features of a range of CBP that provide hints to the common structural elements that mediate chemokine binding. This section includes a tabular summary of the properties of these proteins and figures highlighting their key features.

After that summary, we describe in detail the chemokine-binding properties of rabbitpox protein vCCI as an archetype of the viral CBP. We also describe how molecular simulations, structural analysis, mutation studies, and biochemical/biophysical assays can be combined to elucidate a detailed map of how the structural features of vCCI determine

its chemokine binding specificity. Finally, we end with a look forward to how this structural information can be used to reengineer CBP or chemokines for specific biomedical or biotechnological applications.

2.3 Background

The immune system serves a variety of functions in protecting human health, and a critical aspect of the immune response is the activation and chemotaxis of immune cells, as mediated by chemokines. When injury or infection occurs, chemokines are secreted, producing an inflammatory immune response. Chemokines are small proteins (usually about 70 amino acids) that tightly bind their cognate 7-transmembrane receptor and are also able to bind glycosaminoglycans (GAGs). Their mode of action is generally to first bind GAGs on the endothelial surface, setting up a chemokine concentration gradient. They then bind tightly to their respective receptors on the surface of passing leukocytes, which are activated by this binding event. Chemokine-receptor interactions, including those involved in non-inflammatory processes, have been recently reviewed[56,57].

There are four subfamilies of chemokines, totaling about 50 members, named based on the placement of conserved cysteines near the N-terminus of the protein (CC, CXC, CX3C, and C), with chemokines from all subfamilies having the same overall fold.
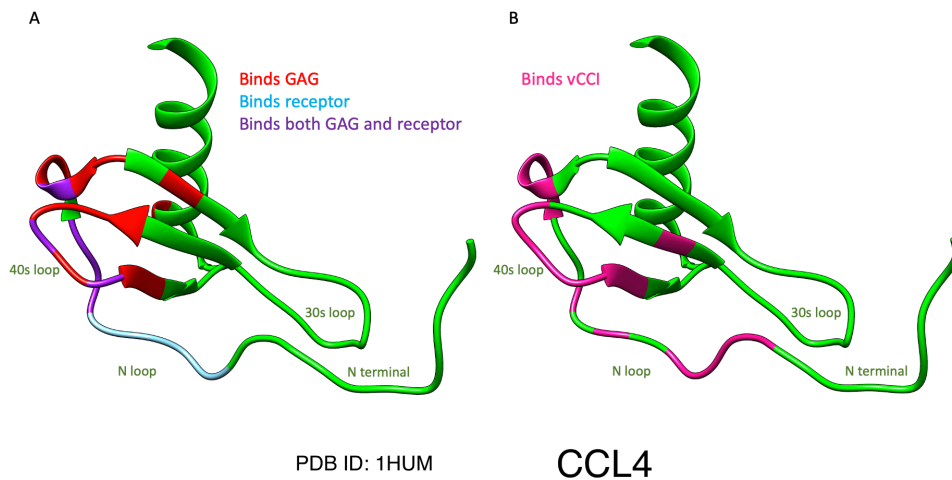
Figure 2.1 vCCI binding to CC chemokines shows significant overlap with the chemokine's natural binding contacts

A. Binding contacts made by CC chemokines with the chemokine receptor and with glycosaminoglycans (GAGs). The CC chemokine CCL4 (PDB ID: 1HUM) is used as a typical example. The chemokine is shown in green, with receptor binding contacts shown in light blue. GAG contacts are shown in red. Amino acids that are used both to bind receptors and to bind GAGs are shown in purple. With regard to receptor binding, note that after the initial binding event (using light blue and purple residues), the N-terminus of the chemokine is used to contact the transmembrane regions of the receptor. The chemokine is shown as a monomer although CCL4 forms a dimer under many conditions. B. Binding contacts made by CC chemokines with vCCI. The structure of CCL4 (PDB ID: 1HUM) is shown in green, with residues buried by contact with vCCI shown in deep pink. Contacts were determined from analysis of molecular dynamics simulation of the structure of vCCI in complex with CCL4 (adapted from the structure PDB ID: 2FFK). (Nguyen et al, and subsequent analysis of their data).

The name of each chemokine is based on its subfamily type, followed by L (to signify it is a ligand of a chemokine receptor), followed by a number to distinguish different specific molecules, e.g. CCL4. For a table correlating older chemokine names with this numerical naming system, see Supplemental Table 1. The different subfamilies exert their influence on different receptors affecting different leukocyte populations[57]. There are about 20 mammalian chemokine receptors, which are 7 transmembrane G-protein coupled receptors (except for so-called atypical receptors) that tend to bind chemokines from one subfamily. There is a great deal of redundancy in the system because many chemokines can bind to multiple receptors, and many receptors can have multiple chemokines as ligands. While this redundancy makes the system more resilient since a mutation in the gene for one receptor may not lead to a diminished immune response, it also means that medically targeting the chemokine system to reduce inflammation is a complex endeavor that may encompass the need to modulate multiple chemokines, multiple receptors and/or multiple cell types.[57]

Chemokine binding to cognate receptors has been the subject of much inquiry and occurs with two sites on the chemokine interacting with two sites on the cognate receptor, leading to receptor activation. The CC chemokine N-loop (from about residues 12-20) and basic residues in the 40s loop bind to the N-terminus of the cognate receptor; subsequently the chemokine N-terminal tail contacts the receptor transmembrane region[56] (Figure 2.1A). Mutation studies on chemokines have found that deletion of the N-terminal tail still allows the chemokine to bind, but not activate, the receptor [58,59], while mutations to the N-loop and basic 40's loop residues reduce binding affinity [58–61]. Upon receptor activation, the receptor-bearing cells proceed to move up the chemokine concentration gradient, toward the site of injury or infection. While chemokines tend to form oligomeric structures in solution and when bound to GAGs[62–65], most (in particular CC chemokines) bind and activate the receptor in their monomeric form [58,59,66].

Before turning to the topic of the modulation of chemokine signaling by pathogens and parasites, we should also note that dysregulation of this pathway to yield an inappropriate or an overly aggressive immune response which can cause or exacerbate a variety of ailments including arthritis, atherosclerosis, and traumatic brain injury [67–69]. Hence, an increased understanding of this complex chemokine communication system may offer strategies to therapeutically dampen the immune response in some situations.

Given the importance of the chemokine signaling system in maintaining surveillance, inflammation, and protection from various types of invasion, other organisms and especially viruses have evolved numerous ways to subvert the chemokine system. For example, some viruses express chemokine analogs that bind chemokine receptors, often (but not always) to antagonize the receptors and stop the response. An example of such a protein is vMIP-II, a viral protein of 72 amino acids that is produced by herpesvirus HHV-8 with a structure very similar to CC chemokines[70]. This protein binds to several chemokine receptors, being an antagonist for CCR1, CCR5, and CXCR4, among others, while apparently agonizing CCR3 and CCR8[71,72]. These chemokine analogs have been reviewed by Alcami and Lira[73]. Another strategy used by viruses is to produce chemokine receptor analogs, which are transmembrane proteins that can bind chemokines and sometimes share the ability to signal. Examples of these include ORF74, produced by Kaposi's sarcoma herpesvirus, and US28, encoded by human cytomegalovirus[73].

Another strategy used by pathogens to control the chemokine response is to secrete soluble chemokine binding proteins (CBP), most acting to bind chemokines before they reach their receptors. The use of CBP allows the pathogen to target specific pathways to subvert the host immune response[57,73–76]. Such CBP are expressed by a wide range of poxviruses and herpesviruses[75,77], and include proteins such as vCCI and M3, respectively. More recently, it has also been discovered that a class of CBP (termed evasins) are used by arthropods such as ticks, that as a group may produce as many as 257 CBP to modulate their host's immune response[78], but note that the arthropod CBP differ in both their structure and mode of function from the viral proteins.

CBP have differing levels of specificity, with some broadly binding multiple sub-families of chemokines, while others bind just one subfamily, or bind only a few chemokines. CBP bind to a variety of different sites on their targets' chemokines. Some CBP bind the GAG-binding region of the chemokine and others bind and block the chemokine's receptor-binding residues or appear to inhibit both functions. Figure 2.1B shows the chemokine CCL4 colored to show the binding interaction sites with the CBP vCCI, in comparison to Figure 2.1A which shows typical residues used by the chemokine to bind GAGs and its cognate receptor. As described below, a common binding feature of these CBP are loops with up to 50% acidic residues that bind basic residues that occur in clusters on the chemokine surface. Other areas of electrostatic complementarity further stabilize the CBP-chemokine complex.

2.4 Survey of Chemokine binding proteins

In this section, we provide a tabular survey of the range of viral and arthropod CBP, listing their chemokine targets, the structural features of their binding, as well as selected data from mutagenesis and/or functional studies on these proteins. This information is listed in Table 2.1 and the corresponding structures are shown in Figure 2.2. Other reviews, with different emphases and scope, are available in the literature[57,74,75,77,79].

Despite the differences in the CBP noted in the table, there are important structural similarities between groups of these proteins. Several of the poxvirus immune-evading CBP share a conserved b sandwich fold (shown in yellow in Figure 2.2 and referred to by Nelson et al. as a "poxvirus immune evasion", or "PIE" domain[76] that is not seen in prokaryotic or eukaryotic proteins (the arthropod CBP Evasin-3 shown in Figure 2G does not contain a b sandwich since it has only one b sheet). One face of this b sandwich acts as the binding surface for the chemokines (see Figures 2.2 and 2.3). Another feature seen in several of these proteins is the "acidic loop" facing the binding site which acts as an "arm" to provide additional binding contacts to the chemokine (see Figure 2.3) and ranges in size from 25 residues in rabbitpox vCCI to only 4 residues in M3 (Figure 2.2E). Finally, an interesting structural feature that seems to be induced by chemokine binding to CBP is the β strand that is formed in the chemokine itself from chemokine residues 8-14 and that is observed in experimental structures of CBP-chemokine complexes, but not seen in the unbound proteins (see further discussion in section 2.5.1. below).
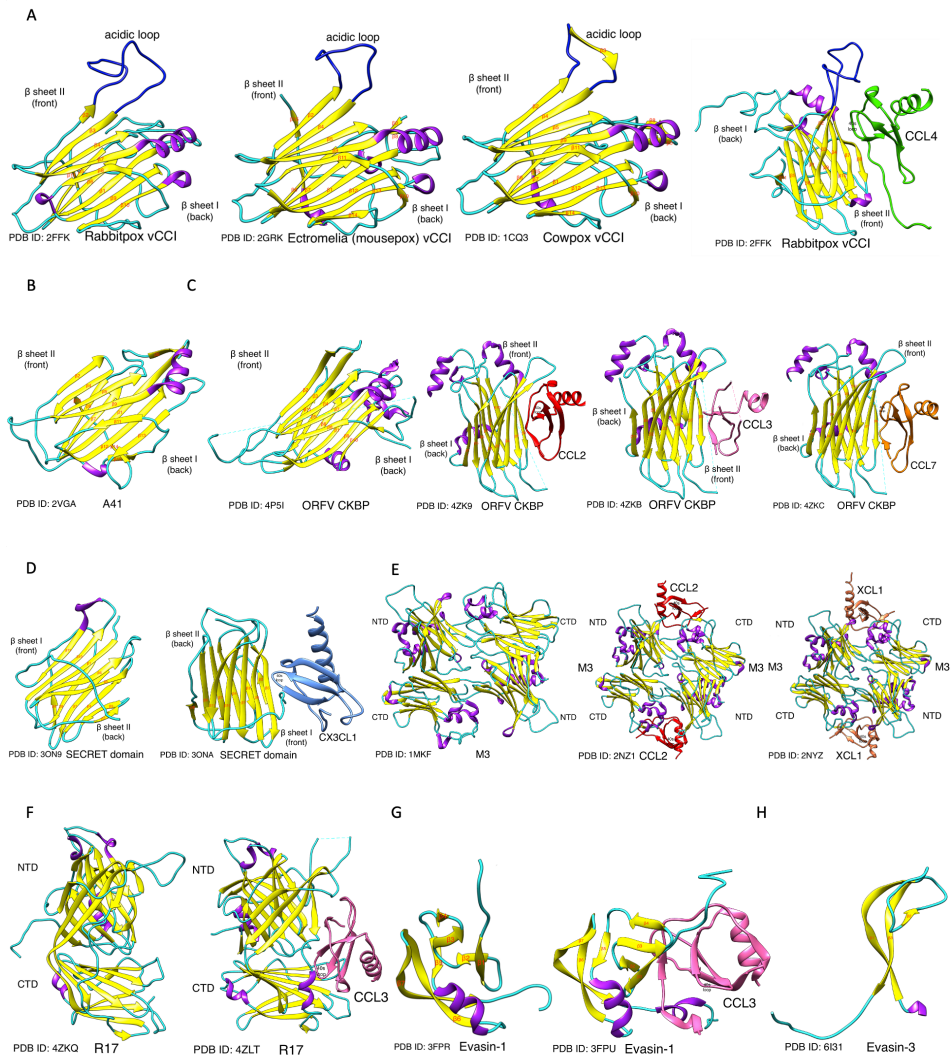
Figure 2.2 The structures of vCCI and other chemokine binding proteins, and their complex with chemokines

Chemokine binding proteins are shown in yellow ribbons with purple helices and blue loops. A: Poxvirus CC chemokine inhibitors. (Left) Three unliganded vCCI: rabbitpox vCCI (PDB ID: 2FFK, ectromelia (mousepox) vCCI (PDB ID: 2GRK), cowpox vCCI (PDB ID: 1CQ3), all shown in the same orientation with acidic loop on the top and b sheet II binding site in the front. Because no unliganded structure of rabbitpox vCCI is available, the "unliganded" rabbitpox vCCI shown here is derived from the vCCI:CCL4 complex and is shown without its ligand for comparison. (Right) rabbitpox vCCI in complex with a CCL4 variant (PDB ID: 2FFK), showing how the rabbitpox vCCI acidic loop and its b sheet II interact with CCL4. B: The structure of vaccinia A41(PDB ID: 2VGA, which is very similar to the structure of vCCI, but does not bind chemokines as tightly as the vCCI family. C: Orf virus ORFV CKBP has a similar b sandwich structure and acidic loop as vCCI, and binds CC chemokines in a similar manner as vCCI. ORFV CKBP has been found to be a dimer and forms a 2:2 binding stoichiometry with chemokines, but we show the monomer to illustrate the similarity to vCCI. From left to right is shown unliganded ORFV CKBP (PDB ID: 4P5I); ORFV CKBP bound to CCL2 (PDB ID: 4ZK9); ORFV CKBP bound to CCL3(PDB ID: 4ZKB; ORFV CKBP bound to CCL7(PDB ID: 4ZKC). D: The ectromelia virus-encoded SECRET domain of CrmD (Left) (PDB ID: 3ON9) and its complex with chemokine CX3CL1 (Right, blue) (PDB ID: 3ONA). While the SECRET domain has a similar b sandwich structure as vCCI, it uses b sheet I rather than b sheet II to interact with the chemokine. E: (Left) Murine gammaherpesvirus68-encoded M3 forms a two-domain b sandwich (PDB ID: 1MKF). (Right) the complex of M3 with CCL2 (red) (PDB ID: 2NZ1) and XCL1 (salmon color, PDB ID: 2NYZ. The stoichiometry of both of these complexes are 2:2. F: (Left) The structure of R17 (PDB ID: 4ZKQ), encoded by rodent herpesvirus Peru (RHVP), has a similar 2-domain b sandwich structure as M3, but (Right) the binding location of the chemokine CCL3 (pink) is different (PDB ID: 4ZLT). G: Evasin-1, a chemokine binding protein from tick salivary gland. (Left) unbound (PDB ID: 3FPR). (Right) Evasin-1 in complex with CCL3 (pink, PDB ID: 3FPU). H: Evasin-3 (PDB ID: 6I31), a chemokine binding protein from tick salivary glands. This protein has a knottin scaffold structure which is necessary for different CXC-chemokine-binding activities.

13

Table 2.1 The summary of chemokine binding proteins

Name, Origin, and Chemokine Target	Medical/Biochemical relevance	Structural features and mutation effects *Figure location (PDB IDs)*
vCCI (aka 35K) Organism: Various poxviruses, including rabbitpox virus, cowpox virus, vaccinia virus, variola virus • CC **vCCI (aka EVM1)** Organism: Ectromelia virus (Mousepox virus) • CC	• Ameliorates numerous inflammatory conditions, including arthritis[80] and atherosclerosis in mice,[81–83] and allergic inflammatory reactions in guinea pigs[84]. • Effective when used intranasally to decrease airway inflammation in a murine model of asthma[85].	*Figure 2A (2FFK[86], 2GRK[87], 1CQ3[88]); (vCCI-CCL4 PDB ID: 2FFK)[86]* • Composed mostly of a β-sandwich fold and has a flexible, highly acidic loop between b strands 2 and 3; or b strands 2 and 4. Forms a 1:1 complex with chemokines. • Length of the acidic loop varies amongst the poxviruses; vCCI uses this loop to interact with key conserved basic residues in the CC chemokines 20s region and 40s loop. • Vaccinia virus vCCI shows a loss of function for mutations E143K or Y80A, and enhanced activity with the mutation R89A[89]. • Mousepox vCCI loses chemokine affinity with the Y69R and the I173R mutations (equivalent to Y80 and I184, respectively in rabbitpox vCCI)[87].
A41 Organism: Vaccinia virus • CC	• Does not inhibit chemokine-induced leukocyte chemotaxis[90]. • Interferes with GAG binding by chemokines[90].	*Figure 2B (2VGA)[90]* • Has 19% sequence identity and similar structure to cowpox vCCI[90] • Uses a negatively charged patch in β sheet II to interact with the chemokine's positively charged loops. • Lacks the acidic loop between the N-terminal b strands, found in vCCI. • Binds chemokines less tightly than the vCCI family.
ORFV CKBP Organism: Parapoxviruses • CC • CXC • C	• BPSV CBP (related to OrfV CKBP) reduces skin inflammation in mice[91] and reduces brain inflammation following a stroke in mice[92].	*Figure 2C (4P5I, 4ZK9, 4ZKB, 4ZKC)[93]* • Exists as a dimer and forms a 2:2 binding stoichiometry with chemokines, unlike the structurally similar A41 and vCCI. • Has a β-sandwich fold along with a small acidic loop between b strands 2 and 3[93]. • Binds CC chemokines in a similar manner to that used by vCCI. • Contains key binding residues E58, E62, E67, binding to R18 and R24 (CCL2 numbering) on the chemokine. • Has a hydrophobic region that forms an antiparallel b strand with the chemokine N-loop (residues 10-17, CCL2 numbering), which contains the residues F13/Y13 used by the chemokine for receptor engagement[93].
SECRET Domain Organism: CrmB (variola virus) and CrmD (ectromelia virus). • CC • CXC • C • CX3C	• Inhibits arthritis when combined with a TNF binding protein[94]. • Transgenic expression CrmD attenuates gut inflammation in a mouse model of Crohn's disease, likely due both to the TNF-binding ability and the chemokine binding ability of CrmD[95].	*Figure 2D (CrmD SECRET domain from Ectromelia virus, PDB ID: 3ON9)[96]; (CrmD SECRET domain-CX3CL1 PDB ID: 3ONA)[96]* • SECRET domain of CrmD adopts a b sandwich and uses b-sheet I in its interaction with the chemokine, unlike vCCI which uses b-sheet II. • Structure of SECRET domain of CrmD in complex with CX3CL1 shows a relatively small surface area of interaction, with heavy reliance on the basic 40's loop of the chemokine in the binding interaction[96]. • Mutation of the positively charged basic residues in the chemokine (K18 and basic residues in the 40's loop, CX3CL1 numbering) confirms their importance in binding the SECRET domain of CrmD. Corresponding mutations in the SECRET domain (D167A/E169A/D316A) abrogate chemokine binding[96].

		· VaV CrmB and EV CrmD found to bind CCL28, CCL25, CXCL12β, CXCL13, and CXCL14 with high affinities, in a study of 43 human chemokines using SPR.[97]
M3 Organism: Mouse herpesvirus-68 • CC • CXC • C • CX3C	• In mice inhibits experimental autoimmune encephalitis (EAE), a disease model for multiple sclerosis in humans[98]. • Prevents streptozotocin-induced diabetes in mice[99].	***Figure 2E (PDB ID: 1MKF)**[100]; **(M3-CCL2 PDB ID: 2NZ1, M3-XCL1 PDB ID: 2NYZ)**[101]* • Inhibits both the receptor binding and GAG binding functionality of chemokines. • Exists as a dimer and the core of the N-terminal domain (NTD) possesses similar structure to vCCI, although with low sequence identity[100]. • Binds chemokines with 2:2 stoichiometry. • Makes contact with the N-terminal/N-loop receptor-binding portion of the chemokine, starting at around residue 8 of the chemokine and including the critical receptor binding residue CCL2 Y13 and XCL1 V12[101]. • Contacts basic regions of the chemokine, including R24 (CCL2 numbering), parts of the 30's loop, and the 40's loop region, the same regions used by chemokines to bind glycosaminoglycans[101].
R17 Organism: Rodent herpesvirus Peru (RHVP) • CC • C	No medical application noted in the literature	***Figure 2F(PDB ID: 4ZKQ); (R17-CCL3 PDB ID: 4ZLT)**[102]* • Forms a two-domain structure (N-terminal and C-terminal b sandwich domains) connected by a bridging sheet; similar in structure to M3 despite only 8% sequence identity. • Has 1:1 stoichiometry compared to 2:2 for M3, with different chemokine binding location, despite their structural similarity. • Binds chemokines in a hydrophobic cavity formed by a flexible linker connecting the two domains. • Mutations that remove negatively charged residues from the linker region 266-270 greatly diminish its ability to bind CC chemokines. • Residues of the chemokine involved in binding R17 are very similar to those used to bind vCCI, including F13, S35, and the residues of the chemokine 40's loop such as R45 and N46. • Mutations to the 40's loop of CC chemokines to add positive residues showed increased binding to R17[102].
Evasin-1,4 **ACA-01** Organism: Arthropod • CC	• Evasins have been shown to reduce inflammation in mouse acute pancreatitis and experimental colitis[103,104].	***Figure 2G (Evasin-1 PDB ID: 3FPR); (Evasin-1-CCL3 PDB ID: 3FPU)**[105]* • Composed of mostly b strands in a "boat" shape. When bound to CCL3, a 1:1 complex is formed. The chemokine sits in the "boat" and contacts both the N- and C- terminal portions of Evasin-1[105]. • Chemokine contacts include T16, S17, and R18, as well as having a interaction between the F13 of CCL3 (a critical receptor binding residue) and F14 in Evasin-1[105]. • Evasin-1 uses residues Phe14 and W89, while Evasin-4, believed to have a similar fold, appears to bind chemokines using different residues, E16 and Y19[106]. • Evasin ACA-01 has been shown to be sulfated at an N-terminal Tyr, indicating likely sulfation of other evasins[107].
Evasin-3 Organism: Arthropod • CXC	• Inhibits neutrophil chemotaxis[108].	***Figure 2H (Evasin-3 PDB ID: 6I31)**[109]* • 66 amino acid protein, structure determined in the absence of chemokines.[108] • Binds to "ELR" containing CXC chemokines, which are a subset having Glu-Leu-Arg near their N-terminus for receptor engagement. • Glycosylated when produced from mammalian cells; active when produced from *E. coli* without glycosylation.
M-T1, M-T7	• Both M-T1 and M-T7 have shown some	***No published structure***

| Organism: Myxoma virus

M-T1:

• CC

M-T7:

• CC
• CXC
• C | efficacy in pre-clinical trials in suppressing inflammatory responses[110,111].
• M-T7 has been shown to reduce hyperplasia after vascular injury from angioplasty in both rabbits and rats[111]. | • With 40% amino acid identity with vCCI proteins (the main subject of this review), M-T1 binds CC chemokines at nanomolar levels[112].
• M-T1can simultaneously bind both glycosaminoglycans and chemokines, potentially allowing localization to sites of inflammation as well as disruption of chemokine function[113].
• M-T7 binds IFN-g and weakly binds chemokines from three subfamilies[114].
• M-T7 likely binds chemokines via the chemokine GAG binding region, not via their receptor binding region[114], indicating that the action of this binding protein is to disrupt the chemokine gradient rather than to directly disrupt receptor interaction. |

The structural and mutation data shown in this table provide numerous independent clues about the specific residue-residue interactions that mediate chemokine-inhibitor binding. However, this data does not on its own constitute a "deciphering of the language" of inhibitor recognition of chemokines. One path towards that goal, described in the remainder of this review, is to focus on one class of chemokine inhibitor, assay their binding affinities to a range of chemokines, and then correlate this data with contacts observed in atomistic molecular dynamics simulations of each inhibitor-chemokine pair. The accuracy of the simulations is then validated by experimentally testing proposed mutations predicted in the simulation to increase or decrease binding.

2.5 VCCI: a CC chemokine binding protein

In this section we focus on one CBP, vCCI from rabbitpox, to provide a detailed analysis of the structural features of its chemokine binding and to highlight the roles of molecular simulation in elucidating these features. Poxviruses have large genomes and produce a variety of chemokine binding proteins. VCCI, sometimes called p35 or 35K, is a chemokine binding protein made by several poxviruses, including those that infect humans and other mammals. VCCI has been shown to bind dozens of CC chemokines, many with low sequence identity to each other, at nanomolar (or even picomolar) levels[115–117]. This makes it a particularly intriguing example for the study of protein-protein interactions.

2.5.1 Experimental studies of vCCI-Chemokine binding

Structurally, vCCI resembles several other chemokine binding proteins, being composed of 11 b strands forming a b sandwich configuration[86–88]. Its bound structure reveals that one face of the sandwich contains the binding site, and there is a large, negatively charged loop between b strands 2 and 3 that is used to anchor the CC chemokine in place, as described in more detail in this section below[86,87]. VCCI is capable of binding more than 80 different CC chemokines across multiple species; however, Burns et al. found no significant binding of vCCI to chemokines from the other three subfamilies[115]. All CC chemokines share a similar tertiary structure composed of three antiparallel b sheets in a Greek key conformation, ending with a C-terminal α helix, but differ greatly in their amino acid sequence and also differ in their cognate receptors.

To maintain the specificity for CC chemokines along with the ability to bind such a variable group of proteins, vCCI utilizes both specific amino acids on its binding face, and its highly acidic loop to complement the positively charged residues conserved on chemokines.

VCCI binds CC chemokines in a 1:1 ratio, as shown in Figure 2A where the structure of vCCI in complex with CCL4 is shown[86]. Key contacts between vCCI and CC chemokines are mediated by negatively charged residues on vCCI, including a long loop composed largely of acidic amino acids. This loop can vary in length, with the rabbitpox vCCI loop being 25 amino acids, while the mousepox (ectromelia) EVM1 loop is only 15 amino acids. These residues and others, including E143 and D141 bind to basic residues on the chemokine. VCCI also forms a hydrophobic interaction with F13 on the chemokine, a position typically containing a large hydrophobic residue in most CC chemokines, that is critical for binding its cognate receptor. Residues 8-14 of the CC chemokine interact with residues 180-186 of vCCI, forming an additional antiparallel b strand upon binding. Interestingly, this formation of a new b strand in the "N-loop" of the chemokine upon complex formation has also been observed in several other chemokine binding proteins, including in M3 binding to CCL2[100], Evasin-1 binding to CCL3[105], and ORFV CKBP binding to CCL2[93]. While not labeled as a b strand in the structure for vCCI with CCL4 in Figure 2.2A, the additional b strand has been observed in MD simulations with vCCI bound to several chemokines [118].

Early studies of vCCI-chemokine interactions involved mutating residues on the chemokine and testing these for changes in binding affinity to determine the involvement of the residue in the interaction. Two such studies tested mutations on CCL2 by surface plasmon resonance and ELISA assays, and both found that Y13A, R18A, and R24A (as well as R24E) significantly reduced affinity to vCCI[119,120]. These residues have been previously shown to also be utilized for chemokine receptor binding[61], indicating that vCCI blocks chemokine signaling by obscuring residues involved in receptor binding.

Our group found similar interactions in these conserved residues in a variant of CCL4. This work determined the structure of vCCI bound to CCL4 using NMR[86] and indicated that R18 interacts with D141 and E143 of vCCI, both found on the binding face of the b sandwich (Supplementary Figure 2.1C). In the vCCI:CCL4 structure, the residue F24 (analogous to R24 in CCL2), along with K45 and R46 (both mutated to alanine in the structural study to reduce aggregation) were found near the acidic loop of vCCI. (Supplementary Figure 1B shows the simulated structure of wild type CCL4 bound to vCCI including its interactions with the acidic loop, with residues 24, 45, and 46 highlighted.) In aligned sequences for multiple CC chemokines, at least one positive charge is found in the corresponding 24/45/46 residues. The distribution of acidic residues in the vCCI loop allows it to find complementary charges on the 20's and 40's loop of chemokines. In later work, we confirmed the importance of charged basic residues on the chemokine by mutating these residues in CCL11(R22A and K44A). Mutating only one of these residues results in a 1.5- to 2-fold decrease in affinity as measured by fluorescence, mutating both results in a 4.8-fold decrease, and mutating both along with R16A (equivalent to R18 in CCL4) leads to a 134-fold decrease [116].

Structural studies also showed that F13 of CCL4 (Y13 in CCL2) fits in a hydrophobic pocket between b sheets I and II of vCCI. As noted in a sequence analysis by Ziarek et al, of 24 human CC chemokines, 9 had a Phe in this position, with other

residues generally being large hydrophobics like Leu and Tyr[121]; this residue generally has a role in both in receptor binding and in mediating chemokine dimerization[59,60]. Mutation to alanine in this position results in an approximately10-fold decrease in affinity for vCCI[119,120], likely due to reduced interactions with the hydrophobic pocket of vCCI, formed by conserved residues V185 and Y217 (Supplementary Figure 2.1D).

Work on CCL2 also found that K49, when mutated to alanine, showed an increase in binding affinity to vCCI[119,120]. This is often a conserved basic residue in CC chemokines (K48 in CCL4, K47 in CCL11). When bound to vCCI, this residue packs closely with Y80 and R89, likely causing steric crowding and/or poor electrostatic interactions due to the positive charges of the two basic residues (see Supplementary Figure 2.2). Fremont, et al. replaced Y69 of EVM1 (Y80 in vCCI) with a large, positive residue, correctly hypothesizing that it would drastically reduce chemokine binding[87]. Correspondingly, it was proposed that mutation of either Y80 or R89 to the small amino acid alanine in vCCI would likely reduce this clash and improve overall binding. White et al[89] tested this hypothesis by separately mutating Y80 and R89 in vCCI to see if replacing these residues with alanine would result in better chemokine binding by vCCI and therefore lower chemokine function. Per their expectations, R89A was found to increase chemokine binding (and thereby block the activity of CCL5, which was the chemokine used in their functional assays). However, rather than enhancing chemokine binding, the Y80A mutation paradoxically resulted in loss of the ability of vCCI to inhibit CCL5 activity, presumably because the Y80A vCCI variant was no longer able to bind the chemokine[89]. The question of why the Y80A vCCI variant unexpectedly has weaker chemokine binding is currently being addressed computationally and in ongoing experiments[122–124].

2.5.2 Computational simulations of vCCI-Chemokine binding

The experimental data described in the previous section provided myriad separate clues about the roles of individual residues involved in vCCI-chemokine binding. Computational molecular modeling can provide a framework to holistically evaluate the contributions of each residue to this binding interaction. Recently we published a combined experimental and computational study of the binding of vCCI to the chemokine CCL4 and the virally produced chemokine analog vMIP-II[125]. NMR analysis showed an overall similar binding by vCCI to the two proteins, and fluorescence studies found that vCCI:vMIP-II had a higher binding affinity than vCCI binding to an actual mammalian chemokine, CCL4. Molecular dynamics simulations (see Appendix for a brief overview of relevant molecular simulation techniques) were performed on these complexes, as well as on a complex with the CCL4 mutant that was used to solve the original structure of the vCCI:CCL4 complex (K45A/R46A/K48A). An analysis was performed of the type and duration of the vCCI-chemokine interactions. These simulations showed that the vCCI:vMIP-II structure had more interprotein hydrogen bonds and interface surface area than vCCI:CCL4, which in turn had more extensive contacts than the vCCI:CCL4 mutant. These results qualitatively corroborated the measured binding affinities, but importantly also produced residue-level "maps" of the interprotein interactions which mediate the binding. To give some examples of structural results noted in this study: the chemokine residue R18 is shown to be important in the binding of both vMIP-II and CCL4; vCCI S182 was seen to have a persistent hydrogen bond to C51; and the vCCI I184 (rabbitpox numbering) which earlier studies in mousepox[87] had suggested caused unfavorable interactions, was instead seen in the MD simulations to interact with I41 and C51 in vMIP-II[125].

18

In addition to providing atomic-level details of the binding in experimentally realized complexes, simulations can also be applied to "hypothetical" complexes, to predict the structure and qualitatively estimate the binding strength. For example, the chemokine CCL17 is one of the few CC chemokines that does not bind well to vCCI[115], likely because CCL17 lacks several of the positively charged residues that have been shown to be important in a vCCI:chemokine complex, including lacking basic residues at positions 18, 45, and 46 (CCL4 numbering). Molecular dynamics simulations of the vCCI:CCL17 complex yield results that can be compared to simulations of vCCI bound to CCL4 and vMIP-II[118]. Figure 2.3 shows the contacts and final bound structures from molecular dynamics simulations of vCCI bound to CCL4 and CCL17.
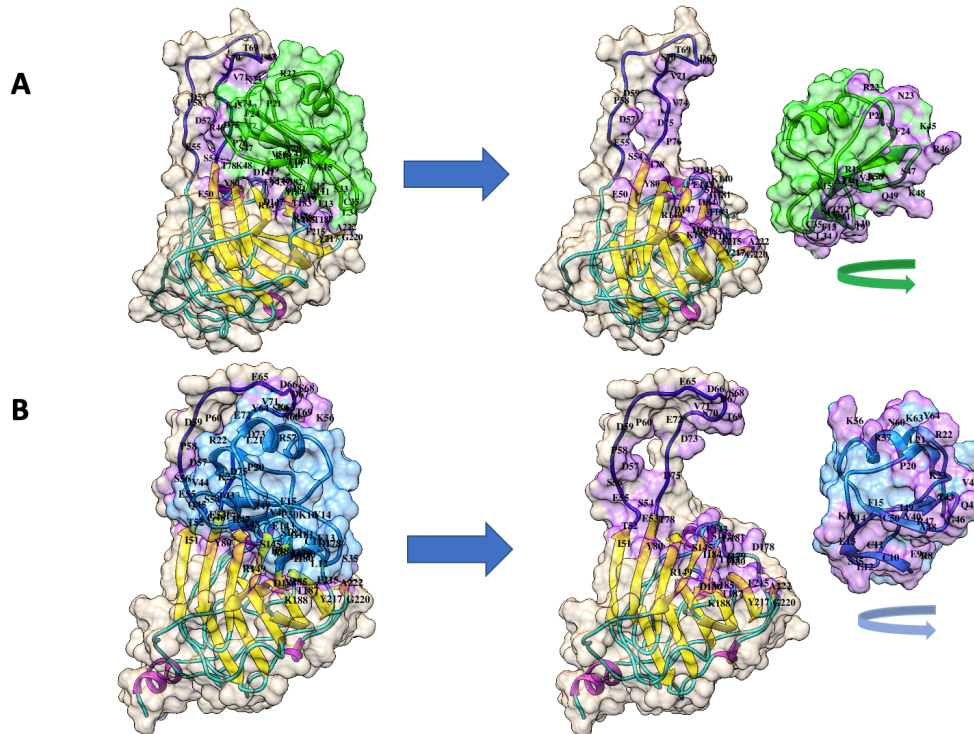
Figure 2.3 Interface of vCCI and its chemokine ligands as predicted by molecular dynamics simulations

The surface area is shown for (A) vCCI when bound to CCL4 and (B) vCCI when bound to CCL17. The structure used in A comes from the PDB ID 2FFK, in which the CCL4 ligand was mutated back to wildtype and molecular dynamics was run for 1µs. In B, the vCCI:CCL17 structure was built by modeling the complex, starting with 2FFK and replacing the chemokine by aligning the Cα backbone. To visualize the intermolecular interactions, each component has been moved apart and rotated to reveal the binding face. vCCI (beige) is on the left, the chemokine ligand is on the right (green for the CCL4, blue for CCL17). The contact surface area between vCCI and each chemokine is colored in purple. The residues involved in the interface on both vCCI and the chemokine are labeled. Contact surface area identified on the CCL17 α helix suggests non-canonical binding with the vCCI acidic loop compared to other chemokines.

The images show the solvent-accessible surface of each protein superimposed on its secondary structure given in the usual "cartoon" format. The contact regions for both proteins are shaded in purple. This illustrates the similarities and differences in the binding of these two chemokines. Both chemokines have multiple contacts to the face of β sheet II of vCCI and all along the acidic loop which wraps over both chemokines. Comparing the two simulated structures, both chemokines obscure nearly the same residues of the vCCI b sheet II face. The differences appear in how the acidic loop of vCCI binds the chemokine. In complex with CCL4, the lower region of the vCCI acidic loop (residues 54-59) contacts the 40s loop of the chemokine, while the middle residues of the vCCI loop (residues 67-71) interact with the chemokine's 20s region. In the simulation with CCL17, the lower region of the vCCI loop (residues 55-60) contacts the 20s region and the 40s loop of CCL17, while the middle residues of the vCCI loop interact with the α helix of the chemokine instead.
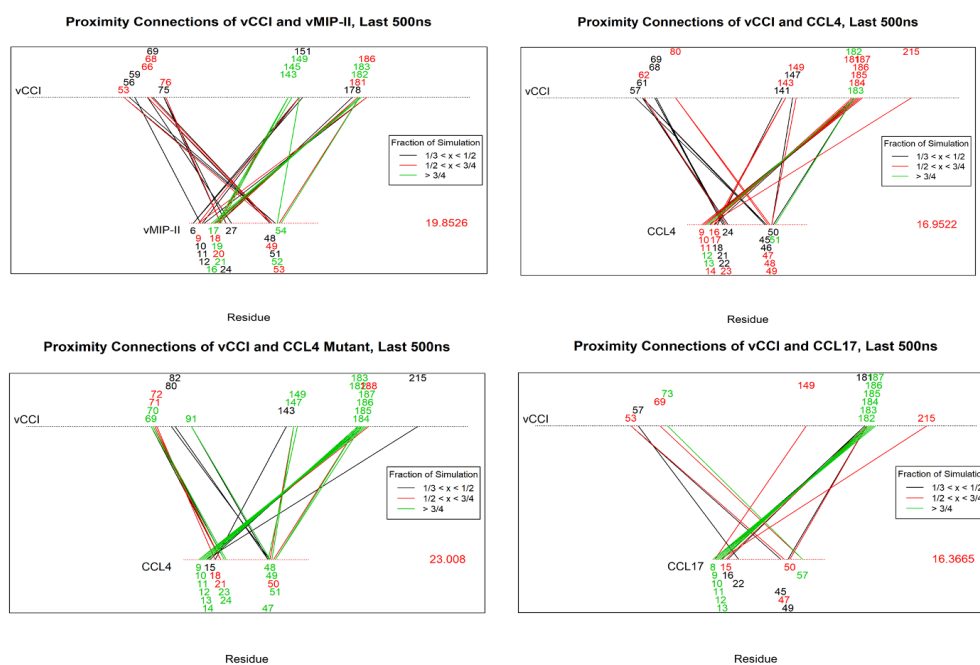
Figure 2.4 Contact maps for vCCI:chemokine interactions

Contact maps show the residues in close proximity between vCCI and the designated chemokine. Analysis was performed on the last 500ns of the 1μs simulations to allow the system to equilibrate. The top horizontal line in each figure represents the sequence of vCCI, from amino acids 1-242. The bottom horizontal line represents the amino acid sequence of each chemokine, ranging from residue 1 to about 70, depending on the chemokine. Each transecting line indicates a contact between vCCI and the chemokine during the last 500 ns of the simulation. The color of the line indicates the fraction of the simulation time the two residues are within 2.8 Å of each other, ranging from black (in contact for a third to a half of the simulation; 167-250ns); red (in contact for a half to three-fourths of the simulation; 250-375ns); and green (in contact for more than three-fourths of the simulation; more than 375ns). The numbers above and below the horizontal lines list the residue numbers of vCCI and the chemokine, respectively, that are involved in an interaction. The color of the number is representative of the most persistent interaction it is a part of, matching the coloring used for the transecting lines. The number in the lower right of each graph is the sum of the fraction of time during the simulation that the indicated interactions are observed, where a higher number indicates more persistent and/or a larger total number of interactions throughout the simulation.

The persistent vCCI-chemokine contacts for vCCI bound to CCL17, as well as for vCCI bound to CCL4, mutant CCL4, and vMIP-II[125] are shown in Figure 2.4. In each diagram, the line at the top represents the sequence of residues in vCCI and the line at the bottom represents the residues in the chemokine. The colored lines between the vCCI and the chemokines show persistent contacts during the molecular dynamic's simulation, and these are color-coded by the fraction of the simulation time they are present, with the green line indicating the most persistent contacts. All four chemokines show extensive, persistent contacts between the N-terminal region of the chemokine (residues 8-14) and β strand 8 on vCCI (residues 180-187). But clear differences arise in the number and persistence of contacts from CCL17 to the vCCI acidic loop (residues 57-75) and other residues on β strand 7 (residues 143-149), compared to the other three chemokines. The fewer, but more persistent, contacts of the vCCI loop to CCL17 suggest the loop becomes locked in a particular conformation with the α helix due to the limited number of charged residues available for it to bind. In contrast, the acidic loop can move between the key charged residues along the 20s region and the 40s loop in other chemokines, resulting in more interactions[118].

Figure 2.5 shows the buried surface area for vCCI and several chemokines as determined by MD simulations. This type of representation illustrates the shared binding face on vCCI. One region of note, residues 180-186 of vCCI, shows identical occlusion (calculated based on the accessibility of the residues to a water-sized molecular probe) from each chemokine. Computer visualizations and secondary structure analysis of MD simulations of this region show each of the chemokines forming an additional β strand
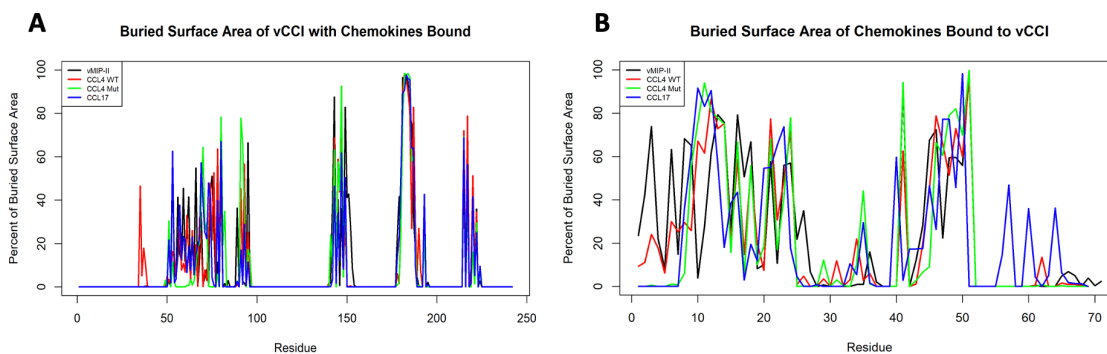
Figure 2.5 Buried surface area of vCCI and chemokines when forming a vCCI:chemokine complex

The percent of buried surface area of each residue is shown for (A) vCCI and (B) selected CC chemokines. The x-axis represents the amino acid sequence of each protein; the y axis represents the percent of that amino acid that is buried during the last 500ns of the 1μs simulation of the complex. The percent of buried surface area is based on the ratio between the buried surface area (when bound) and the accessible surface area (when in solution). Each colored line represents a complex between vCCI and a separate chemokine, with vMIP-II, CCL4 WT, CCL4 Mut, and CCL17 shown in black, red, green, and blue respectively. (A) shows that buried surface area for vCCI is largely the same regardless of the chemokine bound, while (B) shows greater variability in amino acids making contact with vCCI, depending on the chemokine. "CCL4 Mut" is the K45A/R46A/K48A variant of CCL4. Similarities across complexes, such as the 180-186 peak in (A), indicate conserved regions involved in chemokine binding. Alternatively, differences in buried surface area, such as the peaks from 55-65 for CCL17 in (B), can reveal unique binding patterns not utilized by the other complexes.

aligned with chemokine residues 8-14 (see Figure 2.3 and Supplementary Figure 2.3). As noted previously in sections 2.3 and 4.1, this feature, observed in simulation, appears to be common in the experimentally determined structures of binding of chemokines by several CBP, including M3, Evasin-1, and ORFV[93,100,105]. As in the results given in Figures 2.3 and 2.4, Figure 2.5 shows that CCL17 has distinct differences in its binding structure compared to the other chemokines simulated. This chemokine causes a similar pattern of buried surface area on the residues of vCCI as do the other chemokines. However, the buried surface area on the CCL17 itself is notably different from that on other chemokines when bound to vCCI. Unlike the other three chemokines shown, CCL17 has several residues in the C-terminal α-helix in contact with vCCI. This distinctive binding pattern has not yet been experimentally verified, but it is reasonable to infer that the need for the vCCI acidic loop to be highly extended to bind to the CCL17 helix may lead to reduced binding for CCL17 compared to other CC chemokines.

2.6 Prospects for engineering CBP specificity and affinity

As described in section 2.4, many studies have investigated amino acids on the chemokine that affect its binding to a CBP, particularly with vCCI[116,119,120]. Perhaps more relevant for the practical use of CBP in medical applications are investigations to add chemokine binding functionality to this medically relevant protein itself[94] or to study changes in CBP that affect their ability to bind particular chemokines. Structural studies have guided mutations in vCCI-like proteins to determine important features for chemokine binding[87] as well as to allow the successful construction of a variant (R89A) that increases the potency of vCCI[89]. Another study used computer modeling to obtain a structural model of Evasin-4 in complex with a chemokine, followed by phage display to confirm binding determinants suggested by the model[106]. This was a successful marriage of computation and experiment, although the authors expressed disappointment that this work did not lead to the successful design of a potent chemokine inhibitor[74].

We contend that the synergy of structural biology, biochemical experiments, and computer modeling will lead to a more nuanced understanding of CBP-chemokine interactions, which can, in turn, allow molecular engineering of CBP and chemokines with novel binding strength and specificity. These can be tested experimentally, and iteratively optimized until a particular goal is achieved. In ongoing work, we are investigating the complex between vCCI and CCL17. As noted in the previous section, vCCI does not bind CCL17 well[115], likely because CCL17 lacks several of the important basic residues that have been shown to confer affinity to vCCI. A highly specific CCL17-binding protein would be valuable in the study of certain diseases because this chemokine recruits Th2 cells during the inflammatory response in several medical conditions, including allergic asthma[126,127]. Therefore, we plan to use a combination of simulation and experimental work to make a variant vCCI that has high affinity to CCL17. The goal is to modify only vCCI, not CCL17, so that the modified CBP can bind wild type CCL17 as proof of concept that this design technique could be used in a real-world application.

Overall, the long co-evolution of viruses and parasites with their hosts has led to a unique family of proteins, CBP, that subvert the mammalian immune system by binding to chemokines, thereby impeding the function of some host immune cells. Due to this binding ability, CBP have been shown to have remarkable anti-inflammatory properties in vitro and in vivo, with work ongoing in several labs to translate their function into useful therapeutics [74,79,94]. These CBP often share structural features and bind conserved regions

of the chemokines, particularly basic residues and those residues involved in receptor binding and GAG binding. A greater understanding of how CBP bind their chemokine ligands can be pursued by a combination of computational and experimental work, with outcomes that may include altered or tailored specificity in chemokine binding.

2.7 Appendix: Computer simulations of protein-protein binding

As has been described here, viruses and other parasites make a variety of chemokine binding proteins that can be studied to provide a wealth of knowledge about the details of protein-protein interactions. These interactions can inform future studies of other proteins and can be used to make mutations to fine-tune the activity of a particular chemokine binding protein. Given the wealth of structural and biochemical data now available for several of these proteins, computational analysis can be a major tool in their study, leading to testable hypotheses about modes of interactions carried out by CBP and even proposing new mutations to tune binding specificity.

Computer analyses play myriad roles in structural biology and biochemistry, from bioprospecting sequence data for novel genes[128] (including a study to identify evasin-like proteins in tick genomes[78]) to identifying protein-protein binding inhibitors[129]. A potentially profound role for computers is the atomic-scale simulation of biomolecular structure and function, which in principle could elucidate the biochemical mechanisms at exquisite spatial and temporal scales[130]. The most accurate molecular simulations solve the equations of quantum mechanics to predict molecular structures, interaction energies, and even reaction rates, but such methods are presently too computationally costly to be routinely applied to biochemical questions. Instead, so-called classical molecular dynamics (MD) methods are typically used, where each atom is treated as a classical particle typically carrying a partial charge and bound to other atoms by springs (a detailed introduction to MD algorithms has been published by Frenkel and Smit[131]). The so-called "force fields" used in MD simulations include electrostatic and Van der Waals interactions that represent the whole range of molecular interactions, including hydrogen bonds, salt bridges, and hydrophobic contacts. These simulations produce "trajectories" in the form of 3D movies of the motions of every atom in the system during the simulation time. There are inherent limitations to classical MD, especially its inability to directly model chemical reactions, including acid-base chemistry, but despite these limitations, classical MD is emerging as a key tool for studying biochemical processes including protein folding and protein-ligand binding[132,133]. Improvements in computer speeds and MD algorithms have increased the size and timescale of feasible calculations to the point where multi-microsecond simulations of complete proteins and their immediate surroundings are routine and the longest protein MD simulations run into the millisecond domain[134].

For the specific question of studying and engineering protein-protein interactions, MD has two primary uses. First, MD simulations can generate trajectories containing realistic conformations of the molecular system that can be analyzed to show the location and persistence of electrostatic, hydrophobic, and hydrogen bond interactions between the two proteins, as well as changes in the secondary and tertiary structure of the proteins, as was described in section 2.4.2 above. For most protein systems, such simulations are sufficiently easy to set up and are fast enough on inexpensive workstations that it is possible to routinely run many simulations of different protein-protein binding pairs. This allows the computational "mapping" of differences in the interactions between different binding partners and different protein isoforms. A recent review article describes many

examples of the complementarity of molecular modeling and experimental structural biology for the binding of chemokines to their natural targets as well as to small-molecule inhibitors[135].

Another at least potential use of simulation is for the prediction of absolute and/or relative binding free energies between proteins[136]. These simulations can in principle yield binding free energies accurate to a few kcal/mole, but there are still many challenges to routine free energy binding calculations[137]. Nevertheless, improvements in computer speeds, simulation algorithms, and force fields, are making calculations of relative ligand-protein binding free energies increasingly accurate and feasible, especially for relatively small, "drug size" ligands[138]. The most established method for calculating binding free energies is "free energy perturbation" (FEP) also known as "alchemical perturbation" which involves the computational transformation of a molecule or molecular fragment into another molecule[139]. Although the FEP process is not possible in the physical world, this transformation has the same free energy change as a thermodynamic cycle that first unbinds the first ligand and then binds the second. The routine calculation of accurate protein-protein binding free energies by FEP is hampered by the size and flexibility of protein ligands, but recent, carefully validated studies demonstrate that accurate results are achievable[140]. In addition to free energy perturbation methods, several promising new techniques for calculating the binding free energies are being developed, including fragment-based methods[141] and machine learning methods[142] that offer the promise that protein-protein binding energy calculations will become routine and accurate.

Chapter 3

Efficient Production of Fluorophore-Labeled CC Chemokines for Biophysical Studies Using Recombinant Enterokinase and Recombinant Sortase

3.1 Abstract

Chemokines are important immune system proteins, many of which mediate inflammation due to their function to activate and cause chemotaxis of leukocytes. An important anti-inflammatory strategy is therefore to bind and inhibit chemokines, which leads to the need for biophysical studies of chemokines as they bind various possible partners. Because a successful anti-chemokine drug should bind at low concentrations, techniques such as fluorescence anisotropy that can provide nanomolar signal detection are required. To allow fluorescence experiments to be carried out on chemokines, a method is described for the production of fluorescently labeled chemokines. First, a fusion-tagged chemokine is produced in E. coli, then efficient cleavage of the N-terminal fusion partner is carried out with lab-produced enterokinase, followed by covalent modification with a fluorophore, mediated by the lab-produced sortase enzyme. This overall process reduces the need for expensive commercial enzymatic reagents. Finally, we utilize the product, vMIP-fluor, in binding studies with the chemokine binding protein vCCI, which has great potential as an anti-inflammatory therapeutic, showing a binding constant for vCCI:vMIP-fluor of 0.37±0.01 nM. We also show how a single modified chemokine homolog (vMIP-fluor) can be used in competition assays with other chemokines and we report a Kd for vCCI:CCL17 of 14µM. This work demonstrates an efficient method of production and fluorescent labeling of chemokines for study across a broad range of concentrations.

3.2 Introduction

Chemokines are small immune system proteins that bind 7-transmembrane receptors and mediate chemotaxis of leukocytes. Given their size (around 70 amino acids), these proteins are amenable to structural characterization by NMR, and the groups of Marius Clore and Angela Gronenborn were instrumental in obtaining early high resolution structures of chemokines, such as CCL4 (MIP-1b) and CXCL8 (Interleukin-8).[143,144] There are four subfamilies of chemokines, based on the placement of conserved cysteines near the N-terminus of the proteins. So-called CC chemokines have contiguous cysteines and form one of the largest subfamilies, with about two dozen members, having roles from T cell maturation to inflammation upon injury and infection.[145,146] Notably, due to their tight binding to the chemokine receptor CCR5, several CC chemokines (CCL3, CCL4, CCL5) have also been identified as inhibiting infection by HIV-1, which uses CCR5 as a co-receptor for infection.[146,147] Subsequently, variants of these chemokines have proven to be highly potent HIV inhibitors.[51,148–150]

Due to their role in inflammation, maturation, and cell homing, chemokines play a role in both health and disease, and have been implicated in several pathologies including arthritis, multiple sclerosis, and traumatic brain injury.[146,151–153] The study of these proteins remains robust, along with investigation of strategies to control their action. Therefore, there remains a need to optimize the production of chemokines, and in particular, to modify chemokines for biophysical study.[148,154–156] While isotopic labeling of chemokines for NMR is already well-documented, many binding studies rely on fluorescence spectroscopy,

especially when working at the low concentrations that are necessary to investigate the binding constants of these proteins.

The poxvirus protein vCCI (also called p35), is a 243 amino acid beta sheet protein that tightly binds CC chemokines, with equilibrium dissociation binding constants often at low nanomolar or even sub nanomolar concentrations.[21,22,55,157,158] Due to its ability to inhibit chemokine function, vCCI is a potent anti-inflammatory agent and a possible therapeutic, especially if it can eventually be targeted to particular chemokines.[12,159–161] While nanomolar concentrations are not suitable for most protein NMR experiments, binding experiments observed via fluorescence spectroscopy can be carried out at these concentrations if the chemokine is labeled with a fluorophore. We have pursued methods to label CC chemokines in order to allow a variety of fluorescence experiments, particularly to study the vCCI:chemokine interaction.
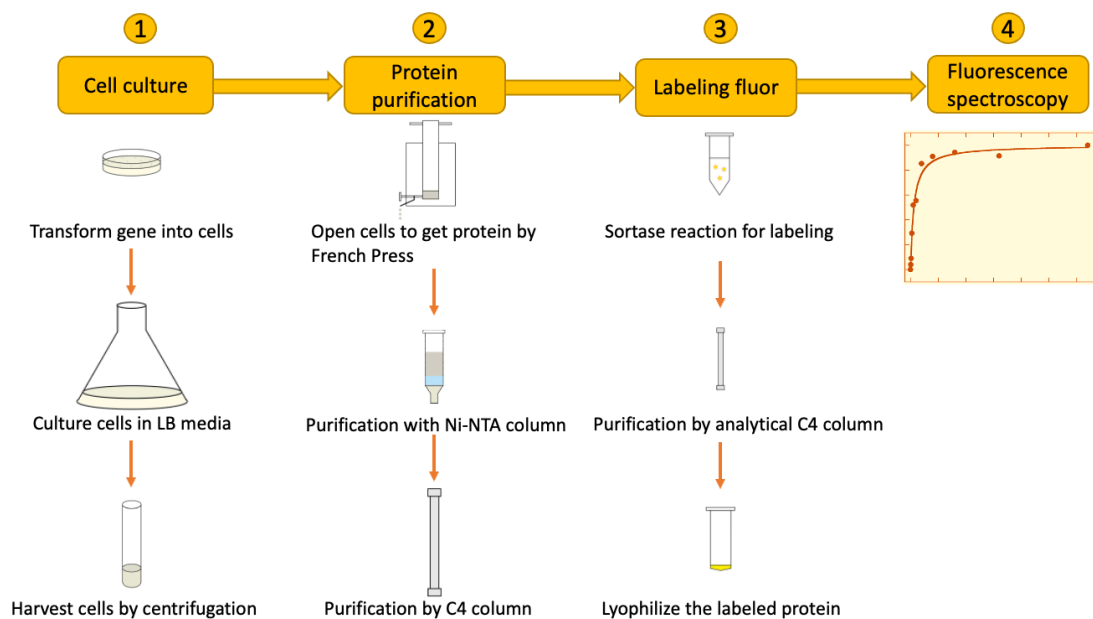
Figure 3.1 Flow diagram showing the steps of purification of fluorescently labeled chemokines

Many chemokines can be expressed in high amounts from E. coli using the T7 expression system, although often an N-terminal fusion tag is required. Generally, for CC chemokines, it is most efficient to unfold the protein in denaturant such as guanidinium chloride and then refold it using any of a variety of conditions.[22,154,162,163] But there are still several impediments to the efficient production of fluorophore-labeled chemokine. One impediment is the cost of specific proteases to cleave the fusion tag, which can be hundreds of dollars per aliquot from commercial sources, but which is necessary because the activity of a CC chemokine is sensitive to the exact sequence at its N-terminus.[163,164] Several well-known proteases such as TEV and thrombin leave extra amino acids at their cut site, making them unsuitable for use in chemokine production. Another roadblock is the often-low yield (and sometimes low specificity) of chemical conjugation of a fluorescent tag, although this can be mitigated if the protein is small enough to allow solid phase synthesis, followed by efficient chemical addition of the fluorophore.[165]

We present here a comprehensive set of methods for producing and purifying fluorescently labeled CC chemokines (Figure 3.1), including reducing costs for cleaving a fusion tag (by inexpensively producing the highly specific protease enterokinase in-lab) and similarly by implementing enzymatic fluorescent labeling of the chemokine with in-house produced sortase. We then show the use of a fluorescently labeled model chemokine (the chemokine homolog vMIP-II) in both direct fluorescence anisotropy titration experiments and as a reagent to test binding by an unlabeled chemokine (CCL17) in competition anisotropy experiments.

3.3 Materials and Methods

3.3.1 Materials

The gene sequence encoding the human Enterokinase (EK) catalytic subunit with an N-terminal tag (MGPINQTNDDDDK, which contains the EK recognition site for self-activation of EK), a single mutation Cys112Ser, and a C-terminal His6-tag, was codon optimized in the pUC57 vector and purchased from GenScript (Piscataway, NJ). The DNA sequence is as follows:

ATGGGCCCTATTAACCAGACCAACGATGACGACGATAAAATTGTGGGTGGCAGCAA
CGCTAAAGAAGGCGCGTGGCCTTGGGTCGTTGGCCTGTACTATGGCGGTCGCCTG
CTGTGTGGCGCGAGCCTGGTTAGCTCCGATTGGCTGGTTAGCGCGGCGCACTGTG
TCTACGGCCGTAACCTGGAACCGAGCAAATGGACCGCCATCCTGGGCCTGCACAT
GAAAAGCAACCTGACGAGCCCGCAAACCGTACCGCGTCTGATCGATGAAATTGTGA
TCAATCCGCACTATAACCGCCGTCGTAAAGATAACGATATTGCGATGATGCATCTG
GAGTTTAAAGTTAACTATACCGATTATATTCAGCCGATTAGCCTGCCAGAGGAGAAT
CAGGTTTTCCCGCCGGGCCGTAATTGTAGCATTGCCGGTTGGGGTACGGTCGTCT
ACCAGGGCACCACTGCCAACATTCTGCAGGAGGCAGATGTGCCGCTGCTGAGCAA
CGAACGTTGCCAACAACAAATGCCGGAATATAATATTACGGAGAACATGATCTGCG
CAGGTTACGAAGAAGGCGGTATCGATTCTTGTCAGGGTGACAGCGGTGGTCCTCT
GATGTGTCAGGAAAATAACCGCTGGTTTCTGGCAGGCGTTACTTCCTTTGGTTACA
AATGCGCACTGCCGAATCGCCCGGGTGTGTACGCACGCGTGTCCCGTTTCACGGA
ATGGATTCAATCCTTTCTGCATCATCATCATCACCATTAA

E. Coli BL21(DE3) cells, XL1-Blue cells, plasmids pET15b, pET28a, and pET32a were purchased from Novagen (Madison, WI). Ni-NTA agarose was purchased from Qiagen (Valencia, CA). Restriction enzymes were purchased from New England Biolabs (Ipswich, MA). The Broad-Range Molecular Weight Markers and 4-20% Mini-PROTEAN® TGXTM Gels were purchased from Bio-Rad (Hercules, CA). The peptide GGGK-FAM (fluorescein amidite) was obtained from Bon Opus Biosciences.

A cure for HIV is impossible until the HIV reservoir is fully understood and either removed or permanently silenced so that the ability to produce new virions is completely abrogated. Various strategies have been proposed to eradicate the latently infected cells: "shock and kill", "locking" cells in latency and dual-affinity retargeting (DART)[166–175]. The earliest and most investigated HIV elimination strategies are the "shock and kill", which usually consist of a drug/compound that activates transcription of the dormant HIV genome (the "shock), yielding the expression of viral proteins that would be recognizable by the immune system, and potentially additional targeted drugs, that could then "kill" the infected cell[166–168,170,171]. The process of "locking" cells into a latent state, usually through gene therapy or tat inhibitors, theoretically prevents any future transcription of the HIV

genome. Locking techniques and development has been thoroughly reviewed[168–170,172,173,176–179] and will not be discussed further here.

Shock and kill methods have shown promise to transiently increase viral expression in cell[180–185] and animal models[186–194] but, there is no visible evidence that the viral reservoir has been reduced, let alone eliminated. More targeted approaches for shock and kill methods are needed since many of the previously tested strategies are very broadly acting with toxic side effects[169,195–198]. Latency reversal agents (LRAs) include Histone Methyltransferase (HMT) inhibitors[199], Toll-like receptor 7 agonists[200–204], histone deacetylase (HDAC) inhibitors[166,173,205–209], and activators of the nuclear factor-κB (NF-κB) pathway [193,194,210]. HDAC and HMT inhibitors loosen the interactions between histones and DNA, unwinding the DNA and allowing transcription and production of viral proteins[211]. NFκB is a protein complex that controls transcription of DNA[212] , so activation generally up-regulates transcription in a cell, increasing the chance of viral expression.

The most natural and potent enhancer of HIV transcription, that should only induce activation of HIV DNA, is the HIV protein Tat. The Tat protein is responsible for ensuring viral transcription during the viral lifecycle. Tat stimulates transcription by binding to the transactivation response element (TAR) in developing RNA transcripts and recruiting Cyclin T1 and cyclin-dependent kinase 9, which compose the positive transcription elongation factor b (P-TEFb) and will promote transcriptional elongation by recruiting and phosphorylating RNA polymerase II, releasing the elongation inhibitor complexes termed NELF and DSIF[213–222]. Tat has also been shown to bind the upstream promoter regions[223]. Research has shown that insufficient Tat transactivation activity can result in latency[224–229]. Tat inhibitors are being investigated as a means to lock latently infected cells[174,230,231]. Tat has also been investigated as a shock agent[227,228,232–235], but issues with cytotoxicity[227,236,237] highlight a need for a method to target Tat and other LRAs to cells most likely to be infected with HIV. Geng et al generated a mutated Tat to minimize its toxicity while maintaining activity as an HIV transcriptional activator in various latency models[227].

3.3.2 Production of chemokines and vCCl

Purification of chemokines (both vMIP-II and CCL17) was carried out as reported previously.[55,158] The chemokine gene with a Thioredoxin tag followed by an enterokinase cleavage site on the N-terminus and a LPMTGHHHHHH tag on the C-terminus was transformed into *E. coli* BL21(DE3) cells (Novagen, Madison, WI, USA) and cultured at 37°C. When the cells' optical density OD600 reached ~0.7, protein expression was induced by adding IPTG to a final concentration of 0.5 mM and cells were allowed to grow for 18 hr at 22°C. Cells were harvested by centrifugation at 4400 × g, 4°C for 10 min. The cell pellet was then resuspended in lysis buffer (6 M Guanidine HCl, 200 mM NaCl, 50 mM Tris, 10 mM benzamidine, pH 8.0) and French pressed twice at 16,000 p.s.i. After centrifuging the lysate for 1 hr at 27,000 × g, the supernatant was purified by a home-packed Ni-NTA affinity column (Qiagen, Hilden, Germany). The protein was eluted with a pH gradient ending at pH 4. The purified protein was reduced with 10 mM β-mercaptoethanol (βME) at room temperature for 2 hours while stirring. Then the protein was added dropwise with a 10-fold dilution into refolding buffer (550 mM L-arginine hydrochloride, 400 mM sucrose, 9.6 mM NaCl, 0.4 mM KCl, 2 mM CaCl2, 2 mM MgCl2, 1 mM reduced glutathione (GSH), 0.1 mM oxidized glutathione (GSSG), 50 mM Tris, pH 8.0) and allowed to refold for 24 hr at 4°C with stirring. The protein was then dialyzed in

4L of high salt buffer (200 mM NaCl, 2 mM CaCl2, 20 mM Tris, pH 7.4) four times at 4°C. Subsequently the protein was cleaved using ~ 650 nM enterokinase for one to three days. (Due to low concentration of chemokine upon refolding and cutting at 4°C, higher concentrations of EK are used here.) Finally, the cleaved protein was purified by a C4 reversed phase chromatography column (Vydac, Hesperia, CA, USA) using an acetonitrile gradient.

vCCI was produced from E. coli as previously described.[20]

3.3.3 Construction of the enterokinase plasmids

The gene encoding the EK in the pUC57 vector is flanked by several restriction sites on the 5'-end (Xba I, Bgl II, and Nco I) and 3'-end (EcoR I, Sac I, Sal I, Hind III, Not I, Xho I, and BamH I) of the DNA. The EK gene was cloned into various pET expression plasmids by using the restriction sites of Nco I and BamH I to generate pET15b-EK, Nco I and Xho I to generate pET28a-EK, and Bgl II and Xho I to generate pET32a-EK. All constructs were verified by DNA sequencing to ensure correct sequences.

3.3.4 Expression of recombinant enterokinase

E. Coli BL21(DE3) cells were transformed with individual EK plasmids, and grown overnight on LB agar plates containing 50 µg/mL kanamycin for pET28a-EK, or 100 µg/mL ampicillin for pET15b-EK and pET32a-EK. Colonies from each plate were inoculated into 5 mL LB starter cultures containing antibiotics (50 µg/mL kanamycin or 100 µg/mL ampicillin) and grown in a shaker at 37°C, 220 rpm for several hours until the cultures reached log phase of growth. The starter cultures were then added into 1 L of pre-warmed LB (37°C) containing antibiotics and allowed to grow at 37°C, 220 rpm until reaching an O.D.600 of 0.6-0.8, at which protein production was initiated by the addition of IPTG (1 mM final concentration). After 4 hr, the cells were harvested by centrifugation at 4200×g, 4°C for 10 min and the supernatant was discarded. The harvested cell pellets were stored at -20°C.

3.3.5 Extraction and refolding of enterokinase

The harvested cell pellets were resuspended with 20 mL of Lysis Buffer (500 mM NaCl, 50 mM Tris, pH 8), and lysed by three passages through a French press at 16,000 psi (Thermo Fisher, PA). The resulting cell lysate was then centrifuged at 27,000×g, 4 °C for 1 hr. The supernatant was discarded, and the pellet was dissolved in 20 mL of Resuspension Buffer (6 M Guanidinium chloride, 200 mM NaCl, 50 mM Tris, pH 8) at room temperature for 2 hr with agitation. This mixture was then centrifuged at 27,000×g, 4 °C for 1 hr and the supernatant was collected. The supernatant was passed through a 3 mL home-packed Ni-NTA affinity column equilibrated with Resuspension Buffer. The column containing the bound EK was washed with 10 column volumes of Resuspension Buffer, and then with 10 column volumes of Wash Buffer (6 M Guanidinium chloride, 200 mM NaCl, 20 mM NaPi, pH 7.2). The EK was eluted from the Ni-NTA affinity column with Elution Buffer (6 M Guanidinium chloride, 200 mM NaCl, 60 mM NaOAc, pH 4). Fractions containing the eluted EK were identified by absorbance at 280 nm, or by SDS-PAGE after removal of guanidinium chloride by trichloroacetic acid (TCA) precipitation as described in the next paragraph.[238] The fractions were combined (5~10 mL total volume) and reduced with 5 mM DTT at room temperature for 2 hr with agitation. The solution was then added dropwise into a 15-fold volume of Refolding Buffer (700 mM L-Arginine hydrochloride, 1

mM EDTA, 200 mM NaCl, 50 mM Tris, pH 8, modified from FoldIt Screen, Hampton Research, Aliso Viejo, CA) and incubated overnight at 4 °C with gentle stirring.

For TCA (trichloroacetic acid) precipitation, all the samples and reagents are kept on ice throughout. 10µl of TCA is added into each 40µl of protein sample, and vortexed 5 seconds, then samples are placed on ice for 10 minutes. The samples are then centrifuged at 15k rpm for 5 minutes and placed back on ice immediately. The supernatant is then removed without disturbing the pellet (which may not be visible). The pellet is washed with 180µl ice-cold acetone and then centrifuged at 15k rpm for 5 minutes, and the supernatant is discarded; this wash step is repeated. The sample pellet is placed in a 60°C heat block for 10 seconds to evaporate the remaining acetone and 20µl of desired SDS-PAGE sample buffer is added. The sample is heated for 1 minute in a 95°C heat block before running SDS-PAGE.

3.3.6 Dialysis and concentration of enterokinase

After refolding overnight, trace amounts of precipitation in the refolded EK solution were removed by centrifuging at 3600×g, 4 °C for 10 min. The refolded EK solution was dialyzed against 4 L of EK Cleavage Buffer (200 mM NaCl, 2 mM CaCl2, 20 mM Tris, pH 7.5) at 4 °C. The buffer was changed every 8-10 hr. Active EK was obtained after 20 hr of dialysis, as evidenced by an SDS-PAGE gel showing the self-cleavage of its N-terminal fusion tag. Any precipitates were removed by centrifugation at 3600×g, 4 °C for 10 min. A stock solution of 5M NaCl was added to the EK solution to adjust the final concentration of NaCl to 500 mM. The EK solution was then loaded onto a 3 mL home-packed Ni-NTA affinity column equilibrated with Native Equilibration Buffer (500 mM NaCl, 20 mM Tris, pH 7.5). The column was then washed with 10 column volumes of Native Wash Buffer (500 mM NaCl, 20 mM Imidazole, 20 mM Tris, pH 7.5), and finally, the protein was eluted with a small volume (10~15 mL) of Native Elution Buffer (500 mM NaCl, 250 mM Imidazole, 20 mM Tris, pH 7.5). Fractions containing EK were identified by SDS-PAGE and combined. The final EK solution was added with glycerol to 50% (v/v), aliquoted into individual tubes, and stored at -20°C. For concentration determination, prior to addition of glycerol, the EK solution may be dialyzed against 500 mM NaCl, 20 mM Tris, pH 7.5, and then its absorbance measured at 280 nm. The concentration of EK can be calculated using an extinction coefficient of 55390 M-1 cm-1.[239]

3.3.7 Digestion of substrate proteins by EK

Substrate proteins Thioredoxin-KaiC 1-247 R41A K173A (Trx-KaiC) [240] and Thioredoxin-vMIP-II (Trx-vMIP)[155] were used to test the activity of EK. These proteins contain a thioredoxin fusion tag followed by a His6-tag and the EK recognition site (DDDDK↓). These substrate proteins were produced following procedures as previously described.[155,240] To test the EK activity, 500 µg of the substrate proteins were digested with various amounts of EK in 1mL Cleavage Buffer (200 mM NaCl, 2 mM CaCl2, 20 mM Tris, pH 7.5) at 4 °C and 25°C. The substrate proteins were quantified by measuring the absorbance at 280 nm, using the extinction coefficients of 30035 M-1cm-1 for Trx-KaiC and 33835 M-1cm-1 for Trx-vMIP.[239] Time point samples were taken and analyzed on 17% Tris-Glycine SDS-PAGE for Trx-KaiC, and 4-20% Mini-PROTEAN® TGXTM Gels for Trx-vMIP.

3.3.8 Production of the sortase enzyme from staphylococcus aureus

The gene for the sortase A enzyme was a gift of Dr. Archana Chavan, and was encoded with a 6-histidine tag on the N-terminus. This was transformed into E. Coli BL21(DE3) cells, and cells were grown in M9 minimal media in a shaker at 37 °C. Protein production was induced with IPTG (0.5 mM final concentration) at OD600 ~0.7. The temperature was reduced to 18°C and shaking continued overnight (16 hr). Cell pellets were collected by centrifugation for 10 min at 4400×g at 4°C. The pellets were resuspended with ~20 mL buffer A (150 mM NaCl, 50 mM Tris, 20 mM Imidazole, pH 7.5) and the cells lysed 3× using a French press at 16,000 psi. Lysate was clarified by centrifuging at 27,000 ×g, 4 °C for 1 hr. Then the clarified lysate was introduced to a home-packed Ni-NTA affinity column equilibrated with lysis buffer and passed through the column three times. The column was washed with 10 column volumes of buffer A, and then eluted with buffer B (150 mM NaCl, 50 mM Tris, 500 mM Imidazole, pH 7.5). The fractions containing His-Sortase A were identified by SDS-PAGE and combined followed by dialyzing in 4 L sortase buffer (150 mM NaCl, 50 mM Tris, pH 7.5) and then aliquoted and stored at -20°C. A 1 L prep can generally produce around 20 mL of 30 μM – 70 μM, which is about 20 mg protein per prep.

3.3.9 Labeling chemokine with fluorescein.

In order to obtain a high yield of chemokine-fluor, several related fusion tags on the C-terminus of the chemokines were tested using the sortase reaction, including LPMTGG, LPMTG-CHis, LPETG-CHis, and LPETG-2His. "CHis" is a 6-histidine tag, and "2His" is a 12 histidine tag, which was tested so that the cleavage of the tag during the reaction would be more easily visible on an SDS-PAGE gel due to the change in size of the starting protein. In our hands, the LPMTGHHHHHH tag could realize relatively high yield and had easy purification, while the others had lower yield and were more difficult to purify after the sortase reaction.

For the ligation of the fluorophore-peptide with the chemokine analog vMIP-II, 50 μM vMIP-II-LPMTG-CHis (powder was dissolved in sortase buffer (150 mM NaCl, 50 mM Tris, pH 7.5), 10 mM CaCl2, 5 μM His-Sortase A, and 150 μM GGGK5FAM (Bon Opus Biosciences) were incubated in the dark at 4°C for 2 days followed by incubating in ambient temperature for 17 hours. The time required for a sortase reaction is heavily dependent on the substrate, with some proteins requiring less (as little as a few hours) or more time (as much as 3 days). There is also a dependence on the particular amino acids used in the sortase tag on the same target protein.[241] The target protein vMIP-II-LPMTGGGK5FAM, was then purified through an analytical C4 reversed-phase chromatography column (Vydac, Hesperia, CA, USA), and verified by SDS-PAGE and mass spectrometry. The target chemokine-fluor was then aliquoted, then lyophilized and stored in the dark at -20°C. The protein was rehydrated in 20 mM potassium phosphate and 100 mM NaCl, pH 7.0 for fluorescence assays.

3.3.10 Fluorescence anisotropy.

The fluorescence anisotropy titration assays were performed in 20 mM potassium phosphate and 100 mM NaCl, pH 7.0, on a fluorimeter (PC1, ISS, Champaign, IL) (excitation: 498.4 nm, emission: 523.9 nm) at 25°C controlled by a water bath (VWR International, Visalia, CA). The reading of anisotropy was carried out with the excitation filter: 497/16, emission filter: 524/24 (BrightLine Fluorescence band pass filter). The

concentration of the vMIP-II-LPMTGGGK5FAM stock solution (buffer: 20 mM NaPi, pH 2.5) and vCCI stock (buffer: 100 mM NaCl, 20 mM NaPi, pH 7.0) were measured by the Coomassie (Bradford) Protein Assay Kit (Thermo Scientific Pierce). The vMIP-II-LPMTGGGK5FAM was diluted to a desired concentration in a beaker and mixed 1 min by shaking, and then 1990 µl was aliquoted into each cuvette and kept in the dark. Then, 10 µl of desired stock concentration of vCCI (in random order to remove possible bias from using a regular order) was added into one cuvette and mixed 1 min by shaking the cuvette in a 50 mL beaker. After that, the cuvette was incubated at 25°C for 30 min to allow equilibration before measurement. Anisotropy data were recorded, and upon hitting a plateau, the average data over 10 minutes was recorded, and all the anisotropy values were normalized to the proportion of 100% bound anisotropy value. The data were fit to a system of mass conservation equations that included the following equation as previously described[158]:

$$\theta = \frac{[L]_{free} \times K_a}{1 + [L]_{free} \times K_a} \quad \text{Eqn. 1}$$

where θ is the fraction of vMIP-II bound to vCCI, [L]free is the free vCCI concentration approximated by the total vCCI concentration, and Ka is the equilibrium association constant (1/Kd).

Binding constants using competition for the interaction between CCL17 and vCCI were obtained by titrating this ligand into a preformed complex of vCCI and vMIP-fluor at 8 nM[20]and observing the competition displacement of vCCI as a function of concentration at equilibrium via the observed change in anisotropy. The data were then normalized fit to a system of equations describing the conservation of species concentrations and both equilibria to yield the Kd for the CCL17:vMIP interaction using Scientist software (Micromath, St. Louis, MO).[158] The data were fit utilizing a Kd for vCCI:vMIP of 0.37 nM (found in this work) which yielded a Kd for vCCI:CCL17 of 16uM; then fit using a Kd for vCCI:vMIP of 0.06 nM (reported previously[55]) which yielded a very similar Kd for vCCI:CCL17 of 14uM. The rationale for using competition experiments as opposed to direct binding to measure the Kd for CCL17/TARC was that while this protein can be labeled with fluorophore as described for vMIP-II, the resulting peptide-fluor on the C-terminus of the protein was too mobile to provide useful anisotropy values upon directly binding vCCI. Therefore, it was used in its unlabeled form to compete for binding with vMIP-fluor.

3.3.11 Mass spectrometry.

The purified protein from the sortase reaction was collected after running it through a C4-reversed phase column and then lyophilized. To determine the mass of the intact protein, an aliquot of the purified protein was directly injected into an electrospray ionization mass spectrometer (ESI-MS) (Q-Exactive Hybrid Quadrupole-Orbitrap, Thermo Scientific). Additionally, some unpurified protein samples from the sortase reaction were diluted with 95% acetonitrile, 5% water, and 0.1% formic acid and then injected into a mass spectrometer coupled with an ultra-high performance liquid chromatography (UHPLC) system (Vanquish Flex, Thermo Scientific) at a flow rate of 0.3 ml/min for scouting purposes. The spectra, shown as signal intensity versus mass/charge, were analyzed using BioPharma 2.0 software (Thermo Scientific).

3.4 Results and Discussion

3.4.1 Expression and purification of CC chemokines.

CC chemokines have been easily expressed by a variety of methods for many years, so will only be briefly described here. Expression is usually effected using a T7 expression system (such as the pET system) in E. coli such as BL21(DE3), encoding the T7 RNA polymerase. Since solubility of the chemokine is sometimes limited in the supernatant of disrupted cells, it is often desirable to adjust disruption conditions to place the chemokine into the inclusion body, followed by dissolution of the inclusion body in 6M guanidinium chloride, or to simply disrupt the cells in 6 M guanidinium chloride. This is generally followed by a His-tag affinity column such as a Ni-NTA column, followed by refolding the semi-purified protein and dialysis. Since it is common to produce chemokines with an N-terminal fusion partner, this can be selectively cleaved at this point by an appropriate protease, such as by enterokinase (below) or by ULP-1 protease if the fusion tag is the SUMO protein.[20]Each of these proteases leaves no extra amino acids on the chemokine N-terminus upon cutting. Finally, CC chemokines are amenable to final purification by a C4 reversed phase column, which has the benefit of de-salting the protein (so that it can be lyophilized without other components like salts or buffer) and of removing bacterial endotoxins (which is important if the chemokine will be used in cell or animal studies).

For the present work, the CC chemokine homolog vMIP-II containing a C-terminal LPMTG sequence to allow eventual sortase labeling, was expressed with a Thioredoxin tag, partially purified using its His-tag with a Ni-NTA column, refolded, and finally purified with a C4 reversed phase column (Figure 3.1 and Supplementary Figure 3.1). The human CC chemokine CCL17/TARC was similarly expressed and purified. In each case, several milligrams per liter of pure protein were produced; the yield can be improved if necessary by using more of the semi-pure protein from the Nickel column, although this leads to very high volumes upon the dilution necessary for refolding.

3.4.2 Production of enterokinase.

Assuming a chemokine construct with an EK cleavage site (DDDDK↓), the cleavage step of chemokine purification can be efficient but costly if commercial sources of protease are used. To more easily obtain EK in the lab, we have developed a method to purify the human EK light chain from E. coli. The human EK gene was codon optimized for expression in *E. coli*, and flanked with various restriction sites to allow convenient subcloning into the pET vectors 15b, 28a and 32a (Figure 3.2A). Two of these vectors, pET15b-EK and pET28a-EK, confer different antibiotic resistance (ampicillin versus kanamycin, respectively), but produce an identical fusion EK protein. The third construct, pET32a-EK, expresses a thioredoxin fused to EK (Trx-EK).

The EK expressed using our designed pET15b-EK and pET28a-EK vectors contains an N-terminal tag (MGPINQTNDDDDK) that includes the EK cleavage site. This tag was incorporated as a tell-tale marker, as its self-cleavage from the initial fusion protein makes it easy to monitor successful production of mature, functional EK. The N-terminal tag is immediately followed by the catalytic subunit of human enterokinase, with a single Cys112Ser mutation which has been shown to improve refolding yield.[242] At the C-

terminus of the EK, a His6-tag was added, enabling the purification of EK by a simple Ni-NTA affinity column, as well as its convenient removal after cleaving a target protein.
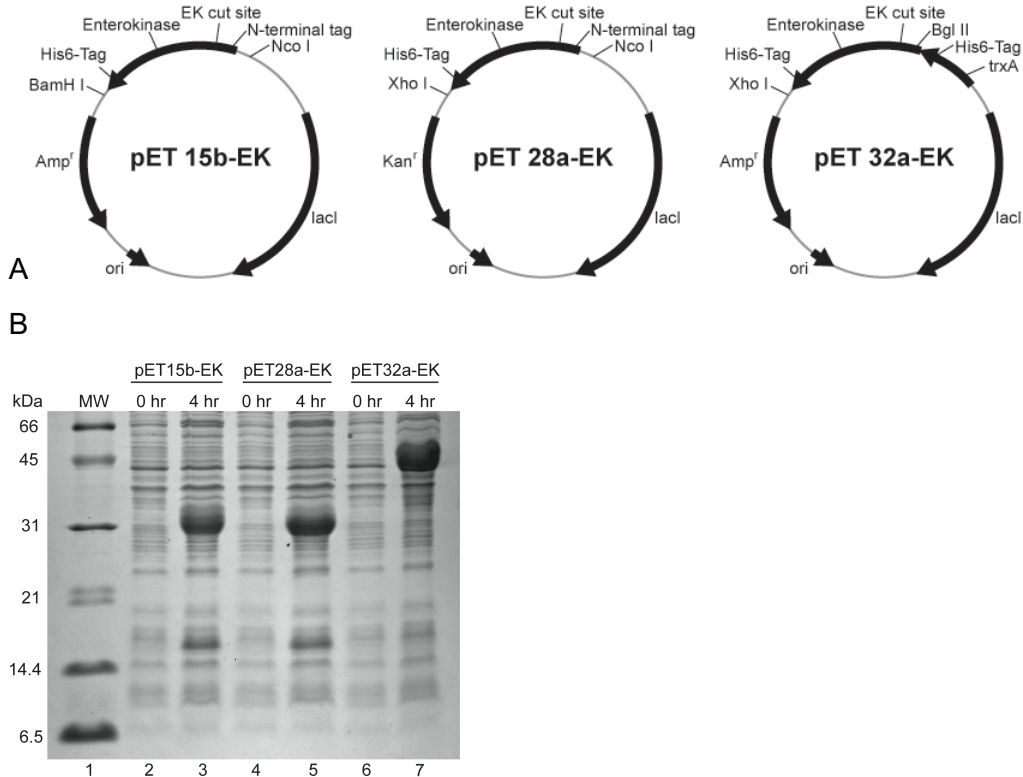
Figure 3.2 Expression vectors of enterokinase and protein expression test

A. Schematic representation of the enterokinase expression vectors pET15b-EK, pET28a-EK, and pET32a-EK. B. Expression of Enterokinase from various vectors in BL21 (DE3) cells at 37°C. Lane 1: Broad range molecular weight marker. Lane 2: Pre-induction time point of pET15b-EK. Lane 3: 4 h post-induction of pET15b-EK with 1 mM IPTG. Lane 4: Pre-induction time point of pET28a-EK. Lane 5: 4 h post- induction of pET28a-EK with 1 mM IPTG. Lane 6: Pre-induction time point of pET32a-EK. Lane 7: 4 h post-induction of pET32a-EK with 1 mM IPTG. The pET32a-EK has a thioredoxin fusion tag at the N-terminus of EK, resulting in a higher apparent molecular mass compared with the other two constructs.

EK expressed in pET32a-EK includes original components from the pET32a vector: starting from the N-terminus, there is a thioredoxin fusion partner (105 amino acid residues), followed by a His6-tag, an S-tag (the N-terminal 15 amino acids from RNase A that can be used in affinity purification) and an EK cleavage site. Following these components is the human EK catalytic subunit with the Cys112Ser mutation, then a C-terminal His6-tag. This thioredoxin fusion partner makes the self-cleavage of EK easier to monitor by SDS-PAGE. It is worth noting that by design, both the thioredoxin fusion partner and the final EK would each contain a His6-tag, so they would both bind to Ni-NTA beads. Therefore, the Trx-EK can be purified and self-cleavage of the Trx tag can occur, but no additional purification is needed before adding this to a solution with target protein, since both Trx and EK can be removed together by binding to Ni-NTA beads. In cases where the co-existing thioredoxin tag may raise concerns, EK produced by the pET15b-EK and pET28a-EK vectors may be preferred.

When expressed in E. coli BL21(DE3) cells, all the three constructs were able to produce EK at high levels as evidenced by SDS-PAGE (Figure 3.2B). Despite the difference in antibiotic resistance, no apparent difference in expression level was observed for pET15b-EK and pET28a-EK (Figure 3.2B, lanes 3 and 5). Due to the similarity in experimental procedures for purification of EK from each of these constructs, only the purification of the EK from pET28a-EK will be discussed here; this protein has a thirteen amino acid residue fusion tag at the N-terminus.
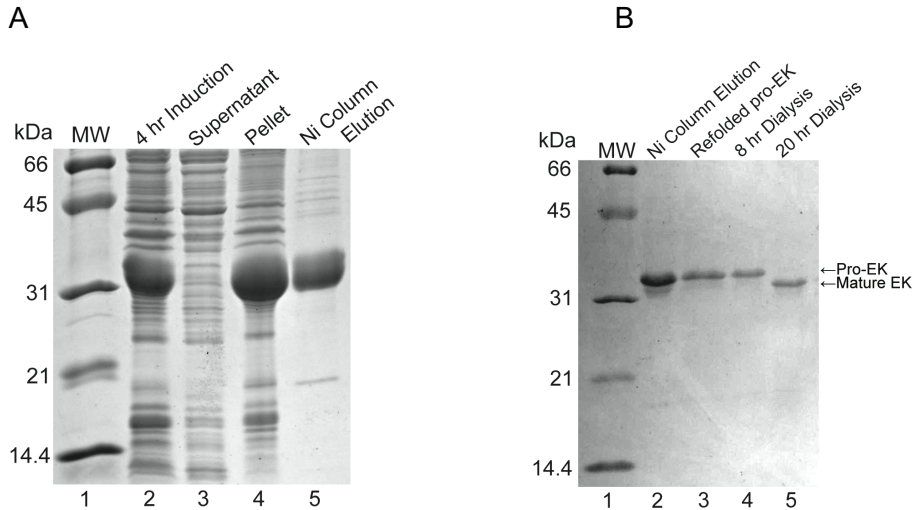
Figure 3.3 Enterokinase purification

A. Purification of enterokinase expressed by pET28a- EK using a Ni-NTA column. Lane 1: Broad range molecular weight marker. Lane 2: 4 h post-induction of pET28a-EK with 1 mM IPTG. Lane 3: Supernatant of cell lysate. Lane 4: Pellet of cell lysate. Lane 5: Elution from Ni-NTA column with pH 4 Elution Buffer containing a denaturing concentration of guanidinium chloride. TCA precipitation was performed to remove guanidinium chloride before preparation of gel samples. B. Self-cleavage of the N-terminal tag during dialysis to produce mature EK. Lane 1: Broad range molecular weight marker. Lane 2: Elution from Ni-NTA column by pH 4 Elution Buffer. Lane 3: pro-EK after the refolding procedure and before the start of dialysis. Lane 4: Refolded pro-EK after 8 h of dialysis. Dialysis Buffer was changed once after the first 8 h. Lane 5: Self-cleaved, mature EK after 20 h dialysis. Samples containing guanidinium chloride were processed by trichloroacetic acid (TCA) precipitation.

To summarize the purification of expressed EK, the cell pellet was resuspended in a Lysis Buffer containing a high concentration of NaCl (500 mM) to drive the EK fusion protein into the lysate pellet (Figure 3.3A, lanes 3 and 4). After cell disruption, this pellet was re-solubilized with buffer containing guanidinium chloride to extract tagged EK in an unfolded form. The crude supernatant was twice passed through a Ni-NTA affinity column and the EK was eluted by guanidinium chloride buffer at pH 4. Analysis by SDS-PAGE revealed that the EK was purified to around 90% purity after this step (Figure 3.3A, lane 5). To correctly fold EK into its native, functional tertiary structure, the purified EK was first fully reduced to break any disulfide bonds that may have formed, then the protein solution was refolded as described in Methods and dialyzed in cleavage buffer where self-cleavage to remove the N-terminal tag is observed (Figure 3.3B, lane 5).

A

B
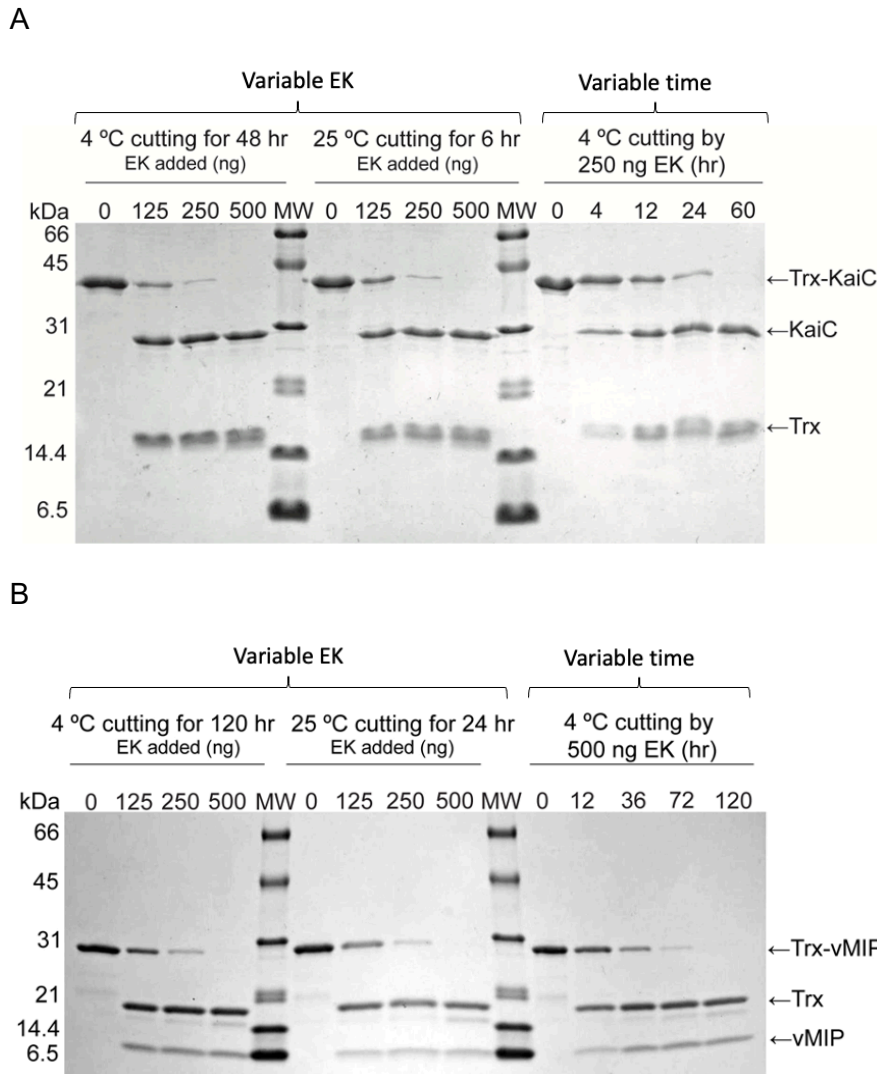
Figure 3.4 Enterokinase cleavage test

A. Cleavage reaction of the Trx-KaiC fusion protein by EK. Samples containing 500 μg of Trx-KaiC in 1 mL Cleavage Buffer with various amounts of EK were incubated at 4 or 25°C. Left set: 4°C for 48 h with 0, 125, 250, and 500 ng of EK. Middle set: 25°C for 6 h with 0,125, 250, and 500 ng of EK. Right set: Time course of 0, 4, 12, 24, and 60 h at 4°C with a fixed amount (250 ng) of EK. B. Cleavage reaction of the Trx-vMIP fusion protein by EK. Samples containing 500 μg of Trx-vMIP in 1 mL Cleavage Buffer with various amounts of EK were incubated at 4 or 25°C. Left set: 4°C for 120 h with 0, 125, 250, and 500 ng of EK. Middle set: 25°C for 24 h with 0, 125, 250, and 500 ng of EK. Right set: Time course of 0, 12, 36, 72, and 120 h at 4°C with a fixed amount (500 ng) of EK.

The matured EK was purified once more by loading the solution onto a Ni-NTA affinity column, and eluting with a small volume of buffer that contained 250 mM Imidazole, resulting in concentrated EK solution that could be used as a stock. Determined by absorbance at 280 nm, approximately 2 mg of active EK was purified from a 1 L E. coli

prep. Note that this amount of protease is sufficient for the needs of most labs for several months but could be optimized for higher yields if desired. The final EK product was stored in 50% glycerol (v/v) at either -20°C or -80 °C. No special procedure was used to remove the imidazole, as upon usage, the EK solution will be diluted by at least several hundred-fold when added into a target protein, and it has been shown that moderate concentrations of imidazole do not appear to affect the proteolytic activity of EK.[243]

3.4.3 Digestion of substrate fusion proteins with EK

To test the functionality of the purified EK, two recombinant proteins, each with an N-terminal thioredoxin fusion tag followed by an EK cleavage site, were chosen as substrates. vMIP-II is a small viral chemokine homolog of 8 kDa[154,155] that will be used in fluorescent labeling (below), and the 26 kDa domain of KaiC is from a critical circadian clock protein.[240] For the cutting reaction, 500 µg of Trx-vMIP-II or Trx-KaiC in 1 mL of EK cutting buffer were digested with increasing amounts of enterokinase, with the mass ratio of substrate protein to EK kept at or above 1000:1 (125, 250 and 500 ng EK). In research labs, cutting reactions for recombinant proteins are frequently carried out either at room temperature, or at a colder temperature to limit bacterial or fungal growth when the cutting takes a longer period of time. To determine functionality under these conditions, the test cutting reactions were carried out at 25 °C and 4 °C. Time point samples were taken periodically and analyzed by SDS-PAGE (Figure 3.4A, B). The results showed that the time needed to achieve complete proteolytic cleavage for each substrate protein differed. 500 µg of Trx-KaiC was completely cleaved by 500 ng of EK in 48 hours at 4 °C, or in 6 hours at 25 °C (Figure 4A, left and middle section). For 500 ng of EK to completely cleave 500 µg of Trx-vMIP, the time needed was about 120 hours at 4 °C, or 24 hours at 25 °C (Figure 3.4B, left and middle section).

Although the purification of active recombinant EK has been reported previously by several groups,[244–246] we have made significant improvements on the production method, presenting a streamlined protocol that produces functional EK in as little as four days. The current protocol bypasses many drawbacks in previous reported methods, without the requirement of complicated multi-buffer exchange before initiation of refolding, or an extensive incubation period during the refolding process, or usage of multiple columns or specialized (and potentially expensive) affinity columns. In contrast to eukaryotic systems such as P. pastoris and S. pombe, our current method produces EK using the E. coli expression system, which greatly simplifies and expedites steps involved in plasmid construction and modification, transformation of expression host cells, and convenient induction of high levels of protein expression, which in turn, should make homemade EK readily accessible for most research labs.

3.4.4 Production and use of the sortase enzyme from staphylococcus aureus.

There are several strategies that can be used to fluorescently label proteins for subsequent biophysical experiments. Direct chemical reaction with a fluorophore can be carried out, generally using the free thiol group of Cys or the amino group of Lys.[158,247] This can be an effective strategy, but maintaining a free thiol in a protein that also has disufides can be difficult, while labeling amino groups can lead to a variety of fluorescently labeled sites since a typical protein will have several Lys residues. For smaller proteins that can be entirely synthesized by solid phase synthesis, there is also the possibility of chemical steps added to the synthesis that allow conjugation of a fluorophore to the site

of interest. This latter method has been shown to be successful with variants of the chemokine CCL5.[165] We chose to use enzymatic methods to fluorescently label our chemokines, due to the specificity of the enzyme used (sortase) and the simplicity of making all components with bacterial expression. The sortase enzyme has the ability to cleave a protein at a specific site (cleavage occurs after the T in LPXTG, where X can be any amino acid), and then covalently add a peptide or protein (that has an N-terminal series of glycines) to the LPXT sequence.[241,248] When this procedure is applied to a chemokine bearing LPMTG at its C-terminus, adding to the reaction the peptide GGGK-fluor, the product is: Chemokine-LPMTGGGK-fluor. The utility of the sortase enzyme has been described for a variety of functions.[248–250] Briefly, the enzyme can be expressed in E. coli and purified with a single nickel column, then aliquoted for storage after brief dialysis (Figure 3.5).
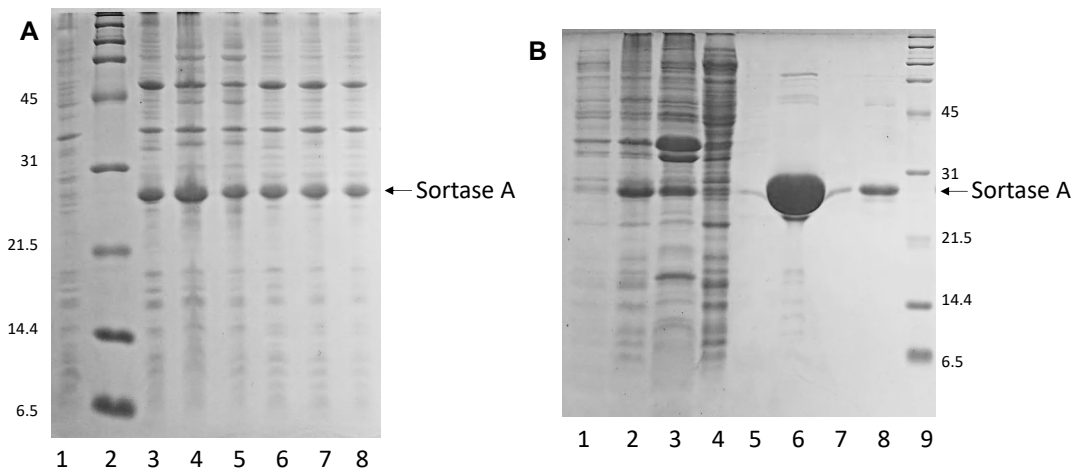
Figure 3.5 Expression and purification of sortase

A. Expression of sortase in BL21 (DE3) cells at 37 and 22°C. Lane 1: Pre-induction. Lane 2: Molecular weight marker. Lane 3: 3 h post-induction at 37°C. Lane 4: 5 h post-induction at 37°C. Lane 5: 7 h post-induction at 37°C. Lane 6: 16 h post-induction at 22°C. Lane 7: 18 h post-induction at 22°C. Lane 8: 20 h post-induction at 22°C. B. Purification of sortase A with a Ni-NTA column. Lane 1: Pre-induction. Lane 2: 5 h post-induction at 37°C. Lane 3: Pellets after lysing. Lane 4: Ni-NTA column flow through. Lane 5: Ni- NTA column wash. Lane 6: Elution 1 from Ni-NTA. Small amounts of impurities from E. coli proteins are observed if a large loading amount is used. Lane 7: Further elution from Ni-NTA. Lane 8: Result of further size exclusion column which is no longer used in lab due to sufficient purity after Ni-NTA column. Lane 9: Molecular weight marker.

When using sortase, the reaction should occur in the dark using foil to wrap the reaction tube, and it is advisable to set up several small scale (200 µL) test reactions to determine the optimal conditions for the ligation, including temperature and time scale. Once suitable conditions are obtained, larger scale reactions can be carried out, at sufficient scale to allow purification afterward. In our hands, reaction amounts of 2 mL containing 50µM chemokine were used, with the reaction requiring several days for optimal efficiency (although others report a wide range of time scales from hours to days[241,251]). Following the sortase reaction, the labeled chemokine can be purified using reversed-phase chromatography (Figure 3.6A). Figure 6C shows an SDS-PAGE gel of the various fractions after reversed phase chromatography, and also shows the same gel under UV light to illuminate the successful fluorescent labeling of the chemokine. If further evidence of purification of the correct labeled product is desired, mass spec can also provide this (Figure 3.6B).
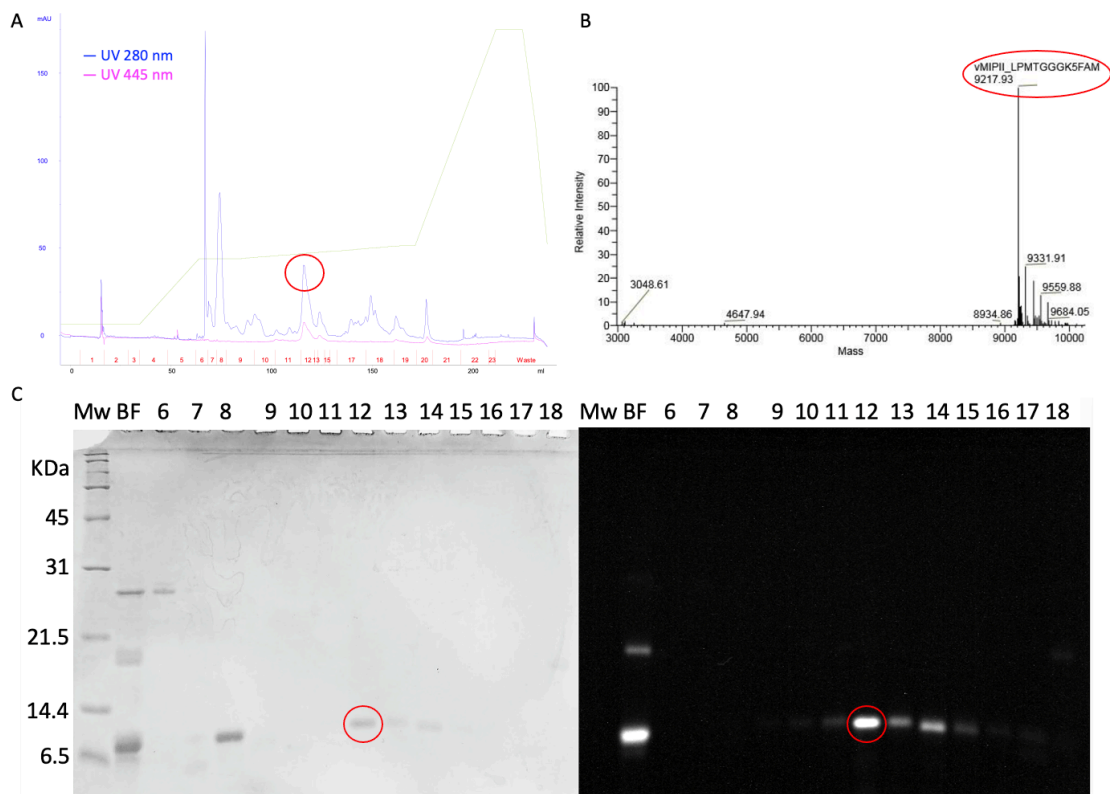
Figure 3.6 Purification of vMIP-II-fluor after the sortase reaction

A. Analytical C4 column trace after the sortase reaction. The two large early peaks are the sortase and unreacted chemokine respectively. The peak for the correctly labeled chemokine is circled. B. C4 fraction 12 verified as vMIP-II-fluor by mass spectrometry. The major peak on the mass spectrum is the expected size after reaction with the fluorophore. The smaller peaks at slightly higher molecular weight correspond to the protein-fluor adduct with trifluoroacetic acid that was used in the purification process. C. (Left)The SDS-PAGE gel of the fractions from the analytical C4 column. Left lane is the molecular weight marker, second lane is the sortase reaction before the C4 column, followed by fractions of the C4 column. (Right) The same gel, in the presence of UV light. The overall yield from the sortase reaction is about 20%.

3.4.5 Fluorescently labeled vMIP-II tightly binds vCCI and competes with CCL17/TARC.

The fluorescently labeled chemokine can be used in many types of assays, as fluorescence spectroscopy is an effective technique to measure binding across orders of magnitude of affinity. Binding can be measured by observing fluorescence intensity, fluorescence anisotropy, and fluorescence correlation (and cross-correlation) spectroscopy, the latter of which has been used to study chemokine binding to the CCR5 receptor.[165] For the in vitro binding of a small chemokine with a larger binding partner (such as vCCI), fluorescence anisotropy is an effective tool that can be carried out in a cuvette or plate reader, and can also be used in a competition experiment where an unlabeled chemokine competes with a labeled chemokine for binding to vCCI. It should be noted that a plate reader can be quite convenient in its ability to measure all the data points of a titration at once, although it tends to have lower sensitivity than the larger path length of a cuvette. We proceeded with fluorescence anisotropy experiments. As shown in Figure 7A vCCI is titrated into a solution containing vMIP-fluor, revealing sub-nanomolar binding with a Kd = 0.37±0.006 nM. Further, when a vCCI:vMIP-fluor complex is preassembled, a competition experiment can be carried out to determine binding constants of unlabeled chemokines as they compete with vMIP-fluor for the vCCI binding site. As shown in Figure 7B, CCL17 (also known as TARC) requires high concentrations to effectively compete with vMIP-fluor, demonstrating a binding constant of 14 μM. This chemokine has been implicated in several inflammatory disorders, such as allergic asthma and atopic dermatitis.[252,253] CCL17 had been previously used in qualitative assays which did suggest low binding to vCCI,[157] but fluorescence spectroscopy allows a quantitative assessment. Higher throughput is also easily achieved with these modified chemokines as 96 well plates can be used for multiple simultaneous binding assays (data not shown).

3.5 Conclusions

In conclusion, we describe techniques and constructs that allow the efficient and inexpensive production and purification of fluorescently labeled chemokines. The elements involved are broadly applicable to other proteins. Three options are presented for the production of recombinant enterokinase, which is used to specifically cleave fusion protein from a target; these varying constructs allow a variety of choices in antibiotic during expression of enterokinase and maintain a simple purification thereafter. The straightforward production of the sortase enzyme allows fluorescent labeling of a target protein if the target protein contains a simple 5 amino acid tag, which again can be applied in a wide variety of experimental systems. As an example of the utility of these toolkit proteins, we show their application in the chemokine system. It is demonstrated that chemokines can be expressed, purified and fluorescently labeled efficiently. Overall, this set of techniques can be used in a wide variety of experiments where proteins are expressed with fusion partners and there is additionally the desire to fluorescently label them inexpensively.

Chapter 4

A Combined Molecular Dynamics and Biophysical Approach to Studying The Chemokine Binding Properties of Viral Protein vCCI

4.1 Abstract

vCCI, the viral CC chemokine inhibitor encoded by rabbitpox virus, has a remarkable ability to bind almost all CC chemokines, many with nanomolar or sub-nanomolar affinity. This binding abrogates the ability of CC chemokines, many of which are pro-inflammatory, to bind and activate their cognate receptors on leukocytes. Therefore, understanding the basis of vCCI's binding ability could provide guidance on the design of anti-inflammatory therapeutics. In the current work, a combination of molecular dynamics and biophysical characterization was used, first determining likely important contacts between vCCI and its chemokine binding partners, then mutating these in vCCI. Binding of the wild type and variant vCCI was assessed by fluorescence anisotropy and NMR, using as a binding partner vMIP-II, a virally expressed chemokine homolog having the highest reported affinity for vCCI. Our results show that despite previous reports of poor binding, the Y80A vCCI variant still retains sub-nanomolar binding. However, molecular dynamics simulations suggest that the binding loop of this variant may transiently close and block the active site before chemokine binding, which is supported by experiments showing a reduced on-rate for the chemokine. Similarly, the R89A mutation of vCCI was predicted by MD to alter the action of the binding loop, and this variant showed a 12-fold reduction in chemokine on-rate. Overall, this work is a combination of biophysical techniques and molecular dynamics to pinpoint sites in vCCI that are involved in chemokine binding, including those that are indirectly involved due to allowing control of the active site loop of vCCI. This work is useful as part of a strategy to understand and design specific chemokine binding ability.

4.2 Introduction

Viruses have many techniques to evade the host immune system. These range from obscuring their surface with glycosylation to avoid antibodies[117], to producing decoy proteins[71,254] to producing proteins that actively subvert the immune system (for reviews see [73,74,255]). One example of the latter strategy is the production of chemokine binding proteins, which is a common feature of poxviruses [256], Many types of poxviruses produce a broadly-acting chemokine binding protein called vCCI (viral CC chemokine Inhibitor; also called "35K". Other viruses also produce a wide array of chemokine binding proteins, some having structural similarity to vCCI[255]; and other organisms such as ticks have also evolved a variety of proteins to bind chemokines to assist their own goals[257].

Binding and inhibiting chemokines is important both as a strategy for immune evasion, and also biomedically as a potential strategy to reduce an inflammatory immune response. Chemokines are small (about 70 amino acid) immune proteins that bind 7-transmembrane G-protein coupled receptors on the surface of leukocytes. This binding event leads to activation and chemotaxis of the immune cell, which can either lead to

maturation and homing (mediated by certain chemokine subsets) or inflammation at a site of injury or infection [56]. Chemokines also bind glycosaminoglycans, allowing them to set up a concentration gradient on the endothelial surface so that immune cells can migrate to an appropriate site. Chemokines have been subdivided into four subfamilies, based on the placement of conserved cysteines near the N-terminus; while all chemokines have essentially the same overall fold, each subfamily member binds receptors that largely restrict binding to members of that subfamily.

So-called CC chemokines have contiguous placement of two cysteines near their N-terminus, and several of these are important mediators of inflammation. For example, CCL2/CCR2 signaling regulates macrophage recruitment during inflammation [258]; CCL5 has been shown to mediate eosinophil, neutrophil and monocyte recruitment to the airways and trigger allergic airway inflammation[259].

vCCI proteins have been found in many poxviruses and have a very high sequence identity (Figure 4.1; the sequences shown range from 82% to 99%). These proteins form a beta sandwich, with the chemokine binding site on one face, and having an acidic loop that acts as a "lid" on the binding site, contacting and holding the chemokine in place upon binding. Chemokines tend to use multiple basic residues in specific locations on their surface to interact with both the binding site of vCCI and with its negatively charged loop[93,260,261]. Interestingly, vCCI has been shown to bind dozens of CC chemokines from various species with high affinity, showing low or no affinity to chemokines from other subfamilies such as CXC chemokines[115,116]. The basis of this broad binding ability has been studied structurally and biophysically, with some key residues being identified for their importance to chemokine binding[87,260,262]. For example, the vCCI acidic loop (between β2 and β3) has broad interaction with CC chemokine basic residues of 20s and 40s region. In addition, the vCCI negatively charged β sheet II shows interaction with CC chemokine's positively charged residues on the chemokine N loop, 20s region and 40s loop. The conserved hydrophobic residue of CC chemokine at 13th position was found to fit in a hydrophobic pocket between β sheet I and II of vCCI.

Some vCCI variants have behaved differently than the available structures would suggest[87,260]. For example, two residues in vCCI (Y80 and R89) appear to protrude into the chemokine binding site, sterically interfering with chemokine binding. Indeed, this seemed to be confirmed in vCCI from mousepox, where it was shown that the equivalent of a Y80R variant (Y69R in mousepox numbering) had lower affinity than the wild type of protein, presumably because of the positioning of a large, positively charged arginine in a location that was sterically crowded and in proximity to positive charges on the chemokine surface[87]. It was hypothesized that mutating Y80 to a smaller Ala would allow greater access by the chemokine and higher affinity. However, when the Y80A mutation was made in variola vCCI, rather than relieving crowding and showing increased chemokine affinity, the protein showed complete loss of ability to bind chemokine CCL5 to inhibit its function[262].

β1   β2

```
RPV   MPASLQQSSSSSSSCTEEENKHHMGIDVIIKVTKQDQTPTNDKICQSVTEITESESDPDP   60
EMV   IPTSLQQSFA--SSCTEEENNHHMGIDVIIKVTKQDQTPTNDKICQSVTEVTESEDDGVS   58
MPV   MPTS-LQ--QSSSSCTEEENKHHMGIDVIIKVTKQDQTPTNDKICQSVTEVTETEDDEVS   57
VAR   MPASLQQS---SSLCTEEENKHYMGIDVIIKVTKQDQTPTNDKICQSVTEITESES--DP   55
VVL   MPASLQQSSSSSSSCTEEENKHHMGIDVIIKVTKQDQTPTNDKICQSVTEITESESDPDP   60
VVC   VPASLQQSSSSSSSCTEEENKHHMGIDVIIKVTKQDQTPTNDKICQSVTEITESESDPDP   60
CPV   IPTSLQQSFSSSSSCTEEENKHHMGIDVIIKVTKQDQTPTNDKICQSVTEVTESED--ES   58
CMLV  MPASLQQS---SSSCTEEENKHHMGIDVIIKVTKQDKTPTNDKICQSVTENTESESDPDP   57
HSPV  MPAS-LQSFSSSSSCTEEENKHHMGIDVIIKVTKQDQTPTDDKICQSVTEVTETKDDEVS   59
      :*:*   *        *  *****:*:**************:***:********* **::.
```

β3   β4   β5   β6

```
RPV   EVESEDDSTSVEDVDPPTTYYSIIGGGLRMNFGFTKCPQIKSISESADGNTVNARLSSVS   120
EMV   EE---------VVKGDPTTYYTVVGGGLRMNFGFTKCPQIKSISESADGNTVNARLSSVS   109
MPV   EE---------VVKGDPTTYYTIVGAGLNMNFGFTKCPKISSISESSDGNTVNTRLSSVS   108
VAR   EVESEDDSTSVEDVDPPTTYYSIIGGGLRMNFGFTKCPQIKSISESANGNAVNARLSSVP   115
VVL   EVESEDDSTSVEDVDPPTTYYSIIGGGLRMNFGFTKCPQIKSISESADGNTVNARLSSVS   120
VVC   EVESEDDSTSVEDVDPPTTYYSIIGGGLRMNFGFTKCPQIKSISESADGNTVNARLSSVS   120
CPV   EE---------VVKGDPTTYYTVVGGGLTMDFGFTKCPKISSISEYSDGNTVNARLSSVS   109
CMLV  EVESEDDFTSVEDVDPPTTYYSIIGGGLRMNFGFTKCPQIKSISESADGNAVNARLSSVS   117
HSPV  EE---------VVKRDPTTYYSIVGAGLNMNFGFTKCPKILSISESSDGNTVNARLSSVS   110
      *               *****::*.** *:*:*******:* ****  ::**:**:*****
```

α1   β7

```
RPV   PGQGKDSPAITHEEALAMIKDCEVSIDIRCSEEEKDSDIKTHPVLGSNISHKKVSYEDII   180
EMV   PMYGIESPAITHEEALAMINDCAVSINIKCSEEEKDSNIKTHPVLGSNISHKKVRYEDII   169
MPV   PGQGKDSPAITREEALAMIKDCEMSIDIRCSEEEKDSDIKTHPVLGSNISHKKVSYKDII   168
VAR   PGQGKDSPAITRVEALAMIKDCELSIDIRCSEEEKDSDIQTHPVLESNISHKKVSYEDII   175
VVL   PGQGKDSPAITREEALAMIKDCEVSIDIRCSEEEKDSDIKTHPVLGSNISHKKVSYEDII   180
VVC   PGQGKDSPAITREEALAMIKDCEVSIDIRCSEEEKDSDIKTHPVLGSNISHKKVSYEDII   180
CPV   PGQGKDSPAITREEALSMIKDCEMSINIKCSEEEKDSNIKTHPVLGSNISHKKVSYEDII   169
CMLV  PGQGKDSPAITREEALAMIKDCEVSIDIRCSEEEKDSDIKTHPVLESNISHKKVSYEDII   177
HSPV  PGQGKDSPAITREEALAMIKDCEVSINIRCSEKEKDSDIKTHPVLGSNISHKKVSYEDII   170
      *   *  :*****: ***:**:**  :**:*:***:****:*:***** ******* *:***
```

β8   β9   β10   β11

```
RPV   GSTIVDTKCVKNLEFSVRIGDMCKESSELEVKDGFKYVDGSASKGATDDTSLIDSTKLKACV   242
EMV   GSTIVDIKCVKDLEFSVRIGDMCKEASELEVKDGFKYIDGSVSEGATDDTSLIDSTKLKACV   231
MPV   GSTIVDTKCVKNLEFSVRIGDMCEESSELEVKDGFKYVDGSASEGATDDTSLIDSTKLKACV   230
VAR   GSTIVDTKCVKNLEFSVRIGDMCKESSDLEVKDGFKYVDGSVSEGVTDDTSLIDSTKLKSCV   237
VVL   GSTIVDTKCVKNLEFSVRIGDMCKESSELEVKDGFKYVDGSASEGATDDTSLIDSTKLKACV   242
VVC   GSTIVDTKCVKNLEFSVRIGDMCKESSELEVKDGFKYVDGSASEGATDDTSLIDSTKLKACV   242
CPV   GSTIVDTKCVKNLEISVRIGDMCKESSELEVKDGFKYVDGSASEDAADDTSLINSAKLIACV   231
CMLV  GSTIVDTKCVKNLEFSVRIGDMCKESSDLEVKDGFKYVDGSASEGATDDTSLIDSTKLKACV   239
HSPV  GSTIVDTKCVKNLEFSVRIGDMCKESSELEVKDGFKYVDGSASKGATDNTSLIDSTKLKACV   232
      ****** ****:**:*********:*:*:*********:***.*:...:*:****:*:** :**
```

Figure 4.1 vCCI sequence alignment

RPV: Rabbitpox virus; EMV: Ectromelia virus; MPV: Monkeypox virus; VAR: Variola virus; VVL: Vaccinia virus Lister strain; VVC: Vaccinia virus Copenhagen strain; CPV: Cowpox virus; CMLV: Camelpox virus ;HSPV: Horsepox virus.

Understanding the detailed interaction of vCCI with its various CC chemokine substrates can potentially allow the tailoring of vCCI's binding interactions toward specific purposes in specific situations, such as controlling inflammation during an asthma attack or in traumatic brain injury, both of which have a chemokine component [69,263,264].

Molecular dynamics is a powerful technique that can be brought to bear on important protein-protein interactions such as those made by vCCI as it binds its chemokine substrates. Molecular dynamics can be particularly helpful in situations where there is a disparity between structural observations and biological experiments.

We have combined an in silico molecular dynamics treatment of vCCI binding with experiments on wild type and mutant vCCI, to provide a more complete picture of the binding surface and important interactions made by vCCI.

4.3 Materials and Methods

4.3.1 Protein Expression and Purification

4.3.1.1 vCCI and its variants

Rabbit pox vCCI was constructed as described previously [261], containing an N-terminal Thioredoxin tag and a His tag, followed by an enterokinase cutting site. For efficiency of the enterokinase protease, the first two amino acids of vCCI, Met-Pro, were replaced with Ala-Met-Ala. The vCCI Y80A variant was constructed by PCR; other mutations, including vCCI R89A, vCCI E143K, vCCI I184R, vCCI Y80R, vCCI triple mutant (Y80R/E143K/I184R) were synthesized by Twist Bioscience (San Francisco, CA). The vCCI wild type and Y80A variant were made using the pET-32a(+) expression vector from Novagen (Madison, WI) while other mutants were made using the Novagen pET-28a(+) plasmid.

Purification of rabbit pox vCCI was carried out as reported previously [261] with slight modifications. vCCI and its variants' plasmids were transformed into E. coli BL21(DE3) competent cells (Novagen) and expressed in Luria broth media or minimal media where 15NH4Cl as the exclusive nitrogen source. The cells were grown in a shaker at 37°C, and the inducing reagent isopropyl β-D-1-thiogalactopyranoside (IPTG; 0.5 mM) was added when OD600 reached around 0.7. The incubation continued in a shaker at 22°C for a further 20 hr. Then, the cell pellets were collected by centrifugation at 4400 × g, 4°C for 10 min followed by resuspending in lysis buffer 1 (6 M Guanidine HCl, 200 mM NaCl, 50 mM Tris, pH 8.0 and passed through a French press (Thermo Fisher, PA) twice at 16,000 p.s.i and centrifuged at 27,000 × g for 1 hr at 4°C. The supernatant was collected and frozen at -80°C overnight. Then the supernatant was centrifuged for additional 1 hr at 27,000 × g at 4°C to further pellet cell debris. At this point, the supernatant was collected and was reduced with 15 mM β-mercaptoethanol (βME) at room temperature for 2 hours while stirring. Meanwhile, a home-packed Ni-NTA affinity column (Qiagen, Hilden, Germany) was equilibrated with buffer A1 (6 M Guanidine HCl, 200 mM NaCl, 50 mM Tris, 15 mM βME, pH 8.0). The supernatant was then passed through the nickel column three times followed with washing with 10 column volumes of buffer A1, and then buffer B1 (6 M Guanidinium chloride, 200 mM NaCl, 15 mM βME, 80 mM sodium phosphate (NaPi), pH 7.2). After washing, the protein was eluted from the column with buffer C (6 M guanidine hydrochloride, 200 mM NaCl, and 60 mM sodium acetate (NaOAc), pH 4.0). The fractions were identified by the absorbance at 280nm and/or SDS-PAGE after removal of guanidinium chloride by trichloroacetic acid precipitation. Fractions containing vCCI were combined. The pH of the solution was then adjusted 8.0 and βME was added

to reach the final concentration of 25 mM. This was agitated at room temperature for 2 hours, followed by stirring at 4°C overnight.

The next day, the protein solution was dripped into 20 fold volume of refolding buffer (550 mM L-arginine hydrochloride, 400 mM sucrose, 9.6 mM NaCl, 0.4 mM KCl, 2 mM CaCl$_2$, 2 mM MgCl$_2$, 3 mM reduced glutathione (GSH), 0.3 mM oxidized glutathione (GSSG), 50 mM Tris, pH 8.0) for 24 hr at 4°C with stirring. Then, the protein solution was dialyzed 4 times in 4 L of high salt dialysis buffer (200 mM NaCl, 2 mM CaCl2, 20 mM Tris, pH 7.4) at 4°C. Enterokinase (produced in house, see below) was then added to the protein solution to a final concentration of 650nM to cleave the thioredoxin fusion tag for 24 hr. After cutting, the protein solution was dialyzed in 4 L of low salt buffer (50 mM NaCl, 20 mM Tris, pH 7.1) at 4°C followed by further purification on a HiTrapTM Q HP Column (GE Healthcare Life Sciences, Chicago, IL, USA), with a gradient separation from 50 mM NaCl, 20 mM Tris pH 7.1 to 1 M NaCl, 20 mM Tris pH 7.1. The fractions containing vCCI were verified on SDS-PAGE gel and dialyzed in 4 L of NMR buffer (100 mM NaCl, 20 mM NaPi, pH 7.0).

4.3.1.2 vMIP-II and its variants

Three vMIP-II proteins, vMIP-II wild type, vMIP-II-linker(GGSGS)-CHis(6 His-tag), vMIP-II-LPMTG-CHis, were used in this paper. Wild type vMIP-II has two constructs, His-Thioredoxin-vMIP-II (pET-32a(+) vector) and His-SUMO-vMIP-II (pET-28a(+) vector), and both lead to an identical target protein. vMIP-II-linker-CHis was constructed via PCR and was cloned into the pET-28a(+) vector with a SUMO fusion tag on the N terminus. vMIP-II-LPMTG-CHis (purchased from Twist Bioscience) was designed with a Thioredoxin tag followed by an enterokinase cutting site on the N terminus in a pET-28a(+) vector.

vMIP-II and its mutants were purified as mentioned previous [261] with some modification. The plasmid was transformed into E. coli BL21(DE3) cells and the cells were grown in a shaker at 37°C. When the optical density at 600nm reached ~ 0.7, protein expression was initiated by adding IPTG to a final concentration of 0.5 mM, and the cells were grown for 5 hr at 37°C and then harvested by centrifugation at 4400 × g, 4°C for 10 min. The pellet was collected and resuspended in lysis buffer 2 (6 M Guanidine HCl, 200 mM NaCl, 50 mM Tris, 10 mM benzamidine, pH 8.0) and French pressed twice at 16,000 p.s.i. After centrifugation at 27,000 × g for 1 hour at 4°C, the supernatant was passed three times onto a home-packed Ni-NTA affinity column equilibrated with buffer A2 (6 M Guanidine HCl, 200 mM NaCl, 50 mM Tris, pH 8.0). After that, the column was washed with 10 column volumes of buffer A2, and then buffer B2 (6 M Guanidinium chloride, 200 mM NaCl, 80 mM NaPi, pH 7.2). Proteins were then eluted from the column with buffer C (6 M guanidine hydrochloride, 200 mM NaCl, and 60 mM NaOAc, pH 4.0). The fractions containing vMIP-II were combined and brought pH to 8.0 followed by addition of the reducing reagent βME to a concentration of 10mM, and stirred at at room temperature for 2 hr. The protein solutions was then dripped into 10 × volume of ice-cold refolding buffer (550 mM L-arginine hydrochloride, 400 mM sucrose, 9.6 mM NaCl, 0.4 mM KCl, 2 mM CaCl$_2$, 2 mM MgCl$_2$, 1 mM reduced glutathione (GSH), 0.1 mM oxidized glutathione (GSSG), 50 mM Tris, pH 8.0) with stirring and the protein was allowed to refold for 24 hr at 4°C. After refolding, the protein solution was dialyzed against 4 liters of high salt dialysis buffer (as above). The cleavage of fusion tags and further purification is described below.

The protein with a Thioredoxin fusion tag was removed from dialysis and enterokinase was added to a concentration of 650nM. This was incubated for 24 hr at 4°C.

After enterokinase cleavage, an equal volume of water was added to the protein solution, followed by 0.2% TFA and 10% C4 buffer B (100% acetonitrile, 0.1% TFA). The protein solution was filtered (0.45 um) before loading to a C4 reversed-phase chromatography column (Vydac, Hesperia, CA, USA). The target protein was then eluted with an acetonitrile gradient. The fractions with the protein of interest were lyophilized for further usage.

The protein with a SUMO tag was cleaved by 100 nM of the Ubiquitin-Like Modifier Protease (Ulp-1; produced in house as noted below) for 24 hr at 4°C. The protein solution was then dialyzed in low salt buffer (50 mM NaCl, 20 mM Tris, pH 7.1) at 4°C , followed by purification on a HiTrap Heparin HP affinity column (GE Healthcare) to separate the SUMO fusion tag from the protein of interest with a gradient separation from 50 mM NaCl, 20 mM Tris pH 7.1 to 1 M NaCl, 20 mM Tris pH 7.1. The fractions containing target proteins were then analyzed on a SDS-PAGE gel and were further purified on a C4 reversed-phase chromatography column (Vydac, Hesperia, CA, USA), with an acetonitrile gradient as described above.

4.3.1.3 Enterokinase

The enterokinase (EK) gene was cloned into pET15b expression plasmid. E. Coli BL21(DE3) cells were transformed with the plasmid and cells were grown in a shaker at 37 °C for several hours until the cultures reached an OD_{600} ~ 0.7, at which protein production was initiated by the addition of IPTG (0.5 mM final concentration). After 4 hr, the cells were harvested by centrifugation at 4400×g, 4 °C for 10 min and the supernatant was discarded. The harvested cell pellets were stored at -20 °C. The harvested cell pellets were then resuspended in 20 mL of lysis buffer 3 (500 mM NaCl, 50 mM Tris, pH 8.0), and lysed using three passages through a French press at 16,000 psi. The resulting cell lysate was then centrifuged at 27,000 ×g, 4 °C for 1 hr. The supernatant was discarded, and the pellet (containing enterokinase) was dissolved in 20 mL of buffer A2 at room temperature for 2 hr with agitation. This mixture was then centrifuged at 27,000×g, 4 °C for 1 hr and the supernatant was collected. The supernatant was passed through a home-packed Ni-NTA affinity column equilibrated with buffer A2. The column containing the bound EK was washed with 10 column volumes of buffer A2, and then with 10 column volumes of buffer B2. The EK was eluted from the Ni-NTA affinity column with buffer C. Fractions containing the eluted EK were identified by absorbance at 280 nm, or by SDS-PAGE gel. The fractions were combined (5~10 mL total volume) and reduced with 5 mM dithiothreitol (DTT) at room temperature for 2 hr with agitation. The solution was then added dropwise into a 15-fold volume of refolding buffer (700 mM L-Arginine hydrochloride, 1 mM EDTA, 200 mM NaCl, 50 mM Tris, pH 8.0) and incubated overnight at 4 °C with gentle stirring.

After refolding 24 hr, trace amounts of precipitation in the refolded EK solution were removed by centrifuging at 4400×g, 4 °C for 30 min. The refolded EK solution was dialyzed against 4 L of high salt dialysis buffer (200 mM NaCl, 2 mM CaCl2, 20 mM Tris, pH 7.4) at 4 °C. Active EK was obtained after 20 hr of dialysis, as evidenced by the self-cleavage of its N-terminal fusion tag. Any precipitates were removed by centrifugation at 4400×g, 4 °C for 30 min. The EK solution was adjusted to a final concentration of NaCl to 500 mM. The EK solution was then loaded onto a home-packed Ni-NTA affinity column equilibrated with native equilibration buffer (500 mM NaCl, 20 mM Tris, pH 7.5). The column was then washed with 10 column volumes of native wash buffer (500 mM NaCl, 20 mM Imidazole, 20 mM Tris, pH 7.5), and finally, the protein was eluted with a small volume (~10mL) of

native elution buffer (500 mM NaCl, 250 mM Imidazole, 20 mM Tris, pH 7.5). Fractions containing EK were identified by SDS-PAGE and combined. The final EK solution was made to 50% (v/v) glycerol, and aliquoted into individual tubes, and stored at -20 °C. For concentration determination, prior to addition of glycerol, the EK solution may be dialyzed against 500 mM NaCl, 20 mM Tris, pH 7.5, and then its absorbance measured at 280 nm. The concentration of EK can be calculated using an extinction coefficient of 55390 $M^{-1}cm^{-1}$.

4.3.1.4 Ulp-1

The His-Ulp-1 plasmid (pET-28b(+)) was transformed into E. Coli BL21(DE3) cells followed by growing cells in M9 minimal media in a shaker at 37 °C, 220 rpm. Once the OD_{600} reached ~ 0.7, IPTG (0.5 mM final concentration) was added and the shaker temperature lowered to 25°C. After 12 hr, the cells were harvested by centrifugation at 4400×g, 4 °C for 10 min and the pellets were resuspended in lysis buffer 4 (500 mM NaCl, 50 mM NaPi, pH 8.0) and passed three times through a French press at 16,000 psi followed by centrifuging at 27,000 ×g, 4 °C for 1 hr. The supernatant was then passed through a home-packed Ni-NTA affinity column (equilibrated with lysis buffer 4) three times and washed with 10 column volumes of buffer A3 (500 mM NaCl, 50 mM NaPi, 25 mM imidazole, pH 8.0). The His-Ulp-1 was then eluted with buffer B3 (500 mM NaCl, 50 mM NaPi, 250 mM imidazole, pH 8.0). The fractions containing His-Ulp-1 were passed through a gel filtration column (HiLoad 16/60 Superdex 75, GE Healthcare) (buffer: 20 mM Tris, 500 mM NaCl, pH = 8.0). Finally, the His-Ulp-1 made to 50% glycerol (v/v) and stored at -80°C.

4.3.1.5 Sortase

The gene for His-Sortase A (strain: S. aureus; obtained from Prof. A. LiWang) was transformed into E. Coli BL21(DE3) cells, and cells were grown in M9 minimal media in a shaker at 37 °C, 220 rpm. Protein production was induced with IPTG (0.5 mM final concentration) at OD_{600} ~0.7. The temperature was reduced to 18°C and shaking continued overnight (16 hr). Cell pellets were collected by centrifugation for 10 min at 4400×g at 4°C. The pellets were resuspended with ~20 mL Buffer A4 (150 mM NaCl, 50 mM Tris, 20 mM Imidazole, pH 7.5) and the cells lysed 3X using a French press at 16,000 psi. Lysate was clarified by centrifuging at 27,000 ×g, 4 °C for 1 hr. Then the clarified lysate was introduced to a home-packed Ni-NTA affinity column equilibrated with Buffer A4, and passed through the column three times. The column was washed with 10 column volumes of buffer A4, and then eluted with Buffer B4 (150 mM NaCl, 50 mM Tris, 500 mM Imidazole, pH 7.5). The fractions containing His-Sortase A were identified by SDS-PAGE and combined, followed by dialyzing in 4 L sortase buffer (150 mM NaCl, 50 mM Tris, pH 7.5), and then stored at -20°C.

4.3.2 Labeling vMIP-II with 5FAM

C-terminal sortase mediated ligations were performed for the fluorescence labelling. For ligation, 50 µM vMIP-II-LPMTG-CHis (powder was dissolved in sortase buffer 150 mM NaCl, 50 mM Tris, pH 7.5), 10 mM $CaCl_2$, 5 µM His-Sortase A, and 150 µM GGGK5FAM (Bon Opus Biosciences) were incubated in dark at 4°C for 2 days followed with incubating in ambience temperature for 17 hours. The labelling reaction, the target protein vMIP-II-LPMTGGGK5FAM, was then purified through an analytical C4

reversed-phase chromatography column (Vydac, Hesperia, CA, USA), and verified by SDS-PAGE and mass spectrometry.

4.3.3 Fluorescence Anisotropy

The fluorescence anisotropy titration assays were performed in 20 mM potassium phosphate and 100 mM NaCl, pH 7.0, on a fluorimeter (PC1, ISS, Champaign, IL) (excitation: 498.4 nm, emission: 523.9 nm) at 25°C controlled by a water bath (VWR International, Visalia, CA). vMIP-II-LPMTGGGK5FAM stock solution (buffer: 20 mM NaPi, pH 2.5) and vCCI stock (buffer: 100 mM NaCl, 20 mM NaPi, pH 7.0) concentration was measured by the Coomassie (Bradford) Protein Assay Kit (Thermo Scientific Pierce). The vMIP-II-LPMTGGGK5FAM was diluted to a desired concentration in a beaker and mixed 1 min by shaking, and then aliquoted 1990 μl into each cuvette and kept in the dark. Then, 10 μl of desired stock concentration of vCCI (in random order to remove possible bias from using a regular order) was added into one cuvette and mixed 1 min by shaking the cuvette in a 50 mL beaker. After that, the cuvette was incubated at 25°C for 30 min to allow equilibration before measurement. Anisotropy data were recorded, and upon hitting a plateau, the average data over 10 minutes was recorded, and all the anisotropy values were normalized to XXX. The data were fit to an equation as before [116] [Nai-Wei paper]:

$$\theta = \frac{[L]_{free} \times K_a}{1 + [L]_{free} \times K_a}$$

θ is the fraction of vMIP-II bound to vCCI, [L]free is the free vCCI concentration, and Ka is the association constant which is the 1/Kd.

CLARIOstar multimode microplate reader (BMG Labtech) was also applied to record the vMIP-II fluorescence anisotropy change under titration of vCCI and its mutants over time. Aliquotes (90 μL) of vMIP-II-LPMTGGGK5FAM master mix were pipetted into black, non-binding 384-well microplates (Greiner BioOne), and 10 μL of vCCI with different concentration were added into each well. The plate was then incubated at 25°C for 30 min prior to measurement. Fluorescence polarization was measured in kinetic mode and fluorescence anisotropy data was calculated by CLARIOstar MARS software.

4.3.4 Mass spectrometry

The products of sortase ligation after analytical C4 reversed-phase chromatography column was identified by Mass spectrometry.

4.3.5 Nuclear Magnetic Resonance (NMR) Spectroscopy

All the NMR samples were prepared in 20 mM sodium phosphate buffer pH-7.0 containing 100 mM NaCl, 10% D_2O and 5μM 2,2-dimethyl-2-silapentane-5-sulfonic acid (DSS). ^{15}N-labeled lyophilized vMIP-II powder was dissolved in 20 mM sodium phosphate buffer, pH 2.5 to prepare a stock solution of the ^{15}N-vMIP-II protein. NMR sample of ^{15}N labelled-vMIP-II (50 uM) was prepared by dissolving in NMR buffer containing 20 mM sodium phosphate buffer, pH-7.0 and 100 mM NaCl. NMR samples for the complexes of ^{15}N labelled-vMIP-II and ^{14}N-VCCI mutant proteins were prepared by dissolving 15N-labelled-vMIP in the NMR buffer containing respective ^{14}N-VCCI mutant proteins ((VCCI_Y80A, Y80R, I184R, E143K, R89A, and Triple mutant).

All ^{1}H-^{15}N HSQC NMR experiments were carried out using a four-channel 600 MHz Bruker Avance III spectrometer equipped with TCI cryo probe. All the HSQC experiments

were performed at 37°C and were referenced with respect to internal DSS. NMR data was processed and analyzed using NMRPipe, Bruker Topspin 3.2 and CARA. For each HSQC spectra, spectral width of 14.09 ppm (8474.576 Hz) (^{1}H) and 29 ppm (1766.656 Hz) (^{15}N) with carrier frequencies set to 4.699 ppm and 119.498 ppm for ^{1}H and ^{15}N dimensions respectively. All the experiments were recorded using 1342 points in ^{1}H dimension and 350 points in ^{15}N dimension.

Chemical shift perturbation was calculated using the following equation:

$$\Delta\delta = \sqrt{(\Delta\delta_H)^2 + (\Delta\delta_N/5)^2}$$

Where, δH and δN are the chemical shift changes of the ^{1}H and ^{15}N dimensions, respectively. Here, the $\Delta\delta$ is the observed difference between bound and free form of ^{15}N-labeled complexes.

4.4 Results and Discussion

^{15}N NMR reveals differences in chemokine binding by vCCI variants. Six variants of rabbitpox vCCI were produced from E. coli and were purified as previously described[261]. Four of the variants were hypothesized to have reduced binding to chemokines (Y80R, E143K, I184R, and triple mutant Y80R/E143K/I184R); two have been hypothesized to enhance binding, but our MD simulations suggest these lead to changes in the motion of the binding loop which may impact binding (Y80A, R89A). Each vCCI variant was determined to be folded by NMR (data not shown). In order to obtain information on the chemokine interactions with these variants, ^{15}N-labeled vMIP-II (a chemokine analog made by herpesvirus that is known to tightly bind vCCI and to have favorable solubility under various conditions) was bound to ^{14}N-labeled vCCI, so that the resulting spectra showed the chemical shifts of the chemokine analog in the complex (Figure 4.2).

In general, vCCI variants with these three individual mutations did not show a profound effect compared to wild type vCCI in the perturbed residues upon complex with vMIP-II. However, the cumulative of effect of three individual vCCI variants was clearly observed in interactions between the vCCI triple mutant and vMIP-II. Differential vCCI variants with distinct mutations generally give perturbations in the major binding regions of vMIP-II, including in the N-terminal loop, second β-strand, and 50's regions. However, additionally perturbed residues that are specific to the individual vCCI variants were also observed.

^{1}H-^{15}N HSQC spectra of free ^{15}N-vMIP and in complex with different ^{14}N-vCCI variants (^{14}N-vCCI-Y80A, ^{14}N-vCCI-E143K,^{14}N-vCCI-R89A, ^{14}N-vCCI-I184R,^{14}N-vCCI-Y80R, ^{14}N-vCCI-TM (triple mutant- Y80R-E143K-I184R) were recorded and analyzed to measure the movement of peaks of ^{15}N-vMIP-II upon the complex formation (Figure 4.2). Assignment of peaks for the unbound form of ^{15}N-vMIP-II were obtained from BMRB (Biological Magnetic Resonance bank) entry 4914. Best possible assignments of peaks were made for bound form of ^{15}N-vMIP-II. Chemical shift perturbation values for each residue were determined (Figure 4.3, Figure 4.4, Supplementary Figure 4.1).
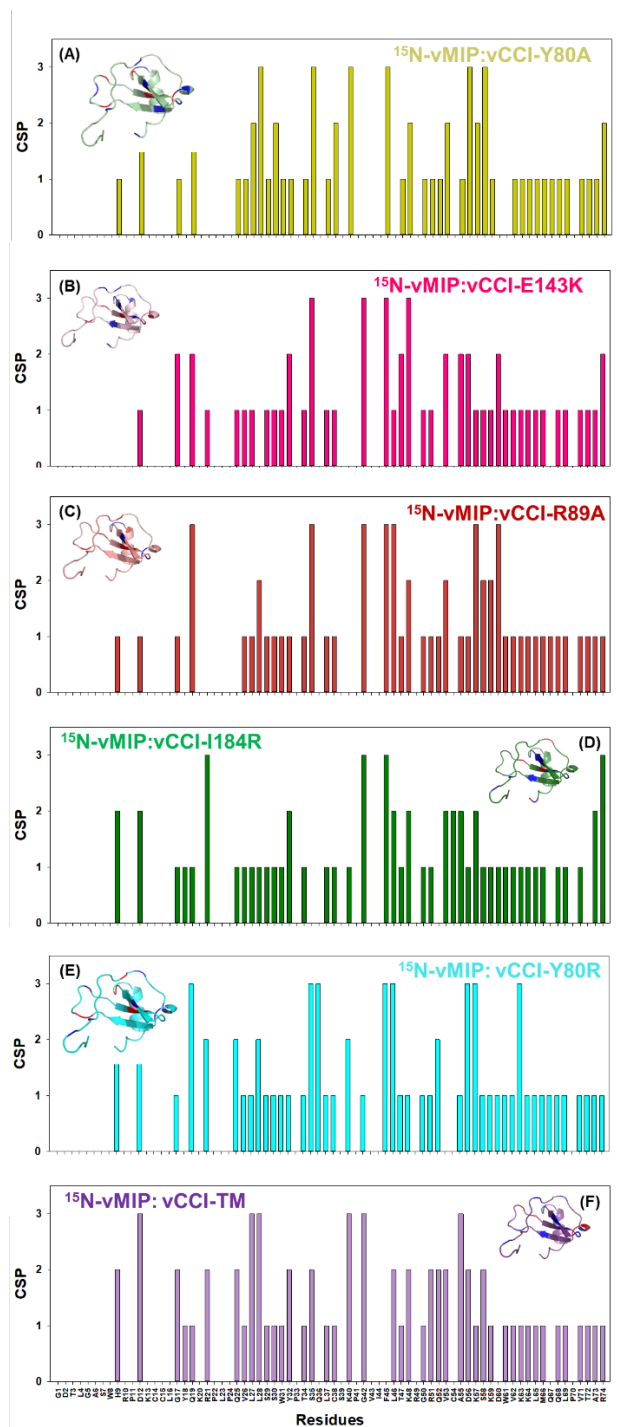
Figure 4.2 Changes in chemical shifts of ^{15}N-vMIP upon binding to vCCI mutants

(A) ^{14}N-vCCI-Y80A, (B) ^{14}N-vCCI-E143K, (C) ^{14}N-vCCI-R89A, (D) ^{14}N-vCCI-I184R, (E) ^{14}N-vCCI-Y80R, (F) vCCI-TM (Triple mutant –Y80R-E143K-I184R). Inset structures of vMIP are highlighted with major perturbed regions upon binding to differential vCCI-variants. Blue and red color indicate the residues that falls in categories 2 and 3 respectively. All the structures were generated using PyMol 1.4.1 software.
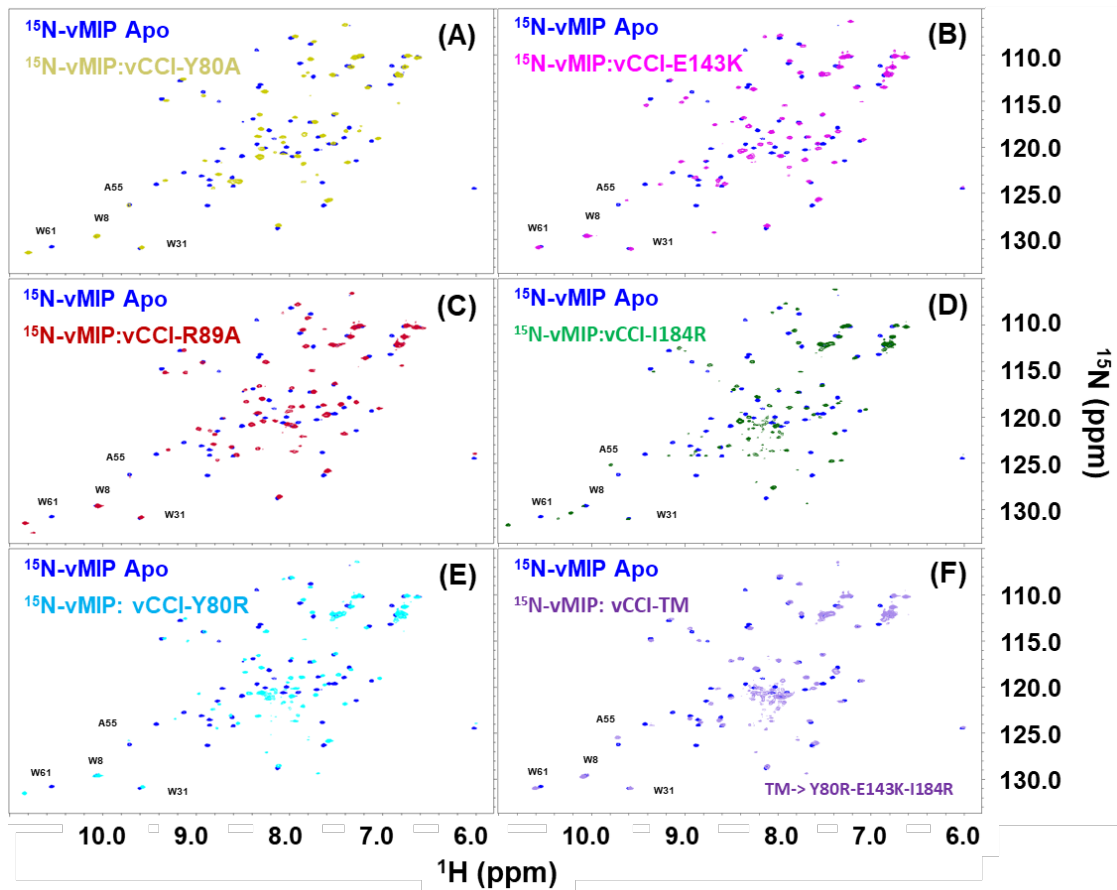
Figure 4.3 Overlay of ^{1}H-^{15}N HSQC spectra of free15N-vMIP (blue) and ^{15}N-vMIP in complex with vCCI mutants

(A) ^{14}N-vCCI-Y80A (light green), (B) ^{14}N-vCCI-E143K (pink), (C) ^{14}N-vCCI-R89A (red), (D) ^{14}N-vCCI-I184R (green), (E) ^{14}N-vCCI-Y80R (cyan), (F) ^{14}N-vCCI-TM (triple mutant- Y80R-E143K-I184R) (purple) with a ratio of 1:3.

Figure 4.4 displays the overlay of actual chemical shift perturbation values obtained for the complexes, where most of the highly perturbed residues in vMIP-II belong to the N-loop region and the 2nd β-strand region. A few residues that belong to 50's region have also been observed to show substantial chemical shift changes. Of all the vCCI mutants, vCCI Y80R showed the highest magnitude of peak movement, which implies a strong interaction with ^{15}N-vMIP-II. However, differential chemical shift changes in residues that belong to the N-loop region, the 2nd β -strand region and 50's region were observed for distinct ^{15}N- vCCI mutant:vMIP-II complexes.
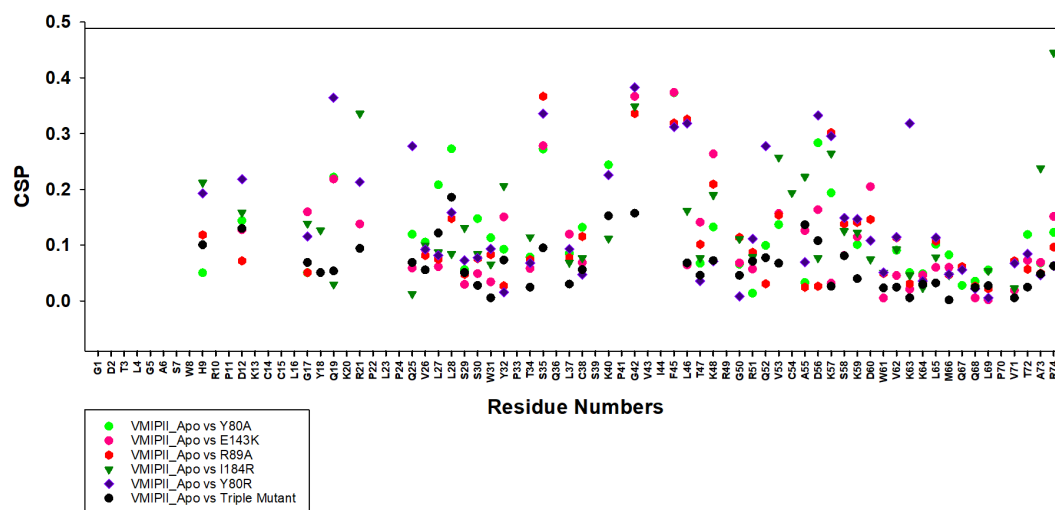
Figure 4.4 Overlay of all the chemical shift perturbation (CSPs) values of vMIP-II with vCCI mutants

Overlay of all the chemical shift perturbation (CSPs) values obtained for ^{15}N-vMIP upon forming the complex with **(A)** ^{14}N-vCCI-Y80A (light green), **(B)** ^{14}N-vCCI-E143K (pink), **(C)** ^{14}N-vCCI-R89A (red), **(D)** ^{14}N-vCCI-I184R (dark green), **(E)** ^{14}N-vCCI-Y80R (purple), **(F)** ^{14}N-vCCI-TM (triple mutant- Y80R-E143K-I184R) (black).

Table 4.1 Annotations of chemical shift perturbation categories

Chemical Shift perturbation	Annotation
0	Peaks not observed
1	Chemical; shift values less than or equal to average
2	More than average but less than one standard deviation away from average
3	More than one standard deviation from average

Table 4.2 Summary of residues falling in chemical shift perturbation categories 2 and 3 for each ^{15}N-vMIP-^{14}N-VCCI variant complex

CSP Categories	^{15}N-vMIP:vCCI-Y80A	^{15}N-vMIP:vCCI-E143K	^{15}N-vMIP:vCCI-R89A	^{15}N-vMIP:vCCI-I184R	^{15}N-vMIP: vCCI-Y80R	15N-vMIP: vCCI-TM
3	L28, S35, K40, F45, D56, S58	S35, G42, F45, K48	Q19,S35, G42, F45, L46, K57, D60	R21,G42, F45,R74	Q19, S35, Q36, F45, L46, D56, K57, K63	D12,L27, L28, K40, G42, A55
2	D12, Q19, L27, S30, C38,K48, V53, K57,R74	G17, Q19,Y32, T47, V53, A55, D56, D60, R74	L28, K48, V53, S58, K59	H9,D12, Y32,L46, K48, V53, C54, A55,K57, A73	H9, D12, R21, Q25, L28, K40, Q52	H9, G17, R21,Q25, Y32,S35, L46, K48, R51, Q52, V53, D56, S58
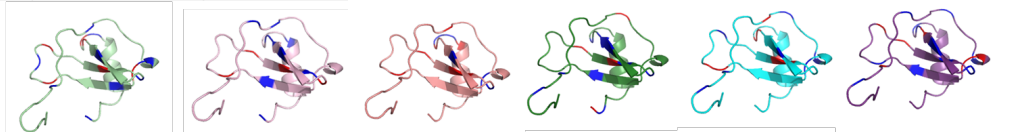
Table 4.1 and 4.2 summarize the most highly perturbed residues for the different complexes. Such residues have also been mapped on the structure of vMIP-II (Inset, Figure 4.3). We have observed a few common residues including S35, F45, G42, that showed highest perturbation in more than 3 complexes. Such residues are predicted to be involved in indirect interactions between vMIP-II and vCCI variants, owing to their specific positions in the vCCI mutant:vMIP-II complexes. Further, the triple mutant of vCCI with the combination of three mutations including Y80R, E143K, and I184R, showed the least movement of peaks upon binding vMIP-II, which indicates its low binding affinity (Figure 4.4). This triple mutant, comprised of three mutations, is involved in disrupting the three major interactions between the vCCI and vMIP-II. Additionally, the vCCI variant with mutation of its acidic residue (E143) to basic residue lysine (K), also appears to show less interaction with vMIP-II as evidenced by small chemical shift changes upon binding, in contrast to other vCCI variants. This is due to the disruption of an important electrostatic interaction between E143 of vCCI and R21 of vMIP-II. Moreover, mutation of E143 to Lysine (K) may lead to repulsion between vCCI and vMIP-II, due to the presence of more positively charged residues (K20 and R21 of vMIP) in the vicinity of K143 of vCCI E143K variant (Figure 4.5). The vCCI Y80R mutant, in which the tyrosine has been replaced with arginine, potentially blocks another interaction between the Y80 of vCCI and R21 of vMIP-II (Figure 4.5). Hence, the replacement of tyrosine 80 with arginine, not only disrupts an important interaction between vCCI and vMIP, it also leads to possible repulsion between the two proteins. Finally, the vCCI I184R variant, in which isoleucine 184 has been replaced with arginine, was designed to remove hydrophobic interactions with vMIP-II, and appears to show overall fewer large interactions than the other point mutants.

Fluorescence anisotropy shows tight binding for vCCI variants. Fluorescence anisotropy is an excellent technique for measuring binding of vCCI to chemokines, since a fluorophore on a chemokine will show higher anisotropy upon binding to the much-larger vCCI, and this technique can be used at nanomolar (or sub-nanomolar) concentrations[116]. Given the excellent solution properties of the chemokine analog vMIP-II, we used this protein as the vCCI binding partner, enzymatically placing fluorescein on its C-terminus: the C-terminus was engineered to contain the amino acids LPXTG, allowing the sortase enzyme from Staphylococcus aureus[265,266] to efficiently covalently join this to the N-terminus of a peptide, replacing the Gly with the peptide sequence. In our case, we

produced "vMIP-II LPMTG-CHis" and used the sortase enzyme with the peptide GGGK-Fluorescein, to make "vMIP-II LPMTGGGK-Fluor". We refer to this as "vMIP-fluor". Purification of the sortase product was carried out with reversed phase chromatography, and the product verified by mass spectrometry. It should be noted that anisotropy changes measured upon binding rely on a loss of motion of the fluorophore as the molecular weight of the complex increases. Given the extra amino acids placed on the C-terminus of vMIP-II, it was possible that the fluorophore would be able to retain high levels of motion regardless of the binding state of the chemokine, leading to a low anisotropy signal. Indeed, several chemokines having sortase-added fluorophore showed significantly less anisotropy change upon vCCI binding than vMIP-II, including RANTES and Eotaxin, which is why the present experiments were primarily carried out with vMIP-fluor which retained a robust change in fluorescence anisotropy upon binding to the vCCI variants.
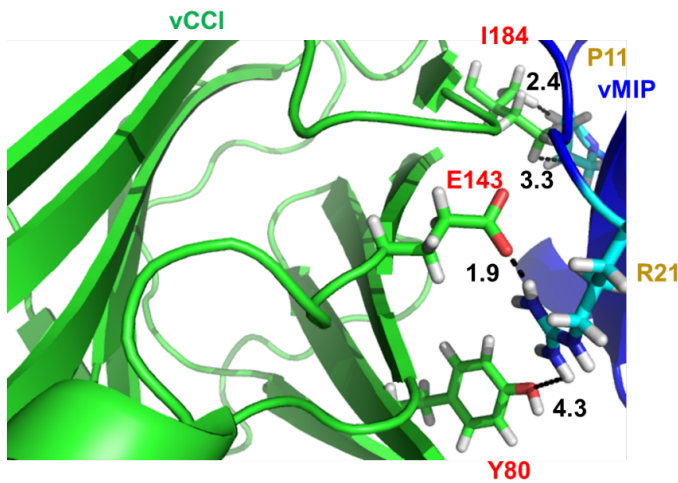
Figure 4.5 Depicting differential interactions between vMIP-II and vCCI

Depicting differential interactions between I184, E143K and Y80 (marked in red) residues of vCCI and P11 and R21 (marked yellow) of vMIP.
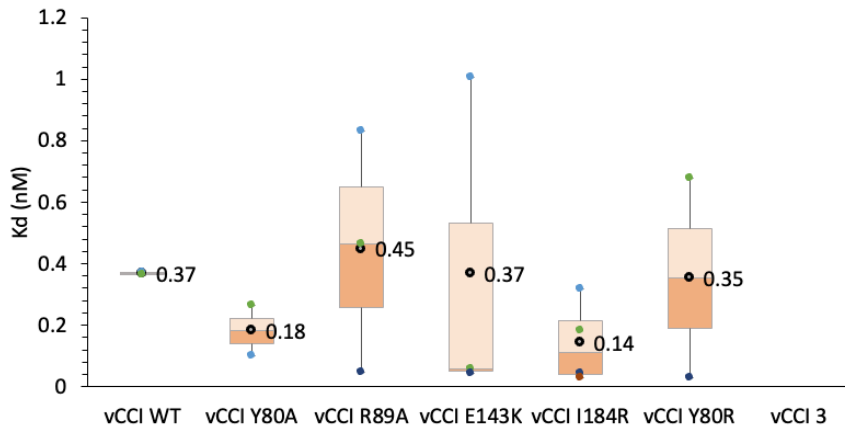
Figure 4.6 The Kd (nM) of vCCI WT and its variant from fluorescence anisotropy assay
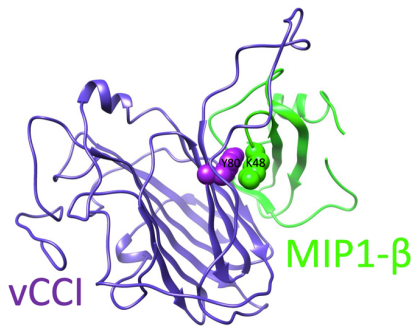
Figure 4.7 vCCI Y80 residue (pink) is close to the side chain of MIP1-β K48
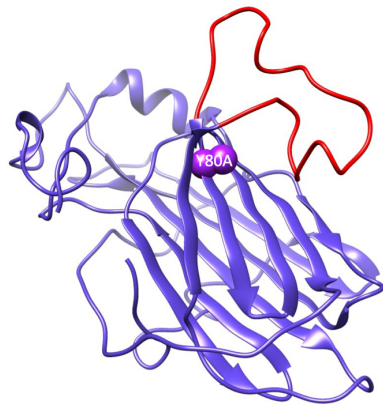
Figure 4.8 vCCI Y80A structure

Wild type vCCI binding to vMIP-fluor. We have previously used competition experiments to measure the wild type vCCI interaction with vMIP-II, resulting in a measured Kd of 0.06 nM[261]. Here, we use direct binding of vCCI with vMIP-II and obtain a Kd of 0.37 ± 0.01nM (Figure 4.6, Supplementary Figure 4.2). The measurements were carried out at various concentrations, although the tight binding led to unreliable curves (resembling a step function) when concentrations of the fluorophore were significantly above the Kd. However, at lower concentrations, there was insufficient sensitivity to carry out the binding experiment below 0.25nM of vMIP-fluor, leading us to conclude that 0.37nM is likely an upper limit to the Kd as determined by this method.

vCCI Y80A binding to vMIP-fluor. The Y80A mutation of vCCI is of great interest due to seeming conflict between its predicted function and experimental results. The structure of rabbitpox vCCI with a soluble variant of the chemokine MIP-1b showed that Y80 was in close contact and possibly obstructing the 48 position of the chemokine[260] (Figure 4.7).

The implication was that if this large residue were mutated into a smaller amino acid such as alanine, the chemokine binding might be tighter. However, when the Y80A mutation was made by White et al. in the similar vCCI gene from variola (and expressed with an Fc tag), the authors found little ability to inhibit the function of the chemokine RANTES (suggesting low/no binding by vCCI Y80A), and concluded that the Y80A mutation unexpectedly disrupted its ability to bind chemokines[262].

We carried out molecular dynamics simulations of vCCI Y80A to better understand its molecular motions and possible binding interactions. In contrast to the functional assay by White et al, fluorescence anisotropy of vCCI Y80A binding to vMIP-fluor shows a tight Kd of 0.18 ± 0.12 nM (Figure 4.6, Table 4.3, Supplementary Figure 4.2). This also appears to be in conflict with our own MD studies that repeatedly indicate that the Y80A mutant's flexible loop closes over the active site, impeding chemokine binding (Figure 4.8).

However, it should be noted that fluorescence anisotropy studies are an equilibrium technique, with measurements occurring on the timescale of minutes, while MD simulations show possible motions on a timescale of microseconds or faster. Therefore, while this does not explain the loss of activity obtained by White et al. by this variant, our own results are not necessarily contradictory: It is possible that on a short timescale, the Y80A mutation does allow the loop to close over the binding site, but this may be transient so that the chemokine can bind when the loop moves back and no longer blocks the site. Once the chemokine binds, there is no indication that the Y80A mutation would disrupt binding (and indeed as noted the structure indicates that the smaller alanine in the 80th position may be favorable to binding) and the loop should behave normally to also assist binding by the chemokine. Therefore, the overall Kd of binding of the chemokine by vCCI Y80A is apparently largely unaffected by the transient effect of this mutation on the vCCI loop.

vCCI mutations predicted to lead to lower affinity at Y80, E143, and I184. Accordingly, vCCI variants with a mutation at each position, and at all three simultaneously, were produced. For Y80 and E143, replacement was with a positively charged residue with the hypothesis that a large, basic amino acid would interact poorly with the basic surface of the chemokine binding partner, so the vCCI variants Y80R and E143K were produced. At position 184, it was hypothesized that adding a charge to the site that interacts with the critical hydrophobic residue of the chemokine would similarly disrupt binding, so I184R was produced. The triple mutant Y80R/E143K/I184R contains all three mutations.

Fluorescence anisotropy of each single mutant showed markedly different results depending on which concentration and which type of instrument was used. In each case, at low concentrations in a fluorimeter with a 2mL quartz cuvette, clear and fairly tight binding was observed: Y80R 0.37nM; E143K 0.37nM; I184R 0.14nM (Figure 4.6, Table 4.2, Supplementary Figure 4.2). However, using the same instrument, higher concentrations gave higher Kd values. Further, when the experiments were carried out in a 96 well plate reader (at much higher concentrations due to lower sensitivity of this instrument), the apparent Kd depended upon the time of reading (1-6hr) and ranged from 21-97nM for Y80R mutant; 18-97nM for E143K mutant, and 4-49nM for I184R mutant (Supplementary Figure 4.2). This suggests that these point mutants may have multiple equilibria, including possible aggregation, so further experiments were carried out using Biolayer interferometry (BLI, below). Overall, however, while each individual variant shows fairly tight binding to vMIP-fluor using anisotropy, the triple mutant Y80R/E143K/I184R shows no binding up to 100 nM, which is not unexpected given the apparent low binding shown even at micromolar concentrations by NMR (Figure 4.3 for NMR and Table 4.1).

The R89A variant tightly binds vMIP-fluor. The arginine at position 89 in vCCI appears to contact. Therefore, it was hypothesized that mutating this residue to the smaller

and uncharged alanine would lead to better binding to chemokines. As expected, this mutation showed tight binding to vMIP-fluor, with a Kd of 0.45 ±0.39 nM (Figure 4.6, Table 4.2, Supplementary Figure 4.2). In addition, unlike several other point mutants, this variant did not show a tendency to aggregate, as noted by stable anisotropy readings at a wide range of concentrations and no sign of anomalous peaks in HSQC spectra (data not shown).

4.5 Discussion

Chemokines play a critical role in inflammatory processes, and are therefore implicated in many diseases, including arthritis, asthma, and traumatic brain injury [12]. Chemokine binding proteins have great potential as potential therapeutics, particularly if their binding can be well enough understood to eventually target subsets of chemokines. These proteins are generally derived from viruses (that use CBP's to subvert the immune system), and by arthropods such as ticks[255,267]. While there are a variety of types of CBP's with an increasing amount of structural information known[255], the vCCI proteins from poxviruses (sometimes called 35K or p35) are studied here because of their high affinity binding to the CC subfamily of chemokines, which includes chemokines directly relevant to the inflammatory diseases mentioned. These proteins have high sequence identity and have been shown to be amenable to production from E. coli[261], baculovirus[87] and mammalian cell systems[262].

The binding face of vCCI was predicted in the original X-ray structure of cowpox vCCI provided by Carfi et al[88], and was confirmed by the NMR structure of rabbitpox vCCI in complex with a variant of CCL4[260], and several other structures of vCCI-like proteins have been reported[87,93]. However, while these structures suggested areas of contact between the binding protein and the chemokine, it is not clear from a structure alone which interactions are critical for binding. Mutations on the CC chemokine ligand showed the importance of several basic residues (at position 18, 24, 44, 45 using CCL4 numbering), although even tightly binding CC chemokines do not necessarily have a positive charge at each position[116,119,120].

Several variants of vCCI proteins have been reported. Using the vCCI-like protein EVM1 (encoded by the ectromelia virus, causative agent for mousepox), several mutations were shown to decrease binding to CCL3, particularly the I173R mutation (equivalent to I184R in rabbitpox vCCI) which caused a 448-fold higher Kd. These authors also showed a large decrease in the ability of EVM1/vCCI to bind CCL3 when the negatively charged loop was completely removed and when the tyrosine at position 69 was replaced by arginine (equivalent to Y80R in rabbitpox vCCI)[87]. Several variants of vaccinia virus (used in smallpox vaccinations) vCCI were also reported, each fused to an Fc domain for longer bioavailability in in vivo studies. In this work, variants were tested for their ability to inhibit the function of chemokines in activating their receptor and in mediating chemotaxis in vitro, as well as to blockade monocyte recruitment in mice. It was found that switching the charge at E143 caused a loss of vCCI's ability to inhibit CCL5 and CCL2 function, suggesting that this site is important to the ability of vCCI to bind these chemokines[262]. Conversely, replacing the bulky arginine at position 89 of vCCI caused an apparently enhancement of the ability of the protein to inhibit chemokine function.

Finally, as previously noted the tyrosine at position 80 was particularly interesting, as White et al found that their Y80A variant of vCCI unexpectedly showed no ability to

inhibit CCL5 function. It had been expected that this mutant would have less steric hindrance upon binding the chemokine and so inhibit chemokines very well[262].

Our results show some similarity to these results with related vCCI proteins, and also some differences. In general, we observe higher affinity for point mutants than other studies, with no single point mutant leading to more than a 20 fold loss of binding, confirming that vCCI's ability to bind is quite robust, with single changes not being particularly disruptive. There are some caveats to this however, including that we work with rabbitpox vCCI, whereas others have reported work with similar (but not identical) vCCI's from other poxviruses. Perhaps more important, our current results have been obtained using vMIP-II, a virally expressed protein, as a canonical chemokine. This protein has been shown to bind more tightly to rabbitpox vCCI than other chemokines tested[261] so its many productive binding interactions may give it more resilience to changes in vCCI.

An important goal for research into chemokine binding proteins is the eventual ability to engineer them as anti-inflammatory therapeutics. vCCI has great potential in this regard, but the ability of the wild type protein to bind essentially all CC chemokines could be considered limiting, particularly in situations where one (or a few) chemokines might be implicated in inflammation, and there is no need to inhibit others (some of which may be desirable to remain active). In this work we identify particular vCCI residues that likely contact the chemokine, and show that changes in these locations still lead to a folded, active protein. MD studies indicate which regions of vMIP-II likely interact with each of these vCCI points of contact, allowing future studies of particular chemokines that have (or don't have) likely productive interactions at those sites. Such work could include engineered vCCI that interacts most tightly with eotaxin (to possibly inhibit an asthma response [268]) or CCL2/MCP-1 (involved in traumatic brain injury[269]. We are currently working on understanding the vCCI interaction with CCL17, one of the few CC chemokines that does not bind vCCI tightly, but which is involved in macrophage related inflammatory disease[270,271] and so may be an appropriate future target for an engineered vCCI ([255]and manuscript in preparation).

In conclusion, we have used a combination of biophysical techniques and molecular dynamics to probe the specific interactions between vCCI and a canonical chemokine, vMIP-II. We show specific points of contact between the two proteins that are likely important to binding and that point the way toward making vCCI retain affinity, yet have more specificity for particular chemokines.

Chapter 5

Rational Design of Higher Affinity Interaction Between CC Chemokine Binding Protein vCCI and CCL17/TARC

5.1 Abstract

The poxvirus-derived protein vCCI (viral CC chemokine inhibitor) binds almost all members of the CC chemokine family with high affinity (in the nanomolar range), inhibiting their biological interactions and thereby eliminating their pro-inflammatory actions. However, vCCI binds at only micromolar levels with the CC chemokine CCL17, despite this protein having the canonical chemokine fold. The development of an understanding of the binding of vCCI in terms of both affinity and specificity is important so that this protein can potentially be developed as an anti-inflammatory therapeutic. Therefore, an analysis of the molecular dynamics simulation of a model of the vCCI:CCL17 complex was undertaken, along with a sequence comparison of CCL17 with other chemokines. Several sites of interest in CCL17 were judged to be important to binding vCCI such that their mutation to a more suitable amino acid was hypothesized to improve binding to vCCI. These sites in CCL17 were mutated and the proteins expressed and purified. It was found that single point mutants V44K and Q45R modestly increased binding affinity to vCCI, and their combination into a double mutant provided further improved affinity. Highest affinity was achieved with the triple mutant CCL17 G17R/V44K/Q45R, which gave a Kd of 0.25 ± 0.13 µM for the vCCI:CCL17 variant complex, a 68 fold improvement in affinity compared to the complex with wild type CCL17. A final quadruple mutant CCL17 G17R/V44K/Q45R/R57W showed high affinity (0.59 ± 0.09 µM) compared to wild type, but lower affinity than the triple mutant. This work demonstrates that sequence comparisons and molecular simulations can predict chemokine mutations that increase binding to vCCI, an important first step in developing engineered chemokine inhibitors useful for anti-inflammatory therapy.

5.2 Introduction

One of the most effective inhibitors of chemokines is the poxviral protein vCCI (also called 35K). This protein tightly binds and inhibits many members of the CC chemokine subfamily, which are involved in inflammation and are so named because they have a conserved pair of cysteines near their N-terminus. As such, vCCI has been suggested as an anti-inflammatory protein that may be useful for use against a wide variety of immune-related pathologies, including asthma, traumatic brain injury, and arthritis [12,272,273].

All chemokines share the same general fold, and CC chemokines have a high degree of sequence similarity. For instance, chemokine CCL17 (also called TARC) is a small protein that binds the receptor CCR4 on the surface of some immune cells, causing activation and chemotaxis. CCL17 shares 28% identity and 57% similarity to CCL2, and 35% identity and 61% similarity to CCL11, which both tightly bind vCCI. Despite these similarities, vCCI was reported to have limited binding affinity for CCL17[157]. We confirmed this in a recent study, showing a vCCI:CCL17 binding Kd of 14 µM[54]. This is several orders of magnitude weaker than vCCI binding to similar CC chemokines such as CCL2, CCL4,

and CCL11, which bind vCCI at low nanomolar (nM) or even sub-nM levels[158,274,275]. In this work we use a combination of molecular dynamics simulations and sequence comparisons to engineer CCL17 mutants with improved binding to vCCI, and succeed in improving the binding of CCL17 by 68-fold. This significant gain of affinity demonstrates the promise of combined computational and experimental biochemistry to determine the key amino acids mediating protein interactions.

The vCCI-chemokine system provides an ideal test for engineering protein binding, because the chemokines all share the same fold, while exhibiting a range of affinities for vCCI. Hence, it should be possible to indentify the pairwise interprotein contacts that strengthen or weaken binding, and mutate amino acids on either the chemokine or vCCI to modulate the binding affinity. Additionally, there is an experimentally determined structure of the vCCI:CCL4 complex[276] which can be used as a template for molecular dynamics simulations of vCCI binding to other chemokines [277–279]. This work is conceived as a proof-of-concept study toward eventually redesigning vCCI itself in a complementary fashion to obtain affinity and specificity toward CCL17 or other CC chemokines. Mutant vCCIs that are specific for certain sets of chemokines could be useful therapeutically, allowing for precise inhibition of those particular chemokines that cause damage while allowing protective inflammatory chemokine signaling to persist.

5.3 Materials and Methods

5.3.1 Protein expression and purification

The gene for CCL17 containing an N-terminal thioredoxin tag followed by an enterokinase (EK) cleavage site along with a C-terminal LPMTGHHHHHH (to allow the sortase reaction) was purchased from Twist Bioscience (San Francisco, CA). We then mutated CCL17 into 3 single mutants: V44K, Q45R, and G17R using PCR with primers purchased from Integrated DNA Technologies (Coralville, IA); and 3 double mutants: V44K/Q45R, G17R/V44K, G17R/Q45R made by PCR using a single mutant as a template and using primers purchased from Integrated DNA Technologies. The genes for the triple mutant G17R/V44K/Q45R and for the tetra mutant G17R/V44K/Q45R/R57W were purchased from Twist Bioscience. Each of these was placed in a pET-28a (+) expression vector, and was purified using the protocol described in our previous paper [54]. One single mutant (CCL17 G17R), and 2 double mutants (G17R/V44K and G17R/Q45R), were found to not express well and were not further considered.

In brief, the gene was expressed in E. coli BL21(DE3), and the cells were lysed in 6M guanidinium chloride, and the protein was semi-purified over a home-packed Ni-NTA affinity column (Qiagen, Hilden, Germany) followed by refolding the semi-purified protein and then dialysis. The fusion protein was then cleaved by EK, and CCL17 was further purified by a C4 reversed phase chromatography column (Vydac, Hesperia, CA, USA) using an acetonitrile gradient. The target protein was verified by SDS-PAGE and lyophilized.

Purification of vMIP-II-LPMTG-CHis and vCCI, were carried out as reported previously [54]. Labeling vMIP-II-LPMTG-CHis with fluorophore 5FAM was carried out through a reaction with the enzyme sortase A. This enzyme was produced in-lab as described previously [54]. The reaction was carried out in the dark using the peptide GGGK-5FAM purchased from Bon Opus Biosciences (Millburn, NJ), as described previously [54]. Briefly, a solution containing 50 µM vMIP-II-LPMTG-CHis, 5 µM sortase A, 10 mM CaCl2,

and 150 µM GGGK-5FAM were incubated in the dark at 4°C for 2 days followed by incubating in ambient temperature for 17 hours. The target protein vMIP-II-LPMTGGGK5FAM (vMIP-fluor) was then purified over an analytical C4 reversed phase column (Vydac) and verified by SDS-PAGE and mass spectrometry. The protein vMIP-fluor was then aliquoted, lyophilized, and stored in the dark at -20 °C.

5.3.2 Fluorescence Anisotropy Assay

The competition fluorescence anisotropy assay was performed as reported previously [54]. Briefly, the 1:1 complex of vCCI and vMIP-fluor at 8 nM was aliquoted into each cuvette and kept in the dark. Different concentrations of unlabeled CCL17 and its mutants were titrated into pre-incubated vCCI-vMIP-fluor cuvettes with observation of the competition displacement of vMIP-fluor as a function of concentration at equilibrium via the observed change in anisotropy. The data were then normalized fit to a system of equations describing the conservation of species concentrations and both equilibria to yield the Kd for the CCL17 and its mutants with vCCI interaction using Scientist software (Micromath, St. Louis, MO) [158].

5.3.3 NMR Spectroscopy

NMR experiments were carried out as described previously.[2,3] In brief, CCL17 mutants and vMIP-II-LPMTG-CHis NMR samples were dissolved in 20 mM sodium phosphate buffer with 10% D_2O, 20 µM 2,2-dimethyl-2-silapentane-5-sulfonic acid (DSS), pH 2.5. vCCI samples were dissolved in buffer containing 100 mM sodium chloride, 20 mM sodium phosphate, 10% D_2O, 20 µM DSS, pH 7.0. Some samples were isotopically labeled with ^{15}N, allowing two-dimensional HSQC experiments, while others were not isotopically labeled and were determined to be folded by one dimensional 1H NMR. The NMR spectra were obtained on a Bruker 600- MHz AVANCE III spectrometer equipped with a TCI cryo-probe.

5.3.4 SEC-MALS

SEC-MALS (size exclusion chromatography with multi-angle static light scattering), WYATT Technology (Hollister Ave, Santa Barbara, CA), were applied in this study to evaluate the stoichiometry of CCL17 and vCCI at high concentration (10 mg/mL). The column was first equilibrated with buffer (100 mM sodium chloride, 20 mM sodium phosphate, pH 7.0) overnight to bring down the system noise. Then, samples were concentrated to 10 mg/mL with an Amicon concentration system and filtered with a 0.22 µm filter before injecting onto the SEC-MALS instrument.

5.3.5 Molecular Dynamics methods

All-atom molecular dynamics simulations (MD) were performed on two vCCI:CCL17 complexes, one with wild type CCL17 and the other with the CCL17 triple mutant (G17R/V44K/Q45R). Both of these structures were derived from the experimental NMR structure of the vCCI:MIP-1β complex (PDB: 2FFK). The vCCI:CCL17 starting structure was created from the vCCI:MIP-1β structure by computationally superimposing the experimental CCL17 wild type structure onto the MIP-1β chain and minimizing the root-mean-square distances between the corresponding Cα backbone atoms. The vCCI:CCL17 triple mutant was created by manually modifying the three amino acids to their mutant form. The net charge on the complexes was neutralized and adjusted to an ion concentration of approximately 70 mM by adding Na^+ and Cl^- ions. We first ran a series

of short minimization and equilibration runs, followed by a full 1 microsecond MD "production" simulation. All MD simulations were performed using Gromacs 2016.3 [280] using the NPT ensemble, the Verlet cutoff scheme and a 2 fs timestep. All bonds to hydrogen were constrained to their equilibrium length using the LINCS algorithm [281]. Temperature was maintained at 300K using the Bussi et al. thermostat [282] and pressure at 1 bar using the Parrinello-Rahman barostat [283]. The simulations were performed using the AMBER99SB-ILDN force field for the protein [284] and the TIP3P water model [285]. The analysis of the interprotein contacts was performed using the "Protein interfaces, surfaces and assemblies" service, PDBePISA (https://www.ebi.ac.uk/pdbe/pisa/) hosted at the website of the European Bioinformatics Institute [286]. We wrote a custom Python script using the Selenium package (https://www.selenium.dev/) to automatically upload structures sampled every 2 nanoseconds from the 1 microsecond trajectories.

5.4 Results

We began by performing a sequence alignment of CCL17 with five other chemokines with high affinity for vCCI (Figure 5.1A). This showed that CCL17 differs in several key residues from the other chemokines. Specifically, CCL17: 1) has a glycine instead of a positively charged residue at position 17; 2) lacks a positively charged residue at positions 44 and/or 45 present in most other chemokines; and 3) has an arginine instead of the highly conserved tryptophan at position 57. These positions are marked on the vCCI-bound CCL17 model shown on the right in Figure 5.1B which were suggested by molecular simulations (see below).
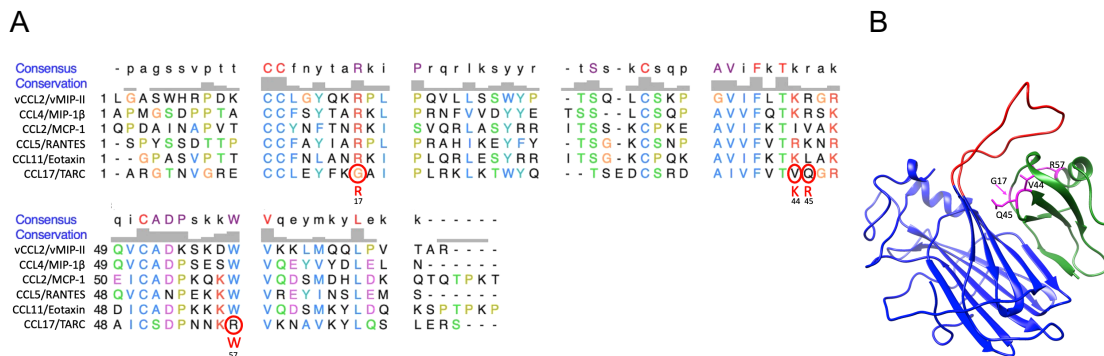
Figure 5.1 CCL17 sequence alignment and the structure of vCCI WT in complex with CCL17

A. Sequence comparison of several CC chemokines that bind vCCI with high affinity, along with CCL17, which binds vCCI several orders of magnitude more weakly. B. Model of the vCCI:CCL17 interaction, as determined by molecular dynamics. vCCI is shown in blue, with the acidic loop denoted in red. CCL17 is shown in green.

The sites at 17, 44 and 45 are in locations that previous experimental structures and molecular simulations have shown can contact vCCI residues. Based on these observations, to create a mutant CCL17 that should have improved binding to vCCI, we identified the following three mutations: G17R, V44K, and Q45R. It is less clear what role the conserved W57 may play in the other chemokines' binding affinity to vCCI. In the experimental vCCI:CCL4 structure the chemokine W57 is not located near the vCCI interface, and, if it were able to contact vCCI, the R57 in CCL17 might be expected to

contribute to stronger binding to vCCI like the other positively charged residues on the chemokines.

vCCI-CCL17 wildtype   vCCI-CCL17 G17R/V44K/Q45R
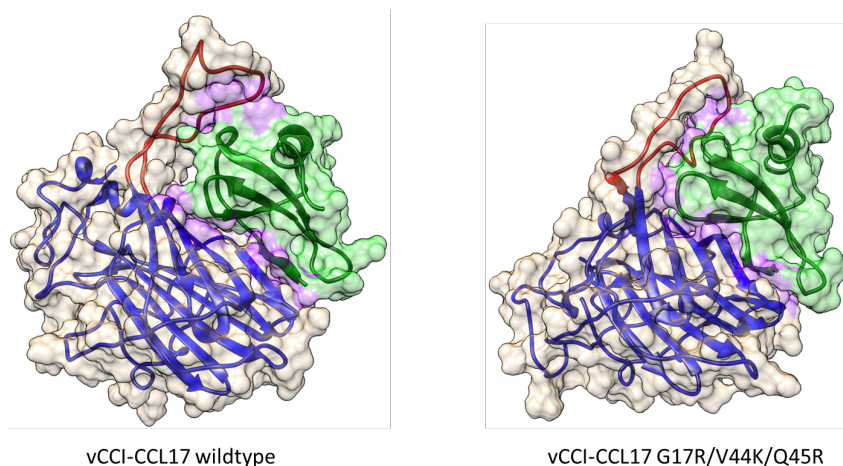
Figure 5.2 vCCI WT in complex with CCL17 WT and triple mutant

Left: vCCI in complex with CCL17 WT. Right: vCCI in complex with CCL17 triple mutant G17R/V44K/Q45R. vCCI is shown in blue, with the acidic loop denoted in red. CCL17 is shown in green. The purple surface shading shows where there are close contacts between the vCCI and chemokine.

After the sequence analysis, we used molecular dynamics (MD) simulations to study the effect of the mutations at sites 17, 44, and 45. We simulated wild type CCL17 bound to vCCI and also the triple mutant G17R/V44K/Q45R for a full 1 microsecond of molecular dynamics. The starting structures were built using as a template the experimentally determined structure of vCCI bound to a human CC chemokine (MIP-1β) [22]. Figure 5.2 (and Supplementary Figure 5.1) shows the bound conformations after 1 microsecond of MD, with vCCI:CCL17(wild type) on the left and vCCI:CCL17(triple mutant) on the right. The Supplementary Figure shows the bound structures "opened" to reveal the binding interface and the purple surface shading shows where there are close contacts between the vCCI and chemokine. The most obvious difference in the interface between the CCL17 wild type and triple mutant is in the contacts with the large vCCI loop (residues 51-74) which has more complete contact with the mutant CCL17 than the wild type. Quantitatively, the interface surface areas calculated using PDBePISA, are 1419.6Å^2 and 1210.9Å^2 for the CCL17 triple mutant and wild type, respectively, suggesting stronger interaction between the CCL17 mutant and the vCCI. PDBePISA also calculates an empirical approximation of the binding ΔG, which yields a binding free energy for the triple mutant 1.1 kcal/mole stronger than for the wild type, which corresponds to a Kd 7-fold smaller for the triple mutant than the wild type.

We analyzed the specific amino acid interactions between the vCCI and chemokines using PDBePISA. This allowed us to count the number of hydrogen bonds (including salt bridges), and also allowed us to identify close inter-protein contacts that are not hydrogen bonds. We analyzed the last 500 ns of the 1 microsecond trajectories, sampling every 20 ns, and only noted interactions that were present in at least 1/3 of the

sampled frames. Figure 5.3 plots these contacts between the amino acids in the vCCI (represented as the top line of dots in each graph) and the chemokine (represented as the bottom line of dots). The red lines show the persistent hydrogen bonds (including salt bridges) and the dashed black lines represent the close contacts that do not involve a hydrogen bond. The numbers above and below the axes indicate the residues involved in each interaction, color coded by the type of interaction (red for hydrogen bond, black for close contact). These results show that each of the CCL17's mutated residues are involved in persistent hydrogen bonds with vCCI. The CCL17 R17 hydrogen bonds to vCCI E143, the CCL17 K44 hydrogen bonds to vCCI D59 (in the vCCI loop), and the CCL17 R45 hydrogen bonds to vCCI E53 (also in the vCCI loop). Therefore, these sites in CCL17 appear to be promising sites to experimentally mutate to improve binding to vCCI. Overall, the triple mutant CCL17 was found to have 23 persistent hydrogen bonds to vCCI and the wild type only had 14, indicating a stronger binding affinity for the mutant.
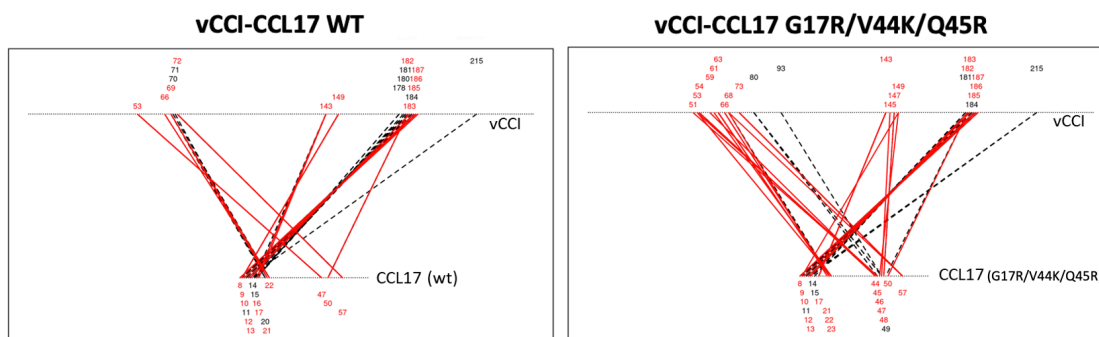
Figure 5.3 The contacts between the amino acids in the vCCI and CCL17.

The red line shows hydrogen bond/salt bridge, and the black dashed line shows the interface contacts.

This simulation also sheds light on the possible effect of the CCL17 R57W mutation on binding. In the simulation of the triple mutant CCL17, the R57 is able to form hydrogen bonds to vCCI intermittently during the 1μs simulation. For example, Supplementary Figure 5.2 shows the R57 in the CCL17 triple mutant forming a hydrogen bond with D73 in the vCCI at the 800 ns point in the simulation. Additionally, the contact maps shown in Figure 5.3 show that R57 in both the wild type and mutant CCL17 has persistent hydrogen bonds with acidic residues in vCCI. If the CCL17 R57 were replaced by a tryptophan, we would expect the interactions with the vCCI acidic residues to be weakened. Therefore, the molecular modeling predicts that the CCL17 R57W mutation will not increase binding to vCCI, despite the tryptophan being highly conserved at that location in tight-binding chemokines.

We experimentally tested the effects of the G17R, V44K, Q45R, and R57W mutations by synthesizing and assaying the mutations individually, in pairs, and as a triple (G17R/V44K/Q45R) and quadruple (G17R/V44K/Q45R/R57W) mutant. The gene sequence for each CCL17 variant was made by PCR or ordered from a commercial source, and these mutants were expressed in BL21(DE3), solubilized in 6 M guanidinium chloride followed by Ni^{+2} affinity chromatography, then refolded, and finally purified by reversed-phase chromatography. The mutants were verified to be folded by NMR. Similarly, wild

type vCCI from rabbitpox was expressed in BL21(DE3), refolded and purified with ion exchange chromatography as previously described [55].
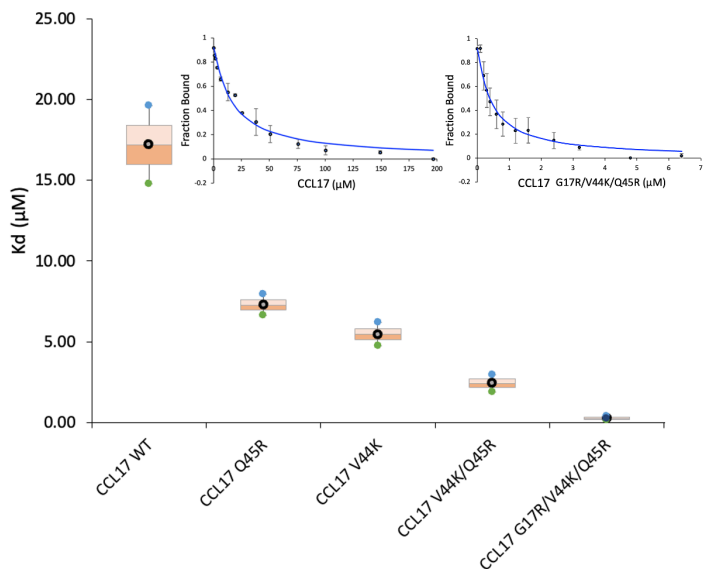
Figure 5.4 Improved vCCI binding for CCL17 variants

Main chart: Mutating various residues in CCL17 leads to improved binding to vCCI. Insets: Fluorescence anisotropy of CCL17 (left) or triple mutant CCL17 G17R/V44K/Q45R (right) in competition with a pre-formed complex of vCCI:vMIP-II-fluor.

To ascertain the vCCI:CCL17 complex stoichiometry, Size Exclusion Chromatography with Multiangle Light Scattering (SEC/MALS) was carried out to demonstrate that vCCI:CCL17 does indeed form a 1:1 complex at high concentrations (10 mg/mL) as observed for other chemokines [22]. To determine the affinity for each CCL17 variant for vCCI, competition fluorescence anisotropy was used. In this technique, a 1:1 complex of vCCI with tight binding ligand vMIP-II having a fluorophore (vMIP-fluor) was first formed and anisotropy measured. Then a CCL17 variant was added to the complex in increasing concentrations and equilibrated. As the CCL17 mutant binds to vCCI, displacing the vMIP-fluor, the anisotropy signal of the vMIP-fluor decreases because an increasing amount of it is in the unbound, i.e. low-anisotropy, form. Using the known Kd (0.06 nM) for vCCI:vMIP-II [55], the curve of anisotropy versus concentration of CCL17 can be fit to obtain a Kd for the CCL17 variant [54].

As shown in Figure 5.4, the designed changes in CCL17 do indeed increase affinity for vCCI. Single mutations show a decrease in Kd of 2-3 fold relative to the wild type CCL17 (Kd of 17.0 ± 3.4 μM): CCL17 Q45R has a Kd of 7.3 ± 0.9 μM, and similar variant CCL17 V44K has a Kd of 5.5 ± 1.0 μM. The effect is more pronounced for the double mutant CCL17 V44K/Q45R, which has a Kd of 2.4 ± 0.8 μM. Further, when multiple areas of contact are mutated in CCL17 to provide a strong ionic interaction with vCCI, significant improvement is observed, with triple mutant CCL17 G17R/V44K/Q45R showing a Kd of 0.25 ± 0.13 μM, a 68-fold increase in affinity compared to wild type CCL17 binding to vCCI (Figure 5.4).

In addition to this triple mutant (G17R/V44K/Q45R) which we accurately predicted would increase CCL17 binding to vCCI, we also created a quadruple mutant (G17R/V44K/Q45R/R57W) to include the highly conserved tryptophan. This change was not predicted by structural modeling to enhance affinity, and indeed, the quadruple mutant does not improve the binding to vCCI beyond that of the triple mutant, giving a Kd of 0.59 ± 0.09 µM.

To put these results in the context of earlier vCCI:chemokine mutation studies by us and others, more than 20 years ago alanine scanning mutagenesis was applied to the chemokine CCL2 to determine which residues were important to binding vCCI. These determined that most single point mutations were either neutral or reduced binding to vCCI, with the exception of K49A which increased binding to vCCI by 2-3-fold [274,275]. Our earlier work expanded on this, using multiple chemokines, further demonstrating the key role of positively charged chemokine residues in vCCI binding. For example, in a study of CCL11 we showed that the replacement of positively charged R and K residues with A typically led to a weaker binding with binding constants up to 4.8 times, 18 times, or 134 times larger for single, double, or triple mutants respectively.4 Replacement of a single basic residue, R, by an acidic residue, E, in CCL11 led to a more dramatic 34-fold increase in the binding constant. Only one CCL11 mutation, K47A, led to improved binding, with an 8-fold decrease in Kd, similar to the earlier CCL2 K49A result mentioned above. These and other mutation studies were important in identifying specific residues required for tight binding of chemokines to vCCI, but did not lead to mutant chemokines for which significantly increased binding was measured, which was the goal of the present study.

The vCCI:chemokine interaction is important both for the impressive ability of vCCI to tightly bind many different chemokines, and also because this binding interaction has great therapeutic potential. An important goal of the study of this interaction is to discern the reasons why a very few CC chemokines such as CCL17 do not bind vCCI well. Most mutagenesis studies involve changing amino acids with the hypothesis that the changes will show the importance of these sites by decreasing binding to an important binding partner. However, in the current work, hypotheses were formed about how to improve binding to vCCI through mutagenesis of CCL17. We used a combination of molecular modeling and biochemical methods to design variants of the chemokine CCL17 to increase the number of favorable interactions between the two proteins, resulting in an overall change in the binding constant from 17.0± 3.4 µM to 0.25 ± 0.13 µM, a remarkable 68-fold increase in binding affinity.

This work illustrates how modifications to the chemokines can lead to stronger vCCI:chemokine interaction, but the complementary approach of designing mutant chemokine inhibitors with modified specificity is an essential next step towards developing therapeutics. An important proof-of-concept of this approach was recently published for evasins, a family of chemokine-binding proteins distinct from the vCCIs. Aryal et al. showed that they could mutate evasins to exhibit substantially higher affinity binding to CCL17, while yielding weaker binding to other chemokines [287,288]. Our group is currently working on the design and testing of mutant vCCI tailored for strong binding to specific chemokines.

Chapter 6

Sustained Delivery of Antiviral Protein Griffithsin and Adhesion to A Biological Surface by A Silk Fibroin Scaffold

6.1 Abstract

The protein Griffithsin (Grft) is a lectin that tightly binds to high mannose glycosylation on viral surfaces. This property allows Grft to potently inhibit many viruses, including HIV-1. The major route of HIV infection is through sexual activity, so an important tool for reducing the risk of infection would be a film that could be inserted vaginally or rectally to inhibit transmission of the virus. We have previously shown that silk fibroin can encapsulate, stabilize, and release various antiviral proteins, including Grft. However, for broad utility as a prevention method, it would be useful for an insertable film to adhere to the mucosal surface so that it remains for several days or weeks to provide longer-term protection from infection. We show here that silk fibroin can be formulated with adhesive properties using the nontoxic polymer hydroxypropyl methylcellulose (HPMC) and glycerol, and that the resulting silk scaffold can both adhere to biological surfaces and release Grft over the course of at least one week. This work advances the possible use of silk fibroin as an anti-viral insertable device to prevent infection by sexually transmitted viruses, including HIV-1.

6.2 Introduction

Since the HIV pandemic began, about 84.2 million people have been infected with the HIV virus, 40.1 million people have died of it, 38.4 million people were living with HIV in 2021, with 1.5 million new HIV infections worldwide every year [289]. HIV can be transmitted through sexual activity, blood transfusions, parenteral exposure via needles, prenatally and through breastmilk [290,291]. Most new infections appear in developing countries and in most cases affect women and young girls. In the United States, 68% of new HIV diagnoses in 2020 were among men who have sex with men; people who inject drugs, sex workers, and prisoners are also disproportionally affected by HIV [292,293].

HIV-1 is a member of the lentivirus family and is 100nM in diameter, covered with surface proteins composed of gp120 and gp41 [294]. Gp120 is the outer spike component while gp41 connects to the viral lipidic membrane [294]; these form trimeric glycoproteins on the surface of HIV-1 and are responsible for targeting viral entry into the cell [295]. Gp120 binds to its receptor CD4, mainly expressed on the surface of the CD4 T cells, which causes conformational changes in gp120 to facilitate the exposure of the fusogenic domain of the gp41 to start the viral fusion to the host membrane [296].

Scientists have been working on an HIV vaccine for more than 30 years. Unlike other viruses, such as polio, smallpox, influenza, measles, and COVID, which can be effectively targeted by antibodies and have long-term or even life-long immunity against subsequent infection, the immune system fails to produce an effective antibody response to the infection. HIV infects, disables, and kills the CD4 T cells which are crucial to the intact function of the immune system[297]. After infection, T-lymphocytes and other immune cells can then become latent reservoirs which harbor the virus and may release HIV at any time. Therefore, even though current small molecule drugs can essentially eliminate

the circulating virus, if medication is stopped HIV reservoirs can activate and viremia will rebound. Furthermore, HIV mutates rapidly which lead to the changes in the structure of proteins that would normally be the target of antibodies, allowing HIV to elude the immune system [297]. Most recently, an HIV vaccine has failed in Phase 3 clinical trial announced by a pharmaceutical company, Johnson & Johnson, on January 18, 2023 [298].

After four decades of endeavors, multiple treatments have been approved by the FDA (Food and Drug Administration), including antibodies [299], protease inhibitors [300], nonnucleoside reverse-transcriptase inhibitors [300], integrase inhibitors[300], and combination antiretroviral therapy with three or more drugs treatment regimens (cART) [301]. These prolong a patient's life, but there is still no cure and no vaccine available currently [301]. Therefore, preventing HIV infection in uninfected and/or at-risk populations is vitally important. More than 10 years ago the FDA approved the first PrEP (pre-exposure prophylaxis) drug Truvada, composed of emtricitabine and tenofovir disoproxil fumarate, both of which are nucleotide reverse transcriptase inhibitors (NRTI), to reduce the risk of HIV infection among high-risk populations and who may engage in sexual activity with HIV-infected partners [302]. It has been found that using daily PrEP by at-risk but uninfected people reduces the sexual acquisition of HIV infection by 99% [303]. Daily oral PrEP, however, relies heavily on a person's ability to adhere to an active prescription or proper schedule, which can be problematic in some settings, particularly for women and girls in the developing world [304]. There is also a concern regarding increasing viral drug resistance when the antiretroviral drugs for PrEP are being used as actual treatment for infected people also [305].

As an alternative to a daily pill, microbicides can be useful as a tool to prevent HIV infection. Microbicides are a type of product or substance that could be inserted into the vaginal or rectal tract to safely prevent HIV acquisition through sexual transmission [306]. Microbicides can be applied to deliver an anti-HIV drug (PrEP product) topically to the vaginal or rectal mucosa surface through materials including foams, films, vaginal rings, gels, etc. [307]. The application of such microbicides provides users with a protection that they can control. Therefore, microbicides have been actively studied and developed as a potential tool in the application against sexually transmitted infections of HIV, especially in resource-poor areas where access to other prevention approaches including condoms or oral PrEP may be limited. An ideal microbicide should be biocompatible, nontoxic, cheap, easy to apply, highly potent against HIV, potentially able to mediate sustained release of anti-HIV drug, and not require refrigeration. The silk fibroin based anti-HIV drug delivery system has all of these properties, making it an excellent candidate for microbicide formulation.

Silk fibroin (SF or "silk" used herein) is derived from silkworm (Bombyx mori) cocoons and is a high-molecular-weight natural protein polymer that has been recognized as a material for biomedical applications for centuries. Silk-based sutures were approved by the FDA in 1993 [308,309]. Later, four silk-based biomedical materials have been commerialized, including bioresorbable surgical mesh (SERI Surgical Scaffold®) [310], silk fabric (MICROAIR DermaSilk®) for atopic dermatitis in children [311,312], a silk patch (Tympasil) for acute tympanic membrane perforation treatment [313], and a silk fibroin wound dressing (Sidaiyi) [314]. With superior biocompatibility, controllable biodegradation into noninflammatory byproducts, aqueous processible, compatibility with sterilization, robust mechanical and thermal properties, and sufficient supply, silk has become a popular biomaterial for drug delivery, as a biosensor, and for tissue engineering [315–325]. It has been

shown that silk is able to encapsulate a variety of molecules, including protein HIV inhibitors, antibodies, and small molecules, with multiple modalities, such as 3D porous scaffolds, films, gels, particulates, and microneedle patches, contributing a desired drug delivery system as a microbicide [49,51,326,327].

We have shown the sustained release of HIV inhibitor Griffithsin (Grft) in silk discs in vitro for 1 month and that Grft remains functional for 14 months at 25°C, 37°C, and 50°C [51]. Grft is a lectin derived from red alga that can tightly bind to high mannose glycosylation on viral surfaces. Against HIV, Grft binds the envelope glycoprotein gp120 to inhibit viral infection and is one of the most potent lectin inhibitors of HIV [328–330]. It also exhibited effective inhibition of other enveloped viruses such as SARS (SARS-CoV-1 and 2) [331,332], and Hepatitis C [333], as well human papillomavirus (HPV) [334], Japanese encephalitis virus (JEV) [335] and Hantaan virus (HTNV) [336]. When Grft is encapsulated into silk fibroin, the SF discs showed strong inhibition properties in activated peripheral blood mononuclear cell (PBMC) and human colorectal and cervical tissue explants. In macaques, insertable SF-Grft disks protected both vaginal and rectal tissue from SHIV infection ex vivo without triggering inflammatory cytokine secretion [51,52]. However, the weak adhesion of silk film discs to tissue surfaces may hinder its application in clinical usage.

The objective of this study was to improve the SF discs' adherence to biological tissue while retaining sustained release of the protein drug. Four chemical additives, tannic acid, Tren-Lys-Cam (TLC) (tris(2-aminoethyl)amine-glycyl-2,3-dihydroxy-benzamide; a siderophore analogue), 3,4-dihydroxybenzoic acid (3,4-DHB), and Hydroxypropyl methylcellulose (HPMC), which may improve SF disc's adhesion to the tissue, were formulated into SF discs. It was found that the silk-HPMC disc can adhere to sample tissue, but this was also accompanied by swift disintegration of the film (within 30 minutes). Therefore, various additives were incorporated into the silk films, including polyethylene glycol (PEG), glucose, and glycerol, to slow down the disintegration of the Silk-HPMC disc. The results show that the addition of the glycerol can decrease the disintegration of the Silk-HPMC while retaining adhesion and sustained release of Grft. Finally, in vitro studies showed the Grft release from Silk-HPMC-Glycerol-Grft discs remain active against HIV.

6.3 Materials and Methods

6.3.1 Production of Grft

The protein Griffithsin was prepared as described previously with small modifications [337,338]. Briefly, the gene encoding the protein Grft with an N-terminal His6 tag in a pET15b vector was transformed into E. coli BL21(DE3) cells (Novagen, Madison, WI) and cultured in Luria–Bertani (LB) medium (VWR, Avantor, Radnor, PA). After expression induced by the adding of IPTG (Gold Biotechnology, MO) to 0.5 mM, for 4-6 h at 37°C, cells were harvested by centrifugation at 4200×g. The cell pellet was then resuspended in lysis buffer (6 M guanidinium chloride (VWR), 200 mM NaCl (Thermo Fisher Scientific, Waltham, MA,), 50 mM Tris (Thermo Fisher Scientific) pH 8.0) followed by sonicating (Qsonica, Newtown, CT) for 10 min to disrupt the cells. After centrifugation, the supernatants were collected and purified by a home-packed Ni-NTA affinity column (Qiagen, Hilden, Germany). The protein was eluted with a pH gradient ending at pH 4.0, and was added dropwise with a 10-fold dilution into refolding buffer (550 mM L-arginine hydrochloride, 200 mM NaCl, 50 mM Tris, 1mM EDTA (Thermo Fisher Scientific), pH 8.0) and allowed to refold for 24 h at 4°C while stirring. Then the protein was dialyzed in 4L

buffer A (200mM NaCl, 20mM Tris pH 8.0) at 4°C twice and then 4L buffer B (80mM NaCl, 20mM Tris pH 8.0) at 4°C twice. Finally, folded Grft was further purified on C4 reversed phase chromatography column (Vydac, Hesperia, CA, USA) with an acetonitrile gradient. The fractions containing pure Grft as determined by SDS-PAGE were combined and lyophilized.

6.3.2 Production of HIV-1 pseudovirus

The single-round virus used containing a lentiviral core with the envelope protein of HIV strain PVO.4 on its surface was a kind gift from Dr. Kathryn Fischer [328]. Viral plasmids' env gene from HIV-1 were from the AIDS Research and Reference Reagent Program, Division of AIDS, NIAID, NIH, and details are as follows: PVO, clone 4, strain SVPB11 (referred to as PVO.4), from David Montefiori and Feng Gao [339]. TZM-bl cells were obtained from the NIH AIDS Research and Reference Reagent Program, Division of AIDS, NIAID, NIH from Dr. John C. Kappes, Dr. Xiaoyun Wu and Tranzyme Inc [340–343]. The TZM-bl cells were cultured in DMEM (Gibco, Life Technologies, Carlsbad, CA, USA) containing 10% FBS, 25mM HEPES (Thermo Fisher Scientific), 1.1% GlutaMAX (Gibco), 0.3% Penicillin/streptomycin (Antibiotic-Antimycotic Solution, Cellgro, Lincoln, NE, USA).

6.3.3 Preparation of silk fibroin solution

The SF isolation and solution preparation is the same as described previously [51,326,344]. Briefly, Bombyx mori cocoons were cut into about 1 cm2 pieces and inspected for debris and stains. Clean cocoon pieces were degummed by boiling in 20 mM Na2CO3 (Thermo Fisher Scientific) for 30 min to remove the sericin protein. The fibers were then rinsed thoroughly in deionized water and air-dried for 2 days. The dried fibers were then dissolved in 9.3 M LiBr (Thermo Fisher Scientific) (1 g silk fibroin fibers in 4 mL LiBr solution) for 4 h at 60°C followed by dialyzing against deionized water for 4 days to remove LiBr. The resulting silk solution was centrifuged to remove debris and the solution was sterilized by autoclave. The SF stock solution was determined to be 5.89% (w/v) and was then stored at 4°C until use. The concentration of SF using this procedure tends to range from 4-6% (w/v).

6.3.4 Production of silk-based discs

The SF stock solution (5.89%) was used to prepare all silk-based discs in this study. The Grft powder was dissolved in 20mM HEPES (Thermo Fisher Scientific) pH8.0 buffer and the concentration were determined by absorbance at 280 nm.

For chemical additives used for increasing adhesion, we tested 4 candidates: tannic acid (VWR), TLC, 3,4-DHB, and HPMC (Thermo Fisher Scientific). The TLC and 3,4-DHB were a gift from Prof. Roberto Andresen Eguiluz and Dr. Syeda Tajin Ahmed. Silk-tannic acid scaffold solution was 1% tannic acid and 2% silk. Silk-TLC scaffold solution was made at two concentrations, 50µM TLC with 2% silk, and 500µM TLC with 2% silk. Silk-3,4-DHB scaffold solution also was made at two concentrations, 50µM 3,4-DHB with 2% silk, and 500µM 3,4-DHB with 2% silk. Silk-HPMC scaffold solution was made with three formulations, 0.75% HPMC with 2% silk, 1.5% HPMC with 2% silk, and 3% HPMC with 2% silk. All these scaffolds' solution was aliquoted to 200µL in 1.5 mL centrifuge tubes and frozen at -80°C for 2 h followed by lyophilizing to make the scaffold.

To determine the best candidate for decreasing the disintegration of Silk-HPMC discs, we tested 3 additives: PEG (polyethylene glycol 400, Merck KGaA, Darmstadt,

Germany), glucose (Thermo Fisher Scientific), and glycerol (Thermo Fisher Scientific). Silk-HPMC-PEG scaffold solution was made with 1% PEG, 3% HPMC, and 2% silk. Silk-HPMC- glucose scaffold solution was made with 15% glucose, 3% HPMC, and 2% silk. Silk-HPMC- glycerol scaffold solution was made with 1% glycerol, 3% HPMC, and 2% silk. All these scaffolds' solutions were aliquoted to 1mL in 24-well plates followed by using one of two processing conditions. The first condition ("condition 1") was to cool the samples to -80°C and then freeze-dry the samples, followed by annealing in an 80°C water bath for 4 days. The second condition ("condition 2") was to annealing samples in an 80°C water bath for 1 hour to allow HPMC polymerization, and then cool the samples to -80°C, freeze-dry the samples, followed by annealing in an 80°C water bath for 4 days. All samples were dried in a 50°C incubator for 2 hours after the processing mentioned above. This results in a flat cylindrical disc of diameter 1.6 cm. The thickness is 0.4 cm for discs made with 1mL silk-based solution, and 0.8 cm for those in the silk adhesion tests (below) that were made with 2 mL silk-based solution.

The discs for sustained release of Grft experiments include Silk-Grft, Silk-HPMC-Grft, and Silk-HPMC-Glycerol-Grft. Silk-Grft scaffold solution was made with 10 µM Grft and 2% silk. Silk-HPMC-Grft scaffold solution was made with 10 µM Grft, 3% HPMC, and 2% silk. Silk-HPMC-Grft scaffold solution was made with 10 µM Grft, 3% HPMC, 1% glycerol, and 2% silk. All these scaffolds' solutions were aliquoted to 1mL in 24-well plates followed by condition 2 (above) processing. All samples were dried in a 50°C incubator for 2 hours after the processing. To sterilize the samples for the Grft release experiments (because the Grft was later used in pseudoviral assays with mammalian cells), the discs were placed in a biosafety cabinet with the UV light on for 1 hr before adding PBS.

The discs for the tissue adhesion test, Silk, Silk-HPMC, Silk-HPMC-Glycerol, and Silk-HPMC-Glycerol-Grft, were made the same way as the discs for sustained release of Grft experiments, except each disc made in 2 mL solution in 24-well plates to allow a thicker disc that can be more easily tested with hanging weights.

The discs for the degradation experiment were made under processing condition 2, including 2%Silk-3%HPMC, 2%Silk-3%HPMC-1%PEG, 2%Silk-3%HPMC-15%Glucose, 2%Silk-3%HPMC-1%Glycerol, and 2%Silk-3%HPMC-1%Glycerol-10 µM Grft.

For FTIR experiments, the unannealed discs were the same formula solution as the discs for sustained release of Grft experiments followed with freeze-drying without annealing (that is, without further processing in a water bath or being placed in a warm incubator). The annealed discs were made the same way as the discs for sustained release of Grft experiments.

The colorful silk-based discs were made by adding small amounts of green, red, blue and yellow food coloring (McCormick, Hunt Valley, MD) to the silk solution and placing it into shaped molds rather than 24 well plates, followed by lyophilization with no further processing.

6.3.5 Morphology of silk-based discs

The interior morphology of the silk-based discs was assessed by Scanning Electron Microscopy (SEM), a Zeiss EVO MA10 electron microscope (Carl Zeiss AG, Germany). The samples were cut to expose the cross sections and mounted onto SEM

stubs and coated with gold via a SC7620 sputter coater (Quorum Technologies, UK). The diameter of the pore in each image was measured by the average of 20 pores in ImageJ.

Fourier-transform infrared spectroscopy (FTIR; JASCO FTIR 6200 spectrometer, Jasco, USA or a Bruker Vertex 70 spectrometer, Germany) was used to evaluate the secondary configurations of silk-based discs as described previously [51]. The amide I region (1585 to 1720 cm−1) was overlayed to compare the β-sheet content.

6.3.6 Adhesion tests

The preliminary adhesion tests were carried out by placing a silk-based disc on the wet surface of the sample skin (chicken skin from commercial sources) and using a tweezer to lift the disc to see whether the disc could adhere well enough to draw up the tissue when pulled (supplementary video 1). If it was able to pull up the tissue, then it was considered a candidate for further experiments.

To measure the adhesion differences among the 4 SF-based discs, called: Silk, Silk-HPMC, Silk-HPMC-Glycerol, and Silk-HPMC-Glycerol-Grft, the retention time that a disc could remain attached to the tissue under a pulling force was recorded. First, the tissue was rinsed and submerged in PBS for 5 min, and then was stabilized against a glass surface horizontally (measuring 10 cm x 7.4 cm). An SF disc was placed on the tissue with brief finger pressure, then incubated for 5 min and allowed to adhere, followed by rotating the set-up to a vertical orientation. Under these conditions it was found that the discs were able to adhere indefinitely. So a further test of adherence to the skin was carried out using small weights (12 g total) attached to the disc. The length of time that a disc retained its hold on the tissue was measured (Figure 4A).

6.3.7 Measurement of sustained release of Grft from the SF discs

The Grft released from 3 SF-based discs, including Silk-Grft, Silk-HPMC-Grft, and Silk-HPMC-Glycerol-Grft, were measured by BLI (biolayer interferometry) (Gator Bio, Palo Alto, CA, USA). To test for Grft release, 1 mL of PBS was added into each disc-containing well (of the 24-well plate) and incubated in a 37°C incubator. The initial "burst" effect of release was collected after the first hour by removal of the PBS, and the solution replaced with fresh PBS. Later time points were taken daily for 7 days, each time collecting the PBS solution and replacing it with fresh PBS.

The concentration of Grft from these timepoints was then determined by a BLI quantitative assay. First, a standard curve was made, using pure Grft that had not been in a disc. For this, several standard Grft concentration solutions were made in PBS at pH 7.4. Four standard concentration solutions were measured by BLI and compared to two sustained release samples, and one PBS buffer at the appropriate pH as a control. All samples were centrifuged 3 min at 15,000 rpm to remove debris before measurement. The pH of the samples that were collected by soaking at pH 4.0 were adjusted to pH 7.4 to allow the His6-tag on Grft to have the protonation state to bind to the BLI anti-Histag sensor. Each type of disc was measured in triplicate, with three separate samples.

6.3.8 HIV inhibition assays

The inhibition of Grft in the sustained release solutions mentioned in 2.7 (above) was tested for its activity against PVO.4 infection of TZM-bl cells [51,326] In brief, 6,000 TZM-bl cells were seeded in a 96-well plate (100 µL per well) and incubated for 16 h. Then the

medium was removed and 20 µL of HIV-pseudovirus PVO.4 was added. For no-virus control wells, 20 µL/well of cell medium were added. Then, 15 µL medium and 15 µL of Grft sample was added. For negative control wells, 15 µL medium and 15 µL/well of pH 7.4 PBS were added. After 10 h infection, 160 µL of media was added into each well and incubated at 37°C for another 36 h.

The viral infection in TZM-bl cells was measured by luciferase quantification of cell lysates using Bright-Glo Luciferase Assay System (Promega, Madison, WI, USA). In brief, of the media was removed, leaving 20 µL in each well; then 20 µL of Bright-Glo Luciferase Assay System solution was added and allowed to react 3 min. After that, the cells and solution are transferred into a white 96-well plate (OptiPlate-96, PerkinElmer, Valencia, CA) and incubated at room temperature for 5 min, followed by reading the luminescence signal on a CLARIOstar plate reader (BMG Labtech, Cary, NC).

6.3.9 Biocompatibility assays

The biocompatibility of the Silk-HPMC-Glycerol-Grft disc was assessed by an MTT assay. In brief, HEK-293Ft cells (Homo sapiens, embryonic kidney cells; a gift from Dr. David Gravano, University of California, Merced) were seeded into a 96-well plate at a density of 10,000 cells per well with 90 µL of culture media and 10 µL of sample (the day 6 sustained release solutions mentioned in 2.7) or pH 7.4 PBS (control). The cells were cultured at 37°C for 24 hours. After that, the cell viability was measured by following the protocol of the MTT Cell Proliferation Assay Kit (Cayman Chemical, Ann Arbor, MI).

6.3.10 Degradation evaluation

The degradation of the silk-based discs, including Silk-HPMC, Silk-HPMC-Glycerol, and Silk-HPMC-Glycerol-Grft, Silk-HPMC-PEG, Silk-HPMC-Glucose, were measured by immersing the discs in a 24-well plate with 2mL of PBS (pH 7.4 or both pH 7.4 and pH4.0 for Grft-containing discs) in each well and incubated at 37°C for 7 days. After that, each disc was placed in a 2mL centrifuge tube and spun down for 10 min at 15,000 rpm. Then the supernatant was removed and the pellets was vacuum-dried with a speed-vac at 60°C for 5 hours. The remaining dry weight (%) is an indicator of each disc's extent of degradation. Silk-HPMC-Glycerol-Grft discs' degradation experiments were done in triplicate at both pH7.4 and pH4.0 PBS. Other discs' degradation experiments were done in duplicate in PBS pH7.4.

6.3.11 Statistical and mathematical analysis

Degradation evaluation One-way and two-way ANOVA (Excel) was applied to evaluate the differences among several groups. Student's t-test (Excel) was utilized to compare two groups' differences. Both ANOVA and Student's t-test alpha value was 0.05. The probability p-value less than 0.05 was considered statistically significant; NS indicates $p > 0.05$; * indicates $p < 0.05$; ** indicates $p < 0.01$.

6.4 Results

6.4.1 HPMC increases the adhesion of the silk discs to sample tissue

To test adhesion in a biological system, moist animal skin was used. The biological tissue used in this study was chicken skin, from Cornish Cross chickens. While not as close a mimic to human skin as porcine skin [345,346], chicken skin has both an epidermis and a dermis (like human skin), and has several similar components, including collagen, elastin, and keratinocytes [347,348]. Additionally, the advantage of being inexpensive and available commercially in large amounts makes it good candidate for preliminary studies. A simple formulation of SF and Grft can adhere to a surface containing the skin but its adhesion is not strong, as evidenced by its easy removal from the surface with a tweezer (Supplemental video 1). Therefore, four candidates, tannic acid, TLC, 3,4-DHB, and HPMC, were blended with silk solution individually to form discs and each disc (2% final SF) was tested for adhesion to the tissue. The silk films that included tannic acid showed significant precipitation on the side of the well and did not form sponge-like discs, so tannic acid was judged to be an unacceptable additive for this work. Discs made of SF/TLC and SF/3,4-DHB were tested at two concentrations of the additive (50µM and 500µM). While these did form sponge-like discs, none of them were able to adhere to moist skin that had been hydrated with either pH 7.4 or pH 4.0 PBS. Finally, discs were formulated with 3% HPMC and 2% silk fibroin in a total of 1mL solution. This formed a disc that adhered well to skin (Supplementary video 1). Lower HPMC concentrations were also used (1.5% and 0.75%) but these showed less ability to adhere to the tissue (data not shown), so 3% HPMC was used in further experiments.
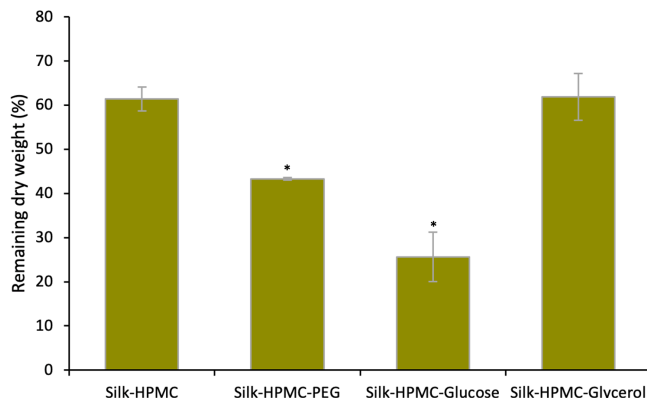
Figure 6.1 The remaining dry weight (%) from a degradation experiment of silk-based discs

Discs were immersed in PBS pH 7.4 for 7 days at 37°C. Silk-HPMC-Glycerol showed the combined properties of lower degradation and better ability to hold its shape. Two-way ANOVA shows significant differences among groups. The Student's t-test was applied to evaluate the extent of differences between Silk-HPMC and other discs. * indicates $p < 0.05$.

6.4.2 Glycerol decreases the disintegration of Silk-HPMC discs

While 2% silk-3% HPMC discs adhered well to model skin samples, these discs did not hold their shape, and under some conditions (such as when silk discs were not annealed) disintegrated on the wet tissue in 30 minutes. This property would be favorable in a situation where rapid drug release and quick protection are a priority. However, this

would not be ideal for use as a sustained release device to allow several days or weeks of protection. Therefore, additives were sought to slow the degradation of the film. Three candidates, PEG 400, glucose, and glycerol, which have been reported to increase the crystallinity of the silk scaffold [349,350], were used. In this study, for 1mL working solution, the silk final concentration was 2%, and the HPMC final concentration was 3%. The candidates' concentrations were (separately) PEG 1%, glucose 15%, and glycerol 1%. The results showed that over the course of a week incubated in PBS pH 7.4, Silk-HPMC-Glycerol scaffolds held their shape and degraded (as judged by remaining dry weight) approximately as much as Silk-HPMC. Both of these showed less degradation than Silk-HPMC-PEG, and Silk-HPMC-Glucose scaffolds (Figure 6.1). Therefore, Silk-HPMC-Glycerol was judged to have desirable properties for further study.

6.4.3 The morphology and FTIR spectra of the silk discs

The 4 silk-based discs, Silk, Silk-HPMC, Silk-HPMC-Glycerol, and Silk-HPMC-Glycerol-Grft, processed with condition 2, were cut to expose the internal structure and evaluated via scanning electron microscopy (SEM; Figure 6.2A-D). The control Silk disc (with no additives) has smaller pores with diameter 20 ± 9 μm in its structure compared to the other three types of discs. Only small visual differences were observed among Silk-HPMC (diameter 68 ± 30 μm), Silk-HPMC-Glycerol (diameter 120 ± 70 μm), and Silk-HPMC-Glycerol-Grft (diameter 82 ± 60 μm) discs.
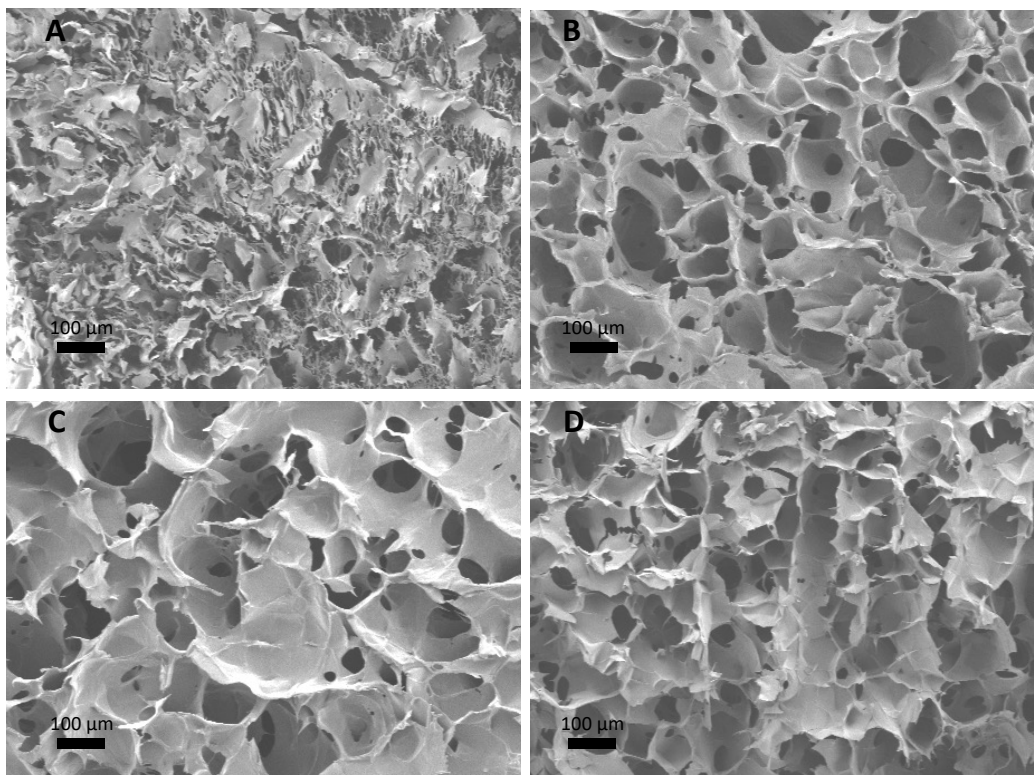
Figure 6.2 SEM images of the 4 silk-based scaffolds

A. control silk disc. B. Silk-HPMC disc. C. Silk-HPMC-Glycerol disc. D. Silk-HPMC-Glycerol-Grft disc. Pore size was measured with ImageJ.

FTIR was performed to analyze the protein secondary structure of the 4 silk-based discs (Figure 6.3A-B). For unannealed (no processing after simple lyophilization) 4 silk-based discs, Silk-HPMC-Glycerol has higher β-sheet content (wavenumber 1,619-1,628 and 1,697-1,703 cm^{-1}) [351] than the other three discs. After processing with the condition 2, however, the annealed 4 silk-based discs all transformed into more β-sheet structure to form silk II assembly which is an organized crystalline form of fibroin and can slow down the degradation of the discs [351].
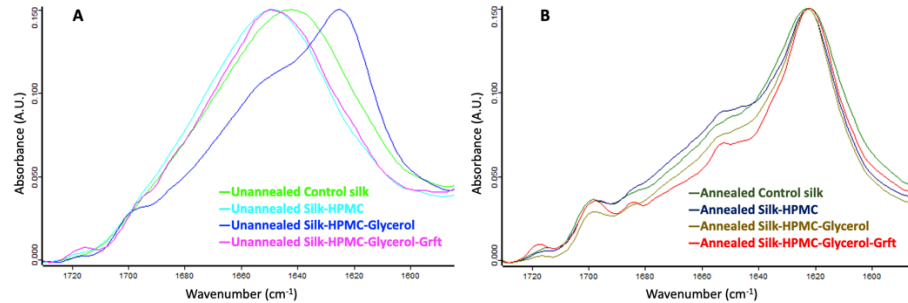
Figure 6.3 FTIR spectra of 4 silk-based scaffolds, unannealed and annealed

A. Unannealed scaffolds: control silk (light green), Silk-HPMC (light blue), Silk-HPMC-Glycerol (blue), and Silk-HPMC-Glycerol-Grft (magenta). B. Annealed scaffolds: control silk (green), Silk-HPMC (dark blue), Silk-HPMC-Glycerol (brown), and Silk-HPMC-Glycerol-Grft (red). Unannealed refers to SF scaffolds that are not further processed beyond lyophilization. Annealing refers to processing under humid conditions as described in Methods 2.4 (condition 2).
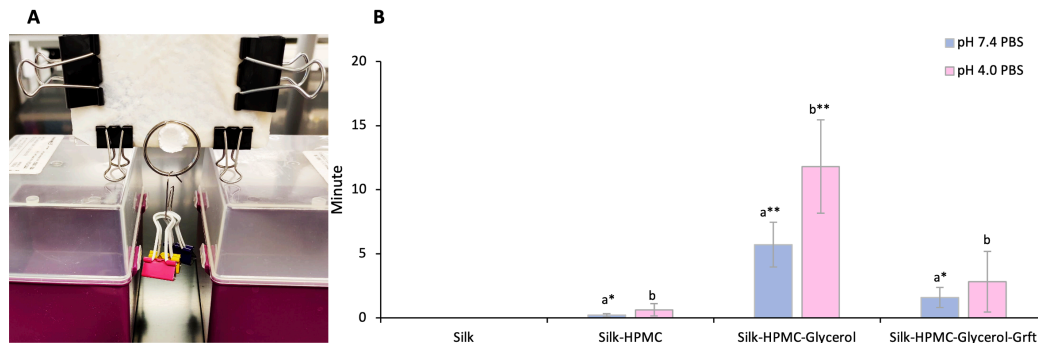
Figure 6.4 Adhesion test of the 4 silk-based scaffolds

A. The set up of the adhesion test. A silk disc is placed on chicken skin that was stabilized on a glass surface and then oriented perpendicular to the table. All silk discs were able to remain on the skin for at least 2 hours under these conditions. To further test adherence to the biological surface, a weight was added to the disc (a ring and three clips connected to the ring). The time was measured until the silk disc fell from the biological surface. B. The time that various formulations of silk disc could remain adhered to the surface in the presence of a 12 g weight; pH 7.4 (blue) and pH 4.0 (pink). Two-way ANOVA shows significant differences among groups. The Student's t-test was applied to evaluate the extent of differences between different groups; a, significance between silk and other discs at pH 7.4; b, significance between silk and other discs at pH 4.0. There was no significant difference within each disc at pH 7.4 and pH 4.0. * indicates $p < 0.05$; ** indicates $p < 0.01$. The p value for Silk-HPMC-Glycerol-Grft compared to the Silk alone is 0.1 due to the large variation of the adhesion time.

6.4.4 Adhesion of the 4 silk-based discs

Adhesion of the 4 silk-based discs, Silk, Silk-HPMC, Silk-HPMC-Glycerol, and Silk-HPMC-Glycerol-Grft, to the tissue (chicken skin) was tested under two pH conditions, 7.4 and 4.0. These pH values were chosen to mimic the pH environment of the rectal area and vaginal area, respectively. Each type of disc was made from 2 mL solution with condition 2 processing, and was measured in triplicate, with three separate samples. The tissue was washed and soaked with PBS and then clamps were used to stabilize the tissue on a horizontal glass surface. Then one of the silk discs was placed on the tissue for 5 minutes (to approximate a user inserting the disc and then carrying out an activity such as walking soon thereafter), and then the surface was rotated to a vertical orientation. Under these conditions, each silk film adhered to the surface indefinitely. Because actual use may include various forces on the insert, small weights were added to determine the robustness of adherence (total weight 12 g). The length of time that the disc was able to retain its hold on the skin with weights attached was measured (Figure 6.4A). The control silk discs had no retention time, falling off the tissue immediately at both pH 7.4 and 4.0. The Silk-HPMC discs did adhere longer, falling at 13 ± 7.6 seconds at pH 7.4 and 38 ± 28 sec at pH 4.0 on average. The weighted Silk-HPMC-Glycerol discs adhered to the vertical surface most tightly, attaching to the tissue 320 ± 86 sec at pH 7.4, and 710 ± 220 sec at pH 4.0 on average. The Silk-HPMC-Glycerol-Grft discs showed good adherence, being able to maintain their position on the vertical surface while weighted for 96 ± 48 sec at pH 7.4 and 170 ± 140 sec at pH 4.0 on average.

6.4.5 Silk-HPMC-Glycerol-Grft discs show sustained release of griffithsin

It is important that a disc formulated with Grft retains its ability to release Grft when used. Further, while some users may prefer immediate protection from insertion of a disc, the key benefit of using a biocompatible, non-immunogenic, naturally-sourced material for the discs (i.e. silk fibroin) is that it can be well tolerated over several days of continuous contact with the human body, and can sustained release therapeutics over a certain period of time. Therefore, the discs were tested to determine the level of Grft released. For these experiments, biolayer interferometry (BLI) was used. This is a relatively facile technique that can monitor the amount of a protein that binds to a solid support by measuring the change in wavelength of light shone through the probe upon binding. Since Grft retains a 6-His tag (which has been shown to not affect its activity) the protein readily binds to a commercial BLI sensor. BLI was used to evaluate the sustained release of griffithsin from the 3 silk-based discs, including Silk-Grft, Silk-HPMC-Grft, and Silk-HPMC-Glycerol-Grft. (When tested for degradation, Silk-HPMC-Glycerol-Grft discs retained 46% of their dry weight after 1 week; the same discs without Grft retained 62% of their dry weight under the same conditions. Discs containing PEG or glucose were not considered because those additives did not slow the degradation of the disc, as shown in Figure 6.1.) Each type of disc encapsulated 147 µg Grft (10 µM final concentration) in 1 mL of silk scaffold solution followed with the condition 2 processing to formulate the discs. All experiments were carried out in triplicate. The silk discs were soaked in pH 7.4 and pH 4.0 PBS solution to represent colorectal and vaginal conditions respectively. At various time points, the incubation solution was removed and replaced with fresh PBS (again at pH 7.4 and pH 4.0 respectively), and the Grft released from the discs was measured (Figure 6.5 A-H). No obvious burst release of Grft in the 1st hour was observed in any of the discs: Silk-HPMC-Glycerol-Grft (2.2 µg (147nM) at pH 7.4 and 3.0 µg (207nM) at pH 4.0, representing ~2% of the total amount of Grft loaded); Silk-Grft discs (4.9 µg (336nM), representing ~3%);

and Silk-HPMC-Grft discs (9.2 μg (623nM), representing ~6%). Rather, in each case, steady release was observed. The accumulated release of Grft in Silk-HPMC-Glycerol-Grft discs after 7 days was ~17 μg in pH 7.4 PBS, and ~24 μg in pH 4.0 PBS. The accumulated release of Grft in Silk-HPMC -Grft discs after 7 days was ~46 μg and ~27 μg in Silk-Grft discs in pH 7.4 PBS.
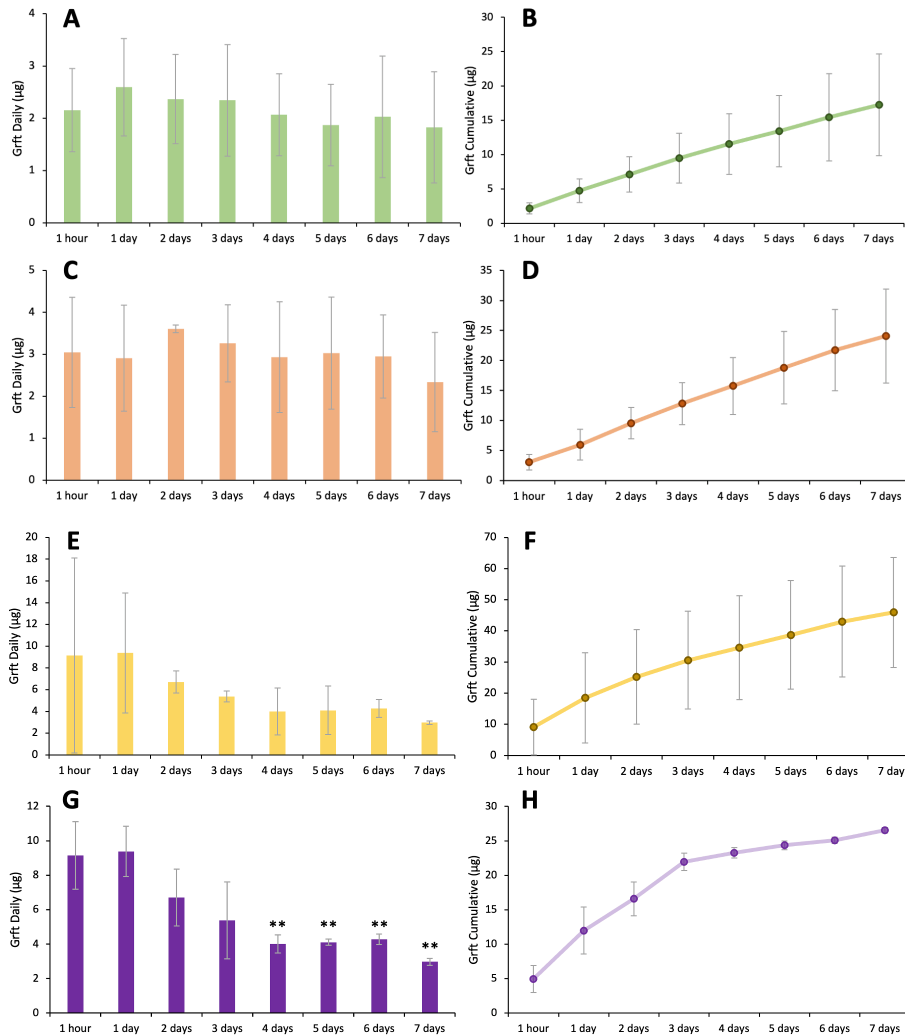
Figure 6.5 Sustained release of Grft from silk-based disks

A. The sustained release of Grft from Silk-HPMC-Glycerol-Grft disks in pH 7.4 PBS. B. The ac-cumulated release of Grft from Silk-HPMC-Glycerol-Grft disks in pH 7.4 PBS. C. The sustained release of Grft from Silk-HPMC-Glycerol-Grft disks in pH 4.0 PBS. D. The accumulated release of Grft from Silk-HPMC-Glycerol-Grft disks in pH 4.0 PBS. E. The sustained release of Grft from Silk-HPMC-Grft disks in pH 7.4 PBS. F. The accumulated release of Grft from Silk-HPMC-Grft disks in pH 7.4 PBS. G. The sustained release of Grft from Silk-Grft disks in pH 7.4 PBS. H. The accumulated release of Grft from Silk-Grft disks in pH 7.4 PBS. All discs were processed with condition 2 (Methods section 2.4). No significant differences were observed in the results of A, C, E evaluated over the 7 day experiment by one-way ANOVA. For G, significant differences were observed within the timepoints and the Student's t-test was applied to evaluate the extent of dif-ferences between 1 day and the other timepoints; ** indicates $p < 0.01$.

6.4.6 The griffithsin released from the Silk-HPMC-glycerol-Grft discs shows inhibitory activity against HIV in vitro

In order to determine whether the griffithsin released from Silk-HPMC-Glycerol-Grft discs is functional and capable of HIV inhibition, the day 6 solution taken from both pH 7.4 (mimicking colorectal condition) and pH 4.0 (mimicking vaginal condition) samples were tested against HIV-1 pseudovirus PVO.4 in TZM-bl cells. The results showed that the Grft released from the disc at both pH 7.4 and 4.0 can fully inhibit the HIV pseudovirus (Figure 6.6). In order to determine the biocompatibility of Silk-HPMC-Glycerol-Grft discs, the day 6 solution taken from the pH 7.4 Silk-HPMC-Glycerol-Grft sustained release experiment was evaluated by an MTT assay upon incubation with HEK 293Ft cells. The results showed that the cell viability of both the sample and the control (pH 7.4 PBS) are the same, which in turn indicates the Silk-HPMC-Glycerol-Grft has good biocompatibility (data not shown).
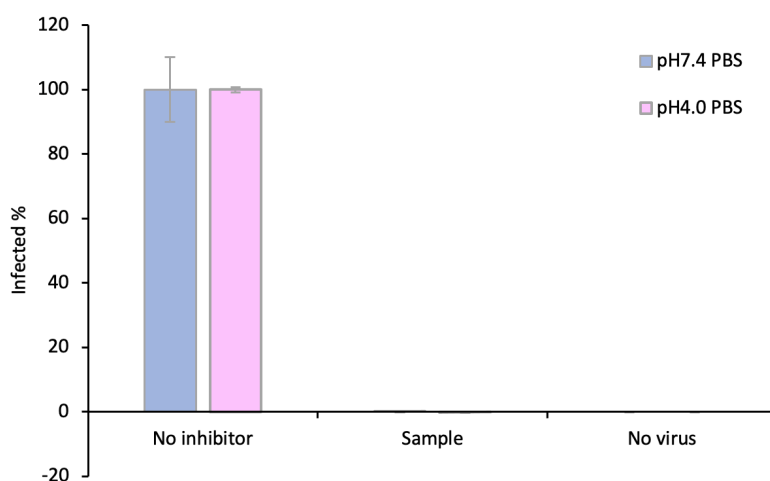
Figure 6.6 The Grft released from Silk-HPMC-Glycerol-Grft disks showed strong inhibition against HIV at both pH 7.4 and pH 4.0 PBS

The day 6 solution taken from both pH 7.4 (gray) and pH 4.0 (purple) samples were tested against HIV-1 pseudo virus PVO.4 in TZM-bl cells. Left: the solution from Silk-HPMC-Glycerol (no Grft). Middle: Solution from Silk-HPMC-Glycerol-Grft from Day 6. Right: TZM-bl cells alone without virus.

6.5 Discussion

Although advances in antiretroviral therapy (ART) have shown great effectiveness in the suppression of HIV replication and in preventing HIV acquisition, there are still challenges for HIV eradication and prevention of new infections. There are several choices on the market for pre-exposure prophylaxis (PrEP), including a daily pill, and a recently-approved injectable, Apretude (cabotegravir extended-release injectable suspension), which can be given every two months to reduce the risk of HIV acquisition [352]. Other forms of PrEP have been incorporated into scaffolds to form microbicides, including sponge-like discs, creams, gels, films, intravaginal rings (IVR), and tablets, which can be applied topically to the vagina or rectum to avoid sexual acquisition of HIV [307,353]. Among these, the dapivirine vaginal ring showed effectiveness in women over 25 years old, and in 2021, WHO recommended the ring as an additional prevention option for women; several Africa

countries have approved its usage for prevention of HIV [354]. While clinical trials have included several types of insertable device that are likely to be effective if used consistently, results often show low adherence among users, particularly young women, leading to low protection in this group [355–360].

Currently, only half of HIV-infected people are receiving anti-retroviral therapy [361], suggesting a large pool of people who could actively transmit HIV if their partner is not protected. Therefore, there is an urgent need for affordable, easy to apply, and long-lasting prevention approaches, especially for young women who tend to have lower compliance with pills, gels and rings in clinical trials [357,362–364].

We have been working on a silk fibroin-based drug delivery platform that is thermostable (able to be stored without refrigeration) and can be readily applied to the vaginal and rectal mucosal sites. We have shown that SF is able to stabilize HIV inhibitory proteins for over a year at high temperatures, and that it can release various proteins over the course of a month [51,326]. Further, in pre-clinical trials in macaques we showed that SF-Grft discs provide protection to both vaginal and rectal tissue [362]. This platform has the added benefit of being able to be formulated into visually pleasing shapes that also have favorable tactile properties (Figure 6.7). SF has emerged as a promising drug carrier of bioactive compounds including small molecules, protein drugs, and antibodies that has superior biocompatibility and tunable biodegradation [326,365].

Figure 6.7 The Silk-based discs can be formed into different shapes and colors can be added

For this photo, the discs are simply composed of silk fibroin (2%) solution with additional food dye.

Griffithsin is a protein lectin that has been shown to inhibit many viruses including HIV-1 and SARS-CoV-2. This protein, one of the most potent HIV inhibitors with inhibition constants rivalling antibodies, binds to the high-mannose region of the HIV-1 gp120 protein to block its entry to the host cells [328,330]. It has been used in several preclinical trials, including with gel inserts that showed inhibition of SHIV, HSV-2 and HPV infections *in vivo* [247,331,333,334,366–369]. Grft and its variant Q-Grft has been shown to be amenable to both rapid release and sustained release from silk fibroin discs and various polymer fibers and nanoparticles [51,368,370,371]. Recently, Grft-based microbicides in the form of a gel and douche (for vaginal and rectal compartments respectively) have been evaluated in clinical trials, showing no significant adverse events with the epithelium and CD4+ cell distribution remaining unchanged [366,372,373]. In addition, Grft has been shown to potently inhibit SARS-CoV-2 live virus infection in Vero E6 cells with half maximal inhibitory concentration (IC50) of 63 nM[374] and 33.2 nM reported respectively [375]. Furthermore, a variant of Grft that is stable to oxidation, Q-Griffithsin, has been formulated into an Intranasal Spray and is in clinical I trials to evaluate its safety, tolerability, and pharmacokinetics (ClinicalTrials.gov Identifier: NCT05437029). So far, results show that the Q-Griffithsin Intranasal Spray is safe and effective, since no dose accumulation effect or systemic exposure was observed, and no severe adverse events were reported [376].

Our work with SF discs in the past has shown success in both quick-dissolve and sustained release of Grft, in amounts that effectively inhibit HIV infection, indicating that SF-Grft is a promising microbicide candidate that may be complementary to the current PrEP treatment to mitigate inconsistent user adherence. (Indeed, in preliminary focus groups silk discs were well received; data not shown). However, while the SF discs show many properties that are valuable including low cost, facile formulation and stability at high temperature, the lack of sustained adhesion to the mucosal surface could limit their effectiveness.

To enhance the SF discs' adherence to the mucosal surface, we investigated four water soluble and biocompatible chemical additives: tannic acid, TLC, 3,4-DHB, and HPMC, which contain multiple hydroxyl groups to improve SF-based scaffolds' hydrophilicity and may improve its adhesion to a tissue in a wet environment [377]. Tannic acid is a food additive approved by the FDA [378] and a Silk-Tannic acid gel has been shown to adhere to rabbit liver, heart and skin [377]. TLC is a siderophore analogue that showed adhesion on solid ionized silica in aqueous solutions [379]. 3,4-DHB, is a metabolite of some food, such as olives, white grapes, and green tea, and has been shown to have anti-inflammatory activities [380]. HPMC is a cellulose ether, and is a food additive as well as having been shown to have mucoadhesive properties [381]. SF-HPMC electrospun scaffolds have been demonstrated to have excellent biocompatibility for human umbilical vein endothelial cells' adhesion and proliferation [382]. Our results showed that the Silk-tannic acid does not form into a useable disc after the freeze-drying process. TLC and 3,4-DHB made acceptable discs but did not improve adhesion to tissue over simply SF alone. The addition of HPMC did enhance the adhesion by silk fibroin discs to a tissue without compromising its shape, but the Silk-HPMC disc alone disintegrated in PBS within half an hour. While this is favorable for near-instantly accessible protection, some users may prefer longer-term protection.

There are multiple strategies for tuning the silk fibroin degradation rate, such as adjusting β-sheet crystallinity, manipulating molecular weight of the silk polymer, controlling the degree of cross-linking, and doping with other molecules [383]. High molecular weight, more β-sheet crystalline regions, and fibrillar structure at the nanoscale level are associated with a lower degradation rate [383]. Here we used doping and recrystallization to slow down the disintegration of the Silk-HPMC disc. Recrystallization in this context is a process that transforms α-helices/random coils to highly oriented β-sheet crystals which will decrease the degradation of the silk scaffolds. This can be achieved by processes such as autoclaving and water annealing [383]. PEG, glucose, and glycerol were chosen as doping candidates. PEG is a commonly used additive that is a non-ionic, hydrophilic, biocompatible and biodegradable polymer and that has been approved by the FDA for drug delivery applications since 1990 [384]. Glucose is a commonly consumed food; it has been reported that the addition of glucose into silk fibroin induced SF crystallization and enhanced the flexibility of SF films, promoting the wound healing process [349]. Glycerol is used widely in skin and cosmetic products and is an ingredient in wound and burn treatments approved by the FDA [378,385,386]. Solid-state NMR analyses indicated that glycerol induces SF β-sheet formation [350]. The results presented here show that the Silk-HPMC-Glycerol discs processed with condition 2 (with annealing at 80°C before freeze-drying) has the slowest disintegration rate, compared with other doping chemicals and the control Silk-HPMC disc.

We then incorporated Grft into the Silk-HPMC-Glycerol formulation to form a Silk-HPMC-Glycerol-Grft disc with the condition 2 processing, and evaluated its morphology, FTIR spectra, adhesion, the sustained release of Grft, as well the ability of the released Grft to inhibit single-round HIV in vitro. SEM images showed the cross section of the Silk-HPMC-Glycerol-Grft disc has a porous structure similar to Silk-HPMC, and Silk-HPMC-Glycerol. FTIR spectra demonstrated that doping with glycerol increased the β-sheet formation in the Silk-HPMC disc, and that all silk-based discs, Silk-HPMC, Silk-HPMC-Glycerol, and Silk-HPMC-Glycerol-Grft, converged to form more β-sheet structure after processing with condition 2.

The discs' adhesion to tissue from stronger to weaker was found to be Silk-HPMC-Glycerol > Silk-HPMC-Glycerol-Grft > Silk-HPMC > Silk disc. These results were consistent at both pH 7.4 (to mimic a rectal environment) and pH 4.0 (to mimic a vaginal environment). In general, adherence at the lower pH was more robust. When using the disc alone with no drag force, the discs were able to remain on the vertical surface indefinitely. It is also noteworthy that the doping of glycerol not only improves the adhesion of Silk-HPMC disc to the tissue but slows down the disintegration of the disc.

The level of sustained release of Grft from 3 silk-based discs, Silk-Grft, Silk-HPMC-Grft, and Silk-HPMC-Glycerol-Grft, was measured by BLI. The results showed that all of the discs are able to release substantial amounts of Grft in quantities that are fully inhibitory for at least 7 days, and none of them has a high burst release of Grft in the first hour. Both the lack of a burst and the continuous release of effective amounts indicates that these formulations have excellent properties that could be useful in a therapeutic device. The discs reported here could be expected to adhere to the mucosal surface within minutes of insertion. While it is not expected that the disc will necessarily remain in place during sexual activity, the released Grft should be protective within hours. As we have shown with more simple SF devices, the Grft released from a silk scaffold (in this case the Silk-HPMC-Glycerol-Grft discs) remained active, showing full inhibition against HIV-1 single round virus pseudotyped with PVO.4 in TZM-bl cells. In addition, the MTT assay showed Silk-HPMC-Glycerol-Grft discs have good biocompatibility with the same cell survival as with PBS alone. Therefore, due to the urgent need for affordable and acceptable microbicides, the Silk-HPMC-Glycerol-Grft disc presented here is a good candidate, being inexpensive, easy to store without refrigeration, and having high potency against HIV. Additionally, it can be formed in a variety of colorful shapes which may lead to higher adherence for at-risk youth.

6.6 Conclusions

In this study, we present a silk fibroin-based drug delivery system that provides sustained release of griffithsin as well as showing adhesion to tissue, indicating likely adhesion to mucosal surfaces that are vulnerable to infection. These SF discs are directly relevant for protection against HIV, and the Grft inhibitor has also been shown to be effective against other viruses such as HPV and SARS-CoV-2. The work involves the addition of HPMC to silk fibroin for improvement of adhesion, and the use of glycerol as a doping agent to reduce the degradation process of the Silk-HPMC disc. The resulting discs (Silk-HPMC-Glycerol-Grft) can adhere to sample skin tissue, and achieve sustained release of active Grft for at least 7 days. This formulation could be applied toward making a variety of biologically useful insertable devices or skin patches that can deliver active

compounds ranging from small molecules to proteins to mucosal protective microoganisms.

Chapter 7

Future Directions

The chemokine system is complex and diverse, playing a fundamental role in coordinating various aspects of biological process, such as organ development, angiogenesis and immune response [1,387]. Chemokines function by binding to specific G protein-coupled receptors (GPCRs) on the surface of target cells, and many receptors can bind multiple chemokines with different affinities [388,389]. Chemokines can attract a wide range of immune cells.

As we mentioned in Chapter 1, chemokines can be divided into 4 subfamilies, CC, CXC, C, CX3C. CC chemokine is the largest subfamily, has 28 members, mainly target macrophages, eosinophils, and basophils; CXC chemokine subfamily, has 16 members, generally attract neutrophils and lymphocytes [389,390]. C chemokine subfamily have two members, XCL1 (lymphotactin) and XCL2, which have been reported to mediate the migration of T cells and NK cells [391,392]. CX3C chemokine subfamily only has one member discovered till now, CX3CL1 (fractalkine), which is a multimodular protein containing a chemokine domain, and its cognate receptor, CXCR1, which has been found on macrophages, microglia, T cells, and astrocytes [393,394].

Chemokines can also be classified into 2 categories, inflammatory and homeostatic, based on their physiological features [395]. Inflammatory chemokines are produced by inflamed resident cells (non-recirculating) when stimulated by pro-inflammatory cytokines or pathogenic agents and their release can be triggered under inflammatory conditions [395,396]. The inflammatory chemokines can recruit effector cells, such as monocytes, granulocytes, and effector T cells, to inflamed sites. Homeostatic chemokines are expressed at non-inflamed sites within lymphoid or non-lymphoid tissues, including skin, intestine and mucosa, to control cells, such as lymphocytes, positioning during tissue development or maintenance [395,396]. Most chemokines functional classification into either inflammatory, including CCL2, CXCL2, and CX3CL1, or homeostatic, such as CCL21, XCL1, CXCL12, but a few chemokines possess both properties and called mixed function chemokines, such as CCL17, CCL20, and CCL22 [395–398].

Any malfunction of chemokines may lead to the diseases, including asthma, atopic dermatitis, traumatic brain disease, etc. Therefore, understanding the complexity and diversity of the chemokine system is important for developing therapeutic candidates to modulate immune responses effectively. Our lab has been working on chemokines for decades, and we found vCCI is a potent CC chemokine inhibitor which can be modified to inhibit the overexpression of chemokines.

7.1 Ongoing vCCI and chemokine projects

CCL17/TARC is a mixed function chemokine mainly expressed in the thymus and is secreted by dendritic cells (DC), endothelial cells, keratinocytes (KC) and fibroblasts [399]. It was first found to be constitutively produced in the thymus and its cognate receptor, CCR4, are predominately on T cells [400,401]. The overexpressed CCL17 has been related to a variety of diseases, including asthma, atopic dermatitis, and rheumatoid arthritis [402]. Therefore, engineering vCCI to bind CCL17 can be a potential way to alleviate the inflammation.

We know vCCI using its β sheet II and acidic loop to interact with CCL17. The hypothesis that increasing the negative charge on the vCCI β sheet II, which is a binding interface, may increase its binding affinity to CCL17 is something that should be further studied and is therefore a current lab project. When designing several vCCI mutations in complex with CCL17 by using AlphaFold and UCSF Chimera prediction, the preliminary results showed that vCCI S82E/R89E/N91E : CCL17 form the tightest complex which has 504 atoms involved in contacts. Based on the best model generated by AlphaFold of each vCCI mutant, vCCI S82E/R89E/N91E/G93D also have more residues involved in the interaction though less atoms (407 atoms) contacts. Therefore, we designed the gene of vCCI tetra mutant (S82E/R89E/N91E/G93D), triple mutant (S82E/R89E/N91E), double mutant (S82E/R89E), and single mutants (S82E and R89E). We bought vCCI tetra mutant and triple mutant from Twist Bioscience, and have undergrads made the double mutant and 2 single mutants though 2-step PCR process. After several months of work, we got all the genes and proteins except vCCI S82E since no expression of this protein. The next step of this ongoing project is to measure the binding affinity of these vCCI mutants with CCL17 though BLI and fluorescence anisotropy assay.

In Chapter 1, we listed some chemokine related inflammatory diseases (Figure 1.2), and this can shed a light on future vCCI and chemokine projects, to develop disease specific vCCI mutants to inhibit those chemokines. For example, the elevation or upregulation of CCL2, CCL4, CXCL8, and XCL1 are related to traumatic brain injury [403–406]. We can do sequence alignment with these chemokines and predict some common site that vCCI can bind in order to inhibit them to bind their receptors or GAGs. Also, Alzheimer's disease is a tough disease which has no effect cure, and the increased CCL11 and CXCL8 are associated with the Alzheimer's disease [407,408]. Therefore, engineering vCCI to inhibit CCL11 and CXCL8 might be a potential way to alleviate the symptom of Alzheimer's disease, with research currently ongoing in our lab.

7.2 Future silk projects

In Chapter 6, we showed the silk-HPMC-Glycerol-Grft scaffold can attach to the wet tissue and realize the sustained release of Grft in one week. The next step is to decrease the degradation of the scaffold to realize longer period of release of Grft, such as one month, three months, and six months. Also, we can find some collaboration with pre-clinical research, to study and improving the *in vivo* adhesion and sustained release of Grft.

vCCI is a potent CC chemokine inhibitor which can be formulated into silk scaffold to treat inflammation related disease. The Silk scaffold can be formed into different shapes, including microneedle patch, film, and 3D porous disk. Formulating vCCI into silk-based scaffold can be further applied to pre-clinical study of the treatment of certain inflammation, paving the way for vCCI as a therapeutical candidate.

7.3 Conclusion

The method used in chemokine and vCCI study can be applied to more protein-protein interaction studies, making the implications far reaching in the biomedical field. The study of vCCI-CCL17 contributes to the future study of vCCI specifically target certain

chemokines in order to alleviate inflammation caused by the chemokines. Silk-based biomedical drug delivery system can be broadly applied to the delivery of protein, antibody, and small molecule drug, since it is inexpensive, heat-stable, biocompatible, biodegradable, and user acceptable.

VII. References

1. Sokol, C. L. & Luster, A. D. The Chemokine System in Innate Immunity. *Cold Spring Harb Perspect Biol* **7**, 1–20 (2015).

2. Dogan, R. N. E. & Karpus, W. J. Chemokines and chemokine receptors in autoimmune encephalomyelitis as a model for central nervous system inflammatory disease regulation. *Front Biosci* **9**, 1500–1505 (2004).

3. Springer, T. A. Traffic signals for lymphocyte recirculation and leukocyte emigration: the multistep paradigm. *Cell* **76**, 301–314 (1994).

4. Hamel, D. J., Sielaff, I., Proudfoot, A. E. I. & Handel, T. M. Chapter 4. Interactions of chemokines with glycosaminoglycans. *Methods Enzymol* **461**, 71–102 (2009).

5. Onuffer, J. J. & Horuk, R. Chemokines, chemokine receptors and small-molecule antagonists: recent developments. *Trends Pharmacol Sci* **23**, 459–467 (2002).

6. King, J. E., Eugenin, E. A., Buckner, C. M. & Berman, J. W. HIV tat and neurotoxicity. *Microbes Infect* **8**, 1347–1357 (2006).

7. Cathcart, M. K. Signal-activated phospholipase regulation of leukocyte chemotaxis. *J Lipid Res* **50**, S231 (2009).

8. Oh-hora, M. & Rao, A. Calcium signaling in lymphocytes. *Curr Opin Immunol* **20**, 250–258 (2008).

9. Nobes, C. D. & Hall, A. Rho, rac, and cdc42 GTPases regulate the assembly of multimolecular focal complexes associated with actin stress fibers, lamellipodia, and filopodia. *Cell* **81**, 53–62 (1995).

10. Tsai, F. C., Kuo, G. H., Chang, S. W. & Tsai, P. J. Ca2+ signaling in cytoskeletal reorganization, cell migration, and cancer metastasis. *Biomed Res Int* **2015**, (2015).

11. Bacon, K. *et al.* Chemokine/chemokine receptor nomenclature. *J Interferon Cytokine Res* **22**, 1067–1068 (2002).

12. White, G. E., Iqbal, A. J. & Greaves, D. R. CC chemokine receptors and chronic inflammation--therapeutic opportunities and pharmacological challenges. *Pharmacol Rev* **65**, 47–89 (2013).

13. Wilen, C. B., Tilton, J. C. & Doms, R. W. HIV: Cell Binding and Entry. doi:10.1101/cshperspect.a006866.

14. De Wit, R. H., De Munnik, S. M., Leurs, R., Vischer, H. F. & Smit, M. J. *Molecular Pharmacology of Chemokine Receptors. Methods in Enzymology* vol. 570 (Elsevier Inc., 2016).

15. Wells, T. N. & Schwartz, T. W. Plagiarism of the host immune system: lessons about chemokine immunology from viruses. *Curr Opin Biotechnol* **8**, 741–748 (1997).

16. Boomker, J. M., De Leij, L. F. M. H., The, T. H. & Harmsen, M. C. Viral chemokine-modulatory proteins: tools and targets. *Cytokine Growth Factor Rev* **16**, 91–103 (2005).

17. Lalani, A. S. *et al.* The purified myxoma virus gamma interferon receptor homolog M-T7 interacts with the heparin-binding domains of chemokines. *J Virol* **71**, 4356–4363 (1997).

18. Graham, K. A. *et al.* The T1/35kDa family of poxvirus-secreted proteins bind chemokines and modulate leukocyte influx into virus-infected tissues. *Virology* **229**, 12–24 (1997).

19. Stark, L. E., Guan, W., Colvin, M. E. & LiWang, P. J. The binding and specificity of chemokine binding proteins, through the lens of experiment and computation. *Biomed J* **45**, 439–453 (2022).

20. Parry, C. M. *et al.* A broad spectrum secreted chemokine binding protein encoded by a herpesvirus. *J Exp Med* **191**, 573–578 (2000).

21. Carfí, A., Smith, C. A., Smolak, P. J., McGrew, J. & Wiley, D. C. Structure of a soluble secreted chemokine inhibitor vCCI (p35) from cowpox virus. *Proc Natl Acad Sci U S A* **96**, 12379–83 (1999).

22. Zhang, L. *et al.* Solution structure of the complex between poxvirus-encoded CC chemokine inhibitor vCCI and human MIP-1beta. *Proceedings of the National Academy of Sciences* **103**, 13985–13990 (2006).

23. Pereira, R. F. P., Silva, M. M. & De Zea Bermudez, V. Bombyx mori Silk Fibers: An Outstanding Family of Materials. *Macromol Mater Eng* **300**, 1171–1198 (2015).

24. Muffly, T. M., Tizzano, A. P. & Walters, M. D. The history and evolution of sutures in pelvic surgery. *Journal of the Royal Society of Medicine* vol. 104 107–112 Preprint at https://doi.org/10.1258/jrsm.2010.100243 (2011).

25. Holland, C., Numata, K., Rnjak-Kovacina, J. & Seib, F. P. The Biomedical Use of Silk: Past, Present, Future. *Adv Healthc Mater* **8**, 1800465 (2019).

26. Lammel, A. S., Hu, X., Park, S. H., Kaplan, D. L. & Scheibel, T. R. Controlling silk fibroin particle features for drug delivery. *Biomaterials* **31**, 4583–4591 (2010).

27. Ciocci, M., Cacciotti, I., Seliktar, D. & Melino, S. Injectable silk fibroin hydrogels functionalized with microspheres as adult stem cells-carrier systems. *Int J Biol Macromol* **108**, 960–971 (2018).

28. Zhou, Z. *et al.* The Use of Functionalized Silk Fibroin Films as a Platform for Optical Diffraction-Based Sensing Applications. *Advanced Materials* **29**, (2017).

29. Wang, C. *et al.* Carbonized silk fabric for ultrastretchable, highly sensitive, and wearable strain sensors. *Advanced Materials* **28**, 6640–6648 (2016).

30. Xiao, S., Wang, Z., Ma, H., Yang, H. & Xu, W. Effective removal of dyes from aqueous solution using ultrafine silk fibroin powder. *Advanced Powder Technology* **25**, 574–581 (2014).

31. Shao, Z. & Vollrath, F. Surprising strength of silkworm silk. *Nature* **418**, 741 (2002).

32. Asakura, T., Okushita, K. & Williamson, M. P. Analysis of the Structure of Bombyx mori Silk Fibroin by NMR. *Macromolecules* **48**, 2345–2357 (2015).

33. Zhou, C. Z. *et al.* Silk fibroin: Structural implications of a remarkable amino acid sequence. *Proteins: Structure, Function and Genetics* **44**, 119–122 (2001).

34. Inoue, S. *et al.* Silk Fibroin of Bombyx mori Is Secreted, Assembling a High Molecular Mass Elementary Unit Consisting of H-chain, L-chain, and P25, with a 6:6:1 Molar Ratio. *Journal of Biological Chemistry* **275**, 40517–40528 (2000).

35. Zafar, M. S., Belton, D. J., Hanby, B., Kaplan, D. L. & Perry, C. C. Functional Material Features of Bombyx mori Silk Light vs. Heavy Chain Proteins. *Biomacromolecules* **16**, 606 (2015).

36. H, Y., Y, I., Y, T., H, S. & K, T. Identification of fibroin-derived peptides enhancing the proliferation of cultured human skin fibroblasts. *Biomaterials* **25**, 467–472 (2004).

37. Tetsuo Asakura, *,† *et al.* Possible Implications of Serine and Tyrosine Residues and Intermolecular Interactions on the Appearance of Silk I Structure of Bombyx mori Silk Fibroin-Derived Synthetic Peptides: High-Resolution 13C Cross-Polarization/Magic-Angle Spinning NMR Study. *Biomacromolecules* **6**, 468–474 (2004).

38. Murphy, A. R. & Kaplan, D. L. Biomedical applications of chemically-modified silk fibroin. *J Mater Chem* **19**, 6443–6450 (2009).

39. Nguyen, A. T. *et al.* Crystal networks in silk fibrous materials: From hierarchical structure to ultra performance. *Small* vol. 11 1039–1054 Preprint at https://doi.org/10.1002/smll.201402985 (2015).

40. Fu, C., Shao, Z. & Fritz, V. Animal silks: their structures, properties and artificial production. *Chemical Communications* 6515–6529 (2009) doi:10.1039/B911049F.

41. Jin, H.-J. *et al.* Water-Stable Silk Films with Reduced β-Sheet Content. *Adv Funct Mater* **15**, 1241–1247 (2005).

42. Kundu, B. *et al.* Silk proteins for biomedical applications: Bioengineering perspectives. *Prog Polym Sci* **39**, 251–267 (2014).

43. Sofia, S., Mccarthy, M. B., Gronowicz, G. & Kaplan, D. L. Functionalized silk-based biomaterials for bone formation. (2000) doi:10.1002/1097-4636.

44. Sampaio, S., Miranda, T. M. R., Santos, J. G. & Soares, G. M. B. Preparation of silk fibroin–poly(ethylene glycol) conjugate films through click chemistry. *Polym Int* **60**, 1737–1744 (2011).

45. CE, K., JH, L., YK, Y., CH, P. & J, Y. Effects of silk fibroin in murine dry eye. *Sci Rep* **7**, (2017).

46.   W, A.-N. *et al.* Silk-Derived Protein Enhances Corneal Epithelial Migration, Adhesion, and Proliferation. *Invest Ophthalmol Vis Sci* **58**, 1425–1433 (2017).

47.   LJ, B. *et al.* Human corneal epithelial equivalents constructed on Bombyx mori silk fibroin membranes. *Biomaterials* **32**, 5086–5091 (2011).

48.   Ding, Z., Cheng, W., Mia, M. S. & Lu, Q. Silk Biomaterials for Bone Tissue Engineering. *Macromol Biosci* 2100153 (2021) doi:10.1002/MABI.202100153.

49.   Yavuz, B. *et al.* Silk Fibroin Microneedle Patches for the Sustained Release of Levonorgestrel. *ACS Appl Bio Mater* **3**, 5375–5382 (2020).

50.   YQ, Z. *et al.* Synthesis, characterization and immunogenicity of silk fibroin-L-asparaginase bioconjugates. *J Biotechnol* **120**, 315–326 (2005).

51.   Zhang, L. *et al.* Stabilization and Sustained Release of HIV Inhibitors by Encapsulation in Silk Fibroin Disks. *ACS Biomater Sci Eng* **3**, 1654–1665 (2017).

52.   Crakes, K. R. *et al.* Efficacy of silk fibroin biomaterial vehicle for in vivo mucosal delivery of Griffithsin and protection against HIV and SHIV infection ex vivo. *J Int AIDS Soc* **23**, e25628 (2020).

53.   YQ, Z. *et al.* Silk sericin-insulin bioconjugates: synthesis, characterization and biological activity. *J Control Release* **115**, 307–315 (2006).

54.   Guan, W. *et al.* Efficient production of fluorophore-labeled CC chemokines for biophysical studies using recombinant enterokinase and recombinant sortase. *Biopolymers* e23557 (2023) doi:10.1002/BIP.23557.

55.   Nguyen, A. F. *et al.* Biophysical and Computational Studies of the vCCI:vMIP-II Complex. *Int J Mol Sci* **18**, (2017).

56.   Bhusal, R. P., Foster, S. R. & Stone, M. J. Structural basis of chemokine and receptor interactions: Key regulators of leukocyte recruitment in inflammatory responses. *Protein Science* **29**, 420–432 (2020).

57.   Stone, M. J., Hayward, J. A., Huang, C., Huma, Z. E. & Sanchez, J. *Mechanisms of Regulation of the Chemokine-Receptor Network*. *International Journal of Molecular Sciences* vol. 18 (2017).

58.   Laurence, J. S., Blanpain, C., De Leener, A., Parmentier, M. & LiWang, P. J. Importance of basic residues and quaternary structure in the function of MIP-1β: CCR5 binding and cell surface sugar interactions. *Biochemistry* **40**, (2001).

59.   Paavola, C. D. *et al.* Monomeric monocyte chemoattractant protein-1 (MCP-1) binds and activates the MCP-1 receptor CCR2B. *J. Biol. Chem.* **273**, 33157–33165 (1998).

60.   Laurence, J. S., Blanpain, C., Burgner, J. W., Parmentier, M. & LiWang, P. J. CC chemokine MIP-1β can function as a monomer and depends on Phe13 for receptor binding. *Biochemistry* **39**, 3401–3409 (2000).

61. Hemmerich, S. *et al.* Identification of residues in the monocyte chemotactic protein-1 that contact the MCP-1 receptor, CCR2. *Biochemistry* **38**, 13013–13025 (1999).

62. McCornack, M. A., Cassidy, C. K. & LiWang, P. J. The binding surface and affinity of monomeric and dimeric chemokine macrophage inflammatory protein 1β for various glycosaminoglycan disaccharides. *Journal of Biological Chemistry* **278**, (2003).

63. Deshauer, C. *et al.* Interactions of the Chemokine CCL5/RANTES with Medium-Sized Chondroitin Sulfate Ligands. *Structure* **23**, 1066–1077 (2015).

64. Wang, X., Watson, C., Sharp, J. S., Handel, T. M. & Prestegard, J. H. Oligomeric structure of the chemokine CCL5/RANTES from NMR, MS, and SAXS data. *Structure* **19**, 1138–1148 (2011).

65. Lau, E. K. *et al.* Identification of the glycosaminoglycan binding site of the CC chemokine, MCP-1: implications for structure and function in vivo. *Journal of Biological Chemistry* **279**, 22294–22305 (2004).

66. Zheng, Y. *et al.* Structure of CC Chemokine Receptor 5 with a Potent Chemokine Antagonist Reveals Mechanisms of Chemokine Recognition and Molecular Mimicry by HIV. *Immunity* **46**, 1005-1017.e5 (2017).

67. White, G. E., Iqbal, A. J. & Greaves, D. R. CC chemokine receptors and chronic inflammation--therapeutic opportunities and pharmacological challenges. *Pharmacol Rev* **65**, 47–89 (2013).

68. Wells, T. N. C., Power, C. A., Shaw, J. P. & Proudfoot, A. E. I. Chemokine blockers - Therapeutics in the making? *Trends Pharmacol Sci* **27**, 41–47 (2006).

69. Hellewell, S., Semple, B. D. & Morganti-Kossmann, M. C. Therapies negating neuroinflammation after brain trauma. *Brain Res* **1640**, 36–56 (2016).

70. LiWang, A. C., Wang, Z. -x., Sun, Y., Peiper, S. C. & LiWang, P. J. The solution structure of the anti-HIV chemokine vMIP-II. *Protein Science* **8**, 2270–2279 (1999).

71. Kledal, T. N. *et al.* A broad-spectrum chemokine antagonist encoded by Kaposi's Sarcoma-associated herpesvirus. *Science (1979)* **277**, 1656–1659 (1997).

72. Szpakowska, M. & Chevigne, A. vCCL2/vMIP-II, the viral master KEYmokine. *J Leukoc Biol* **99**, 893–900 (2016).

73. Alcami, A. & Lira, S. A. Modulation of chemokine activity by viruses. *Curr Opin Immunol* **22**, 482–487 (2010).

74. Proudfoot, A. E. I., Bonvin, P. & Power, C. A. Targeting chemokines: Pathogens can, why can't we? *Cytokine* **74**, 259–267 (2015).

75. Heidarieh, H., Hernáez, B. & Alcamí, A. Immune modulation by virus-encoded secreted chemokine binding proteins. *Virus Res* **209**, 67–75 (2015).

76. Nelson, C. A., Epperson, M. L., Singh, S., Elliott, J. I. & Fremont, D. H. Structural conservation and functional diversity of the poxvirus immune evasion (PIE) domain superfamily. *Viruses* vol. 7 4878–4903 Preprint at https://doi.org/10.3390/v7092848 (2015).

77. González-Motos, V., Kropp, K. A. & Viejo-Borbolla, A. Chemokine binding proteins: An immunomodulatory strategy going viral. *Cytokine Growth Factor Rev* **30**, 71–80 (2016).

78. Hayward, J. *et al.* Ticks from diverse genera encode chemokine-inhibitory evasin proteins. *Journal of Biological Chemistry* **292**, 15670–15680 (2017).

79. Yaron, J. R. *et al.* Deriving Immune Modulating Drugs from Viruses—A New Class of Biologics. *J Clin Med* **9**, 972 (2020).

80. Buatois, V. *et al.* Pan-CC chemokine neutralization restricts splenocyte egress and reduces inflammation in a model of arthritis. *J Immunol* **185**, 2544–2554 (2010).

81. Ali, Z. A. *et al.* Gene transfer of a broad spectrum CC-chemokine inhibitor reduces vein graft atherosclerosis in apolipoprotein E-knockout mice. *Circulation* **112**, 235–241 (2005).

82. Bursill, C. A. *et al.* Lentiviral gene transfer to reduce atherosclerosis progression by long-term CC-chemokine inhibition. *Gene Ther* **16**, 93–102 (2009).

83. Bursill, C. A., Choudhury, R. P., Ali, Z., Greaves, D. R. & Channon, K. M. Broad-spectrum CC-chemokine blockade by gene transfer inhibits macrophage recruitment and atherosclerotic plaque formation in apolipoprotein E-knockout mice. *Circulation* **110**, 2460–2466 (2004).

84. Alcami, A., Symons, J. A., Collins, P. D., Williams, T. J. & Smith, G. L. Blockade of chemokine activity by a soluble chemokine binding protein from vaccinia virus. *Journal of Immunology* **160**, 624–633 (1998).

85. Dabbagh, K. *et al.* Local blockade of allergic airway hyperreactivity and inflammation by the poxvirus-derived pan-CC-chemokine inhibitor vCCI. *Journal of Immunology* **165**, 3418–3422 (2000).

86. Zhang, L. *et al.* Solution structure of the complex between poxvirus-encoded CC chemokine inhibitor vCCI and human MIP-1beta. *Proc Natl Acad Sci U S A.* **103**, 13985–13990 (2006).

87. Arnold, P. L. & Fremont, D. H. Structural Determinants of Chemokine Binding by an Ectromelia Virus-Encoded Decoy Receptor. *J Virol* **80**, 7439–7449 (2006).

88. Carfi, A. *et al.* Structure of a soluble secreted chemokine inhibitor vCCI (p35) from cowpox virus. *Proc. Natl. Acad. Sci. USA* **96**, 12379–12383 (1999).

89. White, G. E., Mcneill, E., Christou, I., Channon, K. M. & Greaves, D. R. Site-Directed Mutagenesis of the CC Chemokine Binding Protein 35K-Fc Reveals Residues Essential for Activity and Mutations That Increase the Potency of CC Chemokine Blockade. *Mol Pharmacol* **80**, 328–336 (2011).

90. Bahar, M. W. *et al.* Structure and Function of A41 , a Vaccinia Virus Chemokine Binding Protein. **4**, (2008).

91. Sharif, S. *et al.* A broad-spectrum chemokine-binding protein of bovine papular stomatitis virus inhibits neutrophil and monocyte infiltration in inflammatory and wound models of mouse skin. *PLoS One* **11**, 1–22 (2016).

92. Lee, S. *et al.* Effect of a broad-specificity chemokine-binding protein on brain leukocyte infiltration and infarct development. *Stroke* **46**, 537–544 (2015).

93. Couñago, R. M. *et al.* Structures of Orf Virus Chemokine Binding Protein in Complex with Host Chemokines Reveal Clues to Broad Binding Specificity. *Structure* **23**, 1199–1213 (2015).

94. Alejo, A., Sánchez, C., Amu, S., Fallon, P. G. & Alcamí, A. Addition of a Viral Immunomodulatory Domain to Etanercept Generates a Bifunctional Chemokine and TNF Inhibitor. *J Clin Med* **9**, 25 (2019).

95. Viejo-Borbolla, A. *et al.* Attenuation of TNF-driven murine ileitis by intestinal expression of the viral immunomodulator CrmD. *Mucosal Immunol* (2010) doi:10.1038/mi.2010.40.

96. Xue, X. *et al.* Structural basis of chemokine sequestration by CrmD, a poxvirus-encoded tumor necrosis factor receptor. *PLoS Pathog* **7**, (2011).

97. Alejo, A. *et al.* A chemokine-binding domain in the tumor necrosis factor receptor from variola (smallpox) virus. *Proc Natl Acad Sci U S A* **103**, 5995–6000 (2006).

98. Millward, J. M. *et al.* The murine gammaherpesvirus-68 chemokine-binding protein M3 inhibits experimental autoimmune encephalomyelitis. *J Neuroimmunol* **224**, 45–50 (2010).

99. Martin, A. P. *et al.* The Chemokine Binding Protein M3 Prevents Diabetes Induced by Multiple Low Doses of Streptozotocin. *The Journal of Immunology* **178**, 4623–4631 (2007).

100. Alexander, J. M. *et al.* Structural basis of chemokine sequestration by a herpesvirus decoy receptor. *Cell* **111**, 343–356 (2002).

101. Alexander-Brett, J. M. & Fremont, D. H. Dual GPCR and GAG mimicry by the M3 chemokine decoy receptor. *Journal of Experimental Medicine* **204**, 3157–3172 (2007).

102. Lubman, O. Y. & Fremont, D. H. Parallel Evolution of Chemokine Binding by Structurally Related Herpesvirus Decoy Receptors. *Structure* **24**, 57–69 (2016).

103. Montecucco, F. *et al.* Treatment with Evasin-3 abrogates neutrophil-mediated inflammation in mouse acute pancreatitis. *Eur J Clin Invest* **44**, 940–950 (2014).

104. Vieira, A. T. *et al.* Treatment with a novel chemokine-binding protein or eosinophil lineage-ablation protects mice from experimental colitis. *American Journal of Pathology* **175**, 2382–2391 (2009).

105. Dias, J. M. *et al.* Structural basis of chemokine sequestration by a tick chemokine binding protein: The crystal structure of the complex between Evasin-1 and CCL3. *PLoS One* **4**, (2009).

106. Bonvin, P. *et al.* Identification of the pharmacophore of the CC chemokine-binding proteins evasin-1 and -4 using phage display. *Journal of Biological Chemistry* **289**, 31846–31855 (2014).

107. Franck, C. *et al.* Semisynthesis of an evasin from tick saliva reveals a critical role of tyrosine sulfation for chemokine binding and inhibition. *Proc Natl Acad Sci U S A* **117**, 12657–12664 (2020).

108. Déruaz, M. *et al.* Ticks produce highly selective chemokine binding proteins with antiinflammatory activity. *Journal of Experimental Medicine* **205**, 2019–2031 (2008).

109. Lee, A. W. *et al.* A knottin scaffold directs the CXC-chemokine-binding specificity of tick evasins. *Journal of Biological Chemistry* **294**, 11199–11212 (2019).

110. Liu, L. *et al.* Viral chemokine-binding proteins inhibit inflammatory responses and aortic allograft transplant vasculopathy in rat models. *Transplantation* **77**, 1652–1660 (2004).

111. Liu, L. *et al.* The vital anti-inflammatory chemokine-binding protein M-T7 reduces intimal hyperplasia after vascular injury. *Journal of Clinical Investigation* **105**, 1613–1621 (2000).

112. Lalani, A. S. *et al.* Functional comparisons among members of the poxvirus T1/35kDa family of soluble CC-chemokine inhibitor glycoproteins. *Virology* **250**, 173–184 (1998).

113. Seet, B. T. *et al.* Glycosaminoglycan Binding Properties of the Myxoma Virus CC-chemokine Inhibitor, M-T1. *Journal of Biological Chemistry* **276**, 30504–30513 (2001).

114. Lalani, A. S. *et al.* The purified myxoma virus gamma interferon receptor homolog M-T7 interacts with the heparin-binding domains of chemokines. *J Virol* **71**, 4356–4363 (1997).

115. Burns, J. M., Dairaghi, D. J., Deitz, M., Tsang, M. & Schall, T. J. Comprehensive mapping of poxvirus vCCI chemokine-binding protein. Expanded range of ligand interactions and unusual dissociation kinetics. *Journal of Biological Chemistry* **277**, 2785–2789 (2002).

116. Kuo, N.-W. *et al.* Structural insights into the interaction between a potent anti-inflammatory protein, viral CC chemokine inhibitor (vCCI), and the human CC chemokine, eotaxin-1. *Journal of Biological Chemistry* **289**, (2014).

117. Watanabe, Y., Bowden, T. A., Wilson, I. A. & Crispin, M. Exploitation of glycosylation in enveloped virus pathobiology. *Biochim Biophys Acta Gen Subj* **1863**, 1480 (2019).

118. Stark, L. E. Evaluating Protein-Protein Interactions in Chemokine-Inhibitor Complexes Through MD Simulation. (University of California, Merced, 2021).

119. Seet, B. T. *et al.* Molecular determinants for CC-chemokine recognition by a poxvirus CC-chemokine inhibitor. *Proc Natl Acad Sci. USA* **98**, 9008–9013 (2001).

120. Beck, C. G. *et al.* The viral CC chemokine-binding protein vCCI inhibits monocyte chemoattractant protein-1 activity by masking its CCR2B-binding site. *Journal of Biological Chemistry* **276**, 43270–43276 (2001).

121. Ziarek, J. J., Heroux, M. S., Veldkamp, C. T., Peterson, F. C. & Volkman, B. F. Sulfotyrosine recognition as marker for druggable sites in the extracellular space. *Int J Mol Sci* **12**, 3740–3756 (2011).

122. Stark, L. E., LiWang, P. & Colvin, M. E. Determining Factors that Influence vCCI Loop Interactions in vCCI-Chemokine Binding through MD Simulation. *Biophys J* (2020) doi:10.1016/j.bpj.2019.11.2792.

123. Stark, L. E., LiWang, P. J. & Colvin, M. E. Evaluating Protein - Protein Interactions in Chemokine - Inhibitor Complexes using MD Simulation. *Biophys J* (2018) doi:10.1016/j.bpj.2017.11.394.

124. LiWang, P., Guan, W., Stark, L., Showalter, L. & Colvin, M. vCCI:Chemokine Interactions: Experimental Biochemistry Meets Computational Prediction. *The FASEB Journal* (2020) doi:10.1096/fasebj.2020.34.s1.07398.

125. Nguyen, A. F. *et al.* Biophysical and computational studies of the vCCI:VMIP-II complex. *Int J Mol Sci* **18**, (2017).

126. Saeki, H. & Tamaki, K. Thymus and activation regulated chemokine (TARC)/CCL17 and skin diseases. *J Dermatol Sci* **43**, 75–84 (2006).

127. Hansel, T. T. *et al.* A Comprehensive Evaluation of Nasal and Bronchial Cytokines and Chemokines Following Experimental Rhinovirus Infection in Allergic Asthma: Increased Interferons (IFN-γ and IFN-λ) and Type 2 Inflammation (IL-5 and IL-13). *EBioMedicine* **19**, 128–138 (2017).

128. Roumpeka, D. D., Wallace, R. J., Escalettes, F., Fotheringham, I. & Watson, M. A review of bioinformatics tools for bio-prospecting from metagenomic sequence data. *Front Genet* **8**, 1–10 (2017).

129. Zhong, S., Macias, A. & MacKerell, A. Computational Identification of Inhibitors of Protein-Protein Interactions. *Curr Top Med Chem* **7**, 63–82 (2006).

130. Dror, R. O., Dirks, R. M., Grossman, J. P., Xu, H. & Shaw, D. E. Biomolecular simulation: A computational microscope for molecular biology. *Annu Rev Biophys* **41**, 429–452 (2012).

131. Frenkel, D. & Smit, B. *Understanding Molecular Simulation, Second Edition: From Algorithms to Applications (Computational Science)*. *Book* (2001).

132. Dill, K. A. & MacCallum, J. L. The Protein-Folding Problem, 50 Years On. *Science (1979)* **338**, 1042–1046 (2012).

133. Perez, A., Morrone, J. A., Simmerling, C. & Dill, K. A. Advances in free-energy-based simulations of protein folding and ligand binding. *Curr Opin Struct Biol* **36**, 25–31 (2016).

134. Shaw, D. E. *et al.* Atomic-Level Characterization of the Structural Dynamics of Proteins. *Science (1979)* **330**, 341–347 (2010).

135. Kufareva, I. Chemokines and their receptors: insights from molecular modeling and crystallography. *Curr Opin Pharmacol* **30**, 27–37 (2016).

136. Siebenmorgen, T. & Zacharias, M. Computational prediction of protein–protein binding affinities. *Wiley Interdiscip Rev Comput Mol Sci* **10**, 1–18 (2020).

137. Hansen, N. & Van Gunsteren, W. F. Practical aspects of free-energy calculations: A review. *J Chem Theory Comput* **10**, 2632–2647 (2014).

138. He, X. *et al.* Fast, Accurate, and Reliable Protocols for Routine Calculations of Protein-Ligand Binding Affinities in Drug Design Projects Using AMBER GPU-TI with ff14SB/GAFF. *ACS Omega* **5**, 4611–4619 (2020).

139. Wang, L. *et al.* Accurate and reliable prediction of relative ligand binding potency in prospective drug discovery by way of a modern free-energy calculation protocol and force field. *J Am Chem Soc* **137**, 2695–2703 (2015).

140. Clark, A. J. *et al.* Free Energy Perturbation Calculation of Relative Binding Free Energy between Broadly Neutralizing Antibodies and the gp120 Glycoprotein of HIV-1. *J Mol Biol* **429**, 930–947 (2017).

141. Donovan-Maiye, R. M., Langmead, C. J. & Zuckerman, D. M. Systematic Testing of Belief-Propagation Estimates for Absolute Free Energies in Atomistic Peptides and Proteins. *J Chem Theory Comput* **14**, 426–443 (2018).

142. Geng, C., Xue, L. C., Roel-Touris, J. & Bonvin, A. M. J. J. Finding the ΔΔG spot: Are predictors of binding affinity changes upon mutations in protein–protein interactions ready for it? *Wiley Interdiscip Rev Comput Mol Sci* **9**, 1–14 (2019).

143. Lodi, P. J. *et al.* High-resolution solution structure of the β chemokine hMIP-1β by multidimensional NMR. *Science (1979)* **263**, 1762–1767 (1994).

144. Clore, G. M., Gronenborn, A. M., Appella, E., Yamada, M. & Matsushima, K. Three-Dimensional Structure of Interleukin 8 in Solution. *Biochemistry* **29**, 1689–1696 (1990).

145. Bhusal, R. P., Foster, S. R. & Stone, M. J. Structural basis of chemokine and receptor interactions: Key regulators of leukocyte recruitment in inflammatory responses. *Protein Science* **29**, 420–432 (2020).

146. Charo, I. F. & Ransohoff, R. M. The many roles of chemokines and chemokine receptors in inflammation. *N Engl J Med* **354**, 610–621 (2006).

147. Dragic, T. *et al.* HIV-1 entry into CD4+ cells is mediated by the chemokine receptor CC-CKR-5. *Nature* **381**, 667–673 (1996).

148. Zhao, B., Mankowski, M. K., Snyder, B. A., Ptak, R. G. & LiWang, P. J. Highly potent chimeric inhibitors targeting two steps of HIV cell entry. *Journal of Biological Chemistry* **286**, 28370–28381 (2011).

149. Gaertner, H. *et al.* Highly potent, fully recombinant anti-HIV chemokines: reengineering a low-cost microbicide. *Proc Natl Acad Sci U S A* **105**, 17706–17711 (2008).

150. Hartley, O. *et al.* Human Immunodeficiency Virus Type 1 Entry Inhibitors Selected on Living Cells from a Library of Phage Chemokines. *J Virol* **77**, 6637 (2003).

151. Proudfoot, A. E. I. Chemokine receptors: multifaceted therapeutic targets. *Nat Rev Immunol* **2**, 106–115 (2002).

152. Hsieh, C. L. *et al.* CCR2 deficiency impairs macrophage infiltration and improves cognitive function after traumatic brain injury. *J Neurotrauma* **31**, 1677–1688 (2014).

153. Joy, M. T. *et al.* CCR5 Is a Therapeutic Target for Recovery after Stroke and Traumatic Brain Injury. *Cell* **176**, 1143-1157.e13 (2019).

154. Zhao, B. & Liwang, P. J. Characterization of the interactions of vMIP-II, and a dimeric variant of vMIP-II, with glycosaminoglycans. *Biochemistry* **49**, 7012–7022 (2010).

155. LiWang, A. C., Wang, Z. -x., Sun, Y., Peiper, S. C. & LiWang, P. J. The solution structure of the anti-HIV chemokine vMIP-II. *Protein Science* **8**, 2270–2279 (1999).

156. Handel, T. M. & Domaille, P. J. Heteronuclear (1H, 13C, 15N) NMR assignments and solution structure of the monocyte chemoattractant protein-1 (MCP-1) dimer. *Biochemistry* **35**, 6569–6584 (1996).

157. Burns, J. M., Dairaghi, D. J., Deitz, M., Tsang, M. & Schall, T. J. Comprehensive mapping of poxvirus vCCI chemokine-binding protein. Expanded range of ligand interactions and unusual dissociation kinetics. *Journal of Biological Chemistry* **277**, 2785–2789 (2002).

158. Kuo, N. W. *et al.* Structural insights into the interaction between a potent anti-inflammatory protein, viral CC chemokine inhibitor (vCCI), and the human CC chemokine, eotaxin-1. *Journal of Biological Chemistry* **289**, 6592–6603 (2014).

159. Bursill, C. A., Choudhury, R. P., Ali, Z., Greaves, D. R. & Channon, K. M. Broad-spectrum CC-chemokine blockade by gene transfer inhibits macrophage recruitment and atherosclerotic plaque formation in apolipoprotein E-knockout mice. *Circulation* **110**, 2460–2466 (2004).

160. Buatois, V. *et al.* Pan-CC chemokine neutralization restricts splenocyte egress and reduces inflammation in a model of arthritis. *J Immunol* **185**, 2544–2554 (2010).

161. Ridiandries, A., Bursill, C. & Tan, J. Broad-Spectrum Inhibition of the CC-Chemokine Class Improves Wound Healing and Wound Angiogenesis. *International Journal of Molecular Sciences 2017, Vol. 18, Page 155* **18**, 155 (2017).

162. Nguyen, A. F., Schill, M. S., Jian, M. & LiWang, P. J. The effect of N-terminal cyclization on the function of the HIV entry inhibitor 5P12-RANTES. *Int J Mol Sci* **18**, (2017).

163. Laurence, J. S., Blanpain, C., Burgner, J. W., Parmentier, M. & LiWang, P. J. CC chemokine MIP-1 beta can function as a monomer and depends on Phe13 for receptor binding. *Biochemistry* **39**, 3401–3409 (2000).

164. Proudfoot, A. E. I. *et al.* Extension of recombinant human RANTES by the retention of the initiating methionine produces a potent antagonist. *J Biol Chem* **271**, 2599–2603 (1996).

165. Rico, C. A. *et al.* High-Affinity Binding of Chemokine Analogs that Display Ligand Bias at the HIV-1 Coreceptor CCR5. *Biophys J* **117**, 903–919 (2019).

166. Shirakawa, K., Chavez, L., Hakre, S., Calvanese, V. & Verdin, E. Reactivation of latent HIV by histone deacetylase inhibitors. *Trends Microbiol* **21**, 277–285 (2013).

167. Hashemi, P. *et al.* Compounds producing an effective combinatorial regimen for disruption of HIV-1 latency. *EMBO Mol Med* e201708193 (2017) doi:10.15252/emmm.201708193.

168. Sadowski, I. & Hashemi, F. B. Strategies to eradicate HIV from infected patients: elimination of latent provirus reservoirs. *Cellular and Molecular Life Sciences* vol. 76 3583–3600 Preprint at https://doi.org/10.1007/s00018-019-03156-8 (2019).

169. Schwartz, C. *et al.* On the way to find a cure: Purging latent HIV-1 reservoirs. *Biochemical Pharmacology* (2017) doi:10.1016/j.bcp.2017.07.001.

170. Elsheikh, M. M., Tang, Y., Li, D. & Jiang, G. Deep latency: A new insight into a functional HIV cure. *EBioMedicine* vol. 45 624–629 Preprint at https://doi.org/10.1016/j.ebiom.2019.06.020 (2019).

171. Deeks, S. G. HIV: Shock and kill. *Nature* **487**, 439–440 (2012).

172. Darcis, G., Van Driessche, B. & Van Lint, C. HIV Latency: Should We Shock or Lock? *Trends Immunol* **38**, 217–228 (2017).

173. Méndez, C., Ledger, S., Petoumenos, K., Ahlenstiel, C. & Kelleher, A. D. RNA-induced epigenetic silencing inhibits HIV-1 reactivation from latency. *Retrovirology* **15**, (2018).

174. Kessing, C. F. *et al.* In Vivo Suppression of HIV Rebound by Didehydro-Cortistatin A, a "Block-and-Lock" Strategy for HIV-1 Treatment. *Cell Rep* **21**, 600–611 (2017).

175. Sloan, D. D. *et al.* Targeting HIV Reservoir in Infected CD4 T Cells by Dual-Affinity Re-targeting Molecules (DARTs) that Bind HIV Envelope and Recruit Cytotoxic T Cells. *PLoS Pathog* **11**, (2015).

176. Delannoy, A., Poirier, M. & Bell, B. Cat and mouse: HIV transcription in latency, immune evasion and cure/remission strategies. *Viruses* vol. 11 Preprint at https://doi.org/10.3390/v11030269 (2019).

177. Marsden, M. D. & Zack, J. A. HIV cure strategies: A complex approach for a complicated viral reservoir? *Future Virology* vol. 14 5–8 Preprint at https://doi.org/10.2217/fvl-2018-0205 (2019).

178. Debyser, Z., Vansant, G., Bruggemans, A., Janssens, J. & Christ, F. Insight in HIV Integration Site Selection Provides a Block-and-Lock Strategy for a Functional Cure of HIV Infection. *Viruses* **11**, 12 (2018).

179. Vanhamel, J., Bruggemans, A. & Debyser, Z. Establishment of latent HIV-1 reservoirs: what do we really know? *J Virus Erad* **5**, 3–9 (2019).

180. Yin, C. *et al.* In Vivo Excision of HIV-1 Provirus by saCas9 and Multiplex Single-Guide RNAs in Animal Models. *Molecular Therapy* **25**, 1168–1186 (2017).

181. Limsirichai, P., Gaj, T. & Schaffer, D. V. CRISPR-mediated Activation of Latent HIV-1 Expression. *Molecular Therapy* **24**, 499–507 (2016).

182. Silas, S. *et al.* Direct CRISPR spacer acquisition from RNA by a natural reverse transcriptase-Cas1 fusion protein. *Science (1979)* **351**, aad4234–aad4234 (2016).

183. Amsterdam, D. Unique natural and adaptive response mechanisms to control and eradicate HIV infection. *AIMS Allergy Immunol* **2**, 113–125 (2018).

184. Henderson, L. J., Reoma, L. B., Kovacs, J. A. & Nath, A. Advances toward Curing HIV-1 Infection in Tissue Reservoirs. *J Virol* **94**, (2019).

185. Wang, H., La Russa, M. & Qi, L. S. CRISPR/Cas9 in Genome Editing and Beyond. *Annu Rev Biochem* **85**, 227–264 (2016).

186. Pegu, A. *et al.* Activation and lysis of human CD4 cells latently infected with HIV-1. *Nat Commun* **6**, 8447 (2015).

187. Spina, C. A. *et al.* An In-Depth Comparison of Latent HIV-1 Reactivation in Multiple Cell Model Systems and Resting CD4+ T Cells from Aviremic Patients. *PLoS Pathog* **9**, 1–15 (2013).

188. Li, C., Mousseau, G. & Valente, S. T. Tat inhibition by didehydro-Cortistatin A promotes heterochromatin formation at the HIV-1 long terminal repeat. *Epigenetics Chromatin* **12**, 23 (2019).

189. Kumar, N., Chahroudi, A. & Silvestri, G. Animal models to achieve an HIV cure. *Current Opinion in HIV and AIDS* vol. 11 432–441 Preprint at https://doi.org/10.1097/COH.0000000000000290 (2016).

190. Takata, H. *et al.* Modeling HIV-1 Latency Using Primary CD4 + T Cells from Virally Suppressed HIV-1-Infected Individuals on Antiretroviral Therapy . *J Virol* **93**, (2019).

191. Flemming, A. Shocking HIV out of hiding. *Nature Reviews Immunology* vol. 20 138–139 Preprint at https://doi.org/10.1038/s41577-020-0283-8 (2020).

192. Llewellyn, G. N. *et al.* Humanized Mouse Model of HIV-1 Latency with Enrichment of Latent Virus in PD-1 + and TIGIT + CD4 T Cells . *J Virol* **93**, (2019).

193. Nixon, C. C. *et al.* Systemic HIV and SIV latency reversal via non-canonical NF-κB signalling in vivo. *Nature* **578**, 160–165 (2020).

194. McBrien, J. B. *et al.* Robust and persistent reactivation of SIV and HIV by N-803 and depletion of CD8+ cells. *Nature* **578**, 154–159 (2020).

195. Van Praag, R. M. E. *et al.* OKT3 and IL-2 treatment for purging of the latent HIV-1 reservoir in vivo results in selective long-lasting CD4+ T cell depletion. *J Clin Immunol* **21**, 218–226 (2001).

196. Gama, L. *et al.* Reactivation of simian immunodeficiency virus reservoirs in the brain of virally suppressed macaques. *AIDS* **31**, 5–14 (2017).

197. Knights, H. D. J. A Critical Review of the Evidence Concerning the HIV Latency Reversing Effect of Disulfiram, the Possible Explanations for Its Inability to Reduce the Size of the Latent Reservoir In Vivo, and the Caveats Associated with Its Use in Practice. *AIDS Res Treat* **2017**, 8239428 (2017).

198. Kim, Y., Anderson, J. L. & Lewin, S. R. Getting the "Kill" into "Shock and Kill": Strategies to Eliminate Latent HIV. *Cell Host and Microbe* vol. 23 14–26 Preprint at https://doi.org/10.1016/j.chom.2017.12.004 (2018).

199. Bouchat, S. *et al.* Histone methyltransferase inhibitors induce HIV-1 recovery in resting CD4+ T cells from HIV-1-infected HAART-treated patients. *AIDS* **26**, 1473–1482 (2012).

200. Macedo, A. B., Novis, C. L. & Bosque, A. Targeting Cellular and Tissue HIV Reservoirs With Toll-Like Receptor Agonists. *Frontiers in Immunology* vol. 10 2450 Preprint at https://doi.org/10.3389/fimmu.2019.02450 (2019).

201. Tsai, A. *et al.* Toll-Like Receptor 7 Agonist GS-9620 Induces HIV Expression and HIV-Specific Immunity in Cells from HIV-Infected Individuals on Suppressive Antiretroviral Therapy. *J Virol* **91**, (2017).

202. Appleman, J. R. & Webber, S. E. Discovery of a novel Toll-like Receptor 7 agonist for systemic immunotherapy of cancer. *Journal of Clinical Oncology* **37**, e14246–e14246 (2019).

203. Chi, H. *et al.* Anti-tumor activity of toll-like receptor 7 agonists. *Frontiers in Pharmacology* vol. 8 Preprint at https://doi.org/10.3389/fphar.2017.00304 (2017).

204. Macedo, A. B. *et al.* Dual TLR2 and TLR7 agonists as HIV latency-reversing agents. *JCI Insight* **3**, (2018).

205. Perreau, M., Banga, R. & Pantaleo, G. Targeted Immune Interventions for an HIV-1 Cure. *Trends Mol Med* **23**, 945–961 (2017).

206. Archin, N. M. *et al.* Interval dosing with the HDAC inhibitor vorinostat effectively reverses HIV latency. *Journal of Clinical Investigation* **127**, 3126–3135 (2017).

207. Margolis, D. M. Histone deacetylase inhibitors and HIV latency. *Curr Opin HIV AIDS* **6**, 25–29 (2011).

208. Beliakova-Bethell, N. *et al.* Histone deacetylase inhibitors induce complex host responses that contribute to differential potencies of these compounds in HIV reactivation. *Journal of Biological Chemistry* **294**, 5576–5589 (2019).

209. Zaikos, T. D., Painter, M. M., Sebastian Kettinger, N. T., Terry, V. H. & Collins, K. L. Class 1-Selective Histone Deacetylase (HDAC) Inhibitors Enhance HIV Latency Reversal while Preserving the Activity of HDAC Isoforms Necessary for Maximal HIV Gene Expression. *J Virol* **92**, (2018).

210. Chan, J. K. L. & Greene, W. C. NF-κB/Rel: Agonist and antagonist roles in HIV-1 latency. *Curr Opin HIV AIDS* **6**, 12–18 (2011).

211. An, W. Histone acetylation and methylation: combinatorial players for transcriptional regulation. *Subcell Biochem* **41**, 351–69 (2007).

212. Gilmore, T. D. Introduction to NF-κB: players, pathways, perspectives. *Oncogene* **25**, 6680–6684 (2006).

213. Ott, M., Geyer, M. & Zhou, Q. The control of HIV transcription: Keeping RNA polymerase II on track. *Cell Host Microbe* **10**, 426–435 (2011).

214. Bayer, P. *et al.* Structural studies of HIV-1 Tat protein. *J Mol Biol* **247**, 529–35 (1995).

215. Bigalke, J. M. *et al.* Formation of Tatâ€"TAR containing ribonucleoprotein complexes for biochemical and structural analyses. (2011) doi:10.1016/j.ymeth.2010.04.001.

216. Gu, J. *et al.* Crystal structure of HIV-1 Tat complexed with human P-TEFb and AFF4. *Cell Cycle* **13**, 1788–1797 (2014).

217. Gatignol, A. Transcription of HIV: Tat and Cellular Chromatin. *Advances in Pharmacology* vol. 55 137–159 Preprint at https://doi.org/10.1016/S1054-3589(07)55004-0 (2007).

218. Easley, R. *et al.* Chromatin dynamics associated with HIV-1 Tat-activated transcription. *Biochimica et Biophysica Acta - Gene Regulatory Mechanisms* vol. 1799 275–285 Preprint at https://doi.org/10.1016/j.bbagrm.2009.08.008 (2010).

219. Siddappa, N. B. *et al.* Transactivation and signaling functions of Tat are not correlated: biological and immunological characterization of HIV-1 subtype-C Tat protein. *Retrovirology* **3**, 53 (2006).

220. Jeang, K. T., Xiao, H. & Rich, E. A. Multifaceted activities of the HIV-1 transactivator of transcription, Tat. *Journal of Biological Chemistry* **274**, 28837–28840 (1999).

221. Rice, A. P. The HIV-1 Tat Protein: Mechanism of Action and Target for HIV-1 Cure Strategies. *Curr Pharm Des* **23**, 4098 (2017).

222. Romani, B., Engelbrecht, S. & Glashoff, R. H. Functions of Tat: The versatile protein of human immunodeficiency virus type 1. *Journal of General Virology* vol. 91 1–12 Preprint at https://doi.org/10.1099/vir.0.016303-0 (2010).

223. Das, A. T., Harwig, A. & Berkhout, B. The HIV-1 Tat Protein Has a Versatile Role in Activating Viral Transcription. *J Virol* **85**, 9506–9516 (2011).

224. Burnett, J. C., Miller-Jensen, K., Shah, P. S., Arkin, A. P. & Schaffer, D. V. Control of stochastic gene expression by host factors at the HIV promoter. *PLoS Pathog* **5**, (2009).

225. Cary, D. C., Fujinaga, K. & Peterlin, B. M. Molecular mechanisms of HIV latency. *Journal of Clinical Investigation* vol. 126 448–454 Preprint at https://doi.org/10.1172/JCI80565 (2016).

226. Donahue, D. A., Kuhl, B. D., Sloan, R. D. & Wainberg, M. A. The Viral Protein Tat Can Inhibit the Establishment of HIV-1 Latency. *J Virol* **86**, 3253–3263 (2012).

227. Geng, G. *et al.* Development of an attenuated tat protein as a highly-effective agent to specifically activate HIV-1 latency. *Molecular Therapy* **24**, 1528–1537 (2016).

228. Kamori, D. & Ueno, T. HIV-1 tat and viral latency: What we can learn from naturally occurring sequence variations. *Frontiers in Microbiology* vol. 8 Preprint at https://doi.org/10.3389/fmicb.2017.00080 (2017).

229. Khoury, G. *et al.* HIV latency reversing agents act through Tat post translational modifications. *Retrovirology* **15**, (2018).

230. Mousseau, G. *et al.* The tat inhibitor didehydro-cortistatin a prevents HIV-1 reactivation from latency. *mBio* **6**, (2015).

231. Mousseau, G. *et al.* Resistance to the Tat Inhibitor Didehydro-Cortistatin A Is Mediated by Heightened Basal HIV-1 Transcription. *mBio* **10**, (2019).

232. Donahue, D. A., Kuhl, B. D., Sloan, R. D. & Wainberg, M. A. The Viral Protein Tat Can Inhibit the Establishment of HIV-1 Latency. *J Virol* **86**, 3253–3263 (2012).

233. Tang, X. *et al.* Exosomal Tat protein activates latent HIV-1 in primary, resting CD4+ T lymphocytes. *JCI Insight* **3**, (2018).

234. Donahue, D. A., Bastarache, S. M., Sloan, R. D. & Wainberg, M. A. Latent HIV-1 can be reactivated by cellular superinfection in a Tat-dependent manner, which can lead to the emergence of multidrug-resistant recombinant viruses. *J Virol* **87**, 9620–32 (2013).

235. Razooky, B. S., Pai, A., Aull, K., Rouzine, I. M. & Weinberger, L. S. A hardwired HIV latency program. *Cell* **160**, 990–1001 (2015).

236. Bagashev, A. & Sawaya, B. E. Roles and functions of HIV-1 Tat protein in the CNS: an overview. *Virol J* **10**, 358 (2013).

237. King, J. E., Eugenin, E. A., Buckner, C. M. & Berman, J. W. HIV tat and neurotoxicity. *Microbes and Infection* vol. 8 1347–1357 Preprint at https://doi.org/10.1016/j.micinf.2005.11.014 (2006).

238. Rajalingam, D., Loftis, C., Xu, J. J. & Kumar, T. K. S. Trichloroacetic acid-induced protein precipitation involves the reversible association of a stable partially structured intermediate. *Protein Science* **18**, 980–993 (2009).

239. Wiederschain, G. Ya. The proteomics protocols handbook. *Biochemistry (Moscow)* **71**, 696–696 (2006).

240. Chang, Y. G., Tseng, R., Kuo, N. W. & LiWang, A. Rhythmic ring-ring stacking drives the circadian oscillator clockwise. *Proc Natl Acad Sci U S A* **109**, 16847–16851 (2012).

241. Piper, I. M. *et al.* Sequence variation in the β7-β8 loop of bacterial class A sortase enzymes alters substrate selectivity. *Journal of Biological Chemistry* **297**, (2021).

242. Simeonov, P., Berger-Hoffmann, R., Hoffmann, R., Sträter, N. & Zuchner, T. Surface supercharged human enteropeptidase light chain shows improved solubility and refolding yield. *Protein Engineering, Design and Selection* **24**, 261–268 (2011).

243. Gasparian, M. E., Ostapchenko, V. G., Dolgikh, D. A. & Kirpichnikov, M. P. Biochemical characterization of human enteropeptidase light chain. *Biochemistry (Mosc)* **71**, 113–119 (2006).

244. Skala, W., Goettig, P. & Brandstetter, H. Do-it-yourself histidine-tagged bovine enterokinase: A handy member of the protein engineer's toolbox. *J Biotechnol* **168**, 421–425 (2013).

245. Gasparian, M. E., Ostapchenko, V. G., Schulga, A. A., Dolgikh, D. A. & Kirpichnikov, M. P. Expression, purification, and characterization of human enteropeptidase catalytic subunit in Escherichia coli. *Protein Expr Purif* **31**, 133–139 (2003).

246. Pepeliaev, S. *et al.* High level expression of human enteropeptidase light chain in Pichia pastoris. *J Biotechnol* **156**, 67–75 (2011).

247. Kouokam, J. C. *et al.* Investigation of Griffithsin's Interactions with Human Cells Confirms Its Outstanding Safety and Efficacy Profile as a Microbicide Candidate. *PLoS One* **6**, e22635 (2011).

248. Popp, M. W. L., Antos, J. M. & Ploegh, H. L. Site-Specific Protein Labeling via Sortase-Mediated Transpeptidation. *Curr Protoc Protein Sci* **56**, 15.3.1-15.3.9 (2009).

249. Pasqual, G. *et al.* Monitoring T cell-dendritic cell interactions in vivo by intercellular enzymatic labelling. *Nature* **553**, 496–500 (2018).

250. Antos, J. M. *et al.* Site-specific N- and C-terminal labeling of a single polypeptide using sortases of different specificity. *J Am Chem Soc* **131**, 10800–10801 (2009).

251. Antos, J. M. *et al.* A Straight Path to Circular Proteins. *J Biol Chem* **284**, 16028 (2009).

252. Catherine, J. & Roufosse, F. What does elevated TARC/CCL17 expression tell us about eosinophilic disorders? *Seminars in Immunopathology 2021 43:3* **43**, 439–458 (2021).

253. Tsunemi, Y. *et al.* CCL17 transgenic mice show an enhanced Th2-type response to both allergic and non-allergic stimuli. *Eur J Immunol* **36**, 2116–2127 (2006).

254. Liwang, A. C., Wang, Z.-X., Sun, Y., Peiper, S. C. & LiWang, P. J. The solution structure of the anti-HIV chemokine vMIP-II. *Protein Science* **8**, (1999).

255. Stark, L. E., Guan, W., Colvin, M. E. & LiWang, P. J. The binding and specificity of chemokine binding proteins, through the lens of experiment and computation. *Biomed J* 1–15 (2021) doi:10.1016/j.bj.2021.07.004.

256. Alcami, A. & Saraiva, M. Chemokine Binding Proteins Encoded by Pathogens. (2013).

257. Bhusal, R. P. *et al.* Evasins: Tick Salivary Proteins that Inhibit Mammalian Chemokines. *Trends Biochem Sci* **45**, 108–122 (2020).

258. Carson, W. F. *et al.* Enhancement of macrophage inflammatory responses by CCL2 is correlated with increased miR-9 expression and downregulation of the ERK1/2 phosphatase Dusp6. *Cell Immunol* **314**, 63 (2017).

259. Marques, R. E., Guabiraba, R., Russo, R. C. & Teixeira, M. M. Targeting CCL5 in inflammation. *Expert Opin Ther Targets* **17**, 1439–1460 (2013).

260. Zhang, L. *et al.* Solution structure of the complex between poxvirus-encoded CC chemokine inhibitor vCCI and human MIP-1beta. *Proc Natl Acad Sci U S A.* **103**, 13985–13990 (2006).

261. Nguyen, A. F. *et al.* Biophysical and computational studies of the vCCI:VMIP-II complex. *Int J Mol Sci* **18**, (2017).

262. White, G. E., Mcneill, E., Christou, I., Channon, K. M. & Greaves, D. R. Site-Directed Mutagenesis of the CC Chemokine Binding Protein 35K-Fc Reveals Residues Essential for Activity and Mutations That Increase the Potency of CC Chemokine Blockade. *Mol Pharmacol* **80**, 328–336 (2011).

263. Barnes, P. J. Targeting cytokines to treat asthma and chronic obstructive pulmonary disease. *Nat Rev Immunol* **18**, 1–13 (2018).

264. Smit, J. J. & Lukacs, N. W. A closer look at chemokines and their role in asthmatic responses. *Eur J Pharmacol* **533**, 277–288 (2006).

265. Popp, M. W.-L. & Ploegh, H. L. Making and breaking peptide bonds: protein engineering using sortase. *Angew Chem Int Ed Engl* **50**, 5024–5032 (2011).

266. Piper, I. M. *et al.* Sequence variation in the β7-β8 loop of bacterial class A sortase enzymes alters substrate selectivity. *Journal of Biological Chemistry* **297**, 100981 (2021).

267. Aryal, P. *et al.* Swapping N-terminal regions among tick evasins reveals cooperative interactions influencing chemokine binding and selectivity. *Journal of Biological Chemistry* **298**, 102382 (2022).

268. Zajkowska, M. & Mroczko, B. From Allergy to Cancer—Clinical Usefulness of Eotaxins. *Cancers (Basel)* **13**, 1–13 (2021).

269. Semple, B. D., Kossmann, T. & Morganti-Kossmann, M. C. Role of chemokines in CNS health and pathology: a focus on the CCL2/CCR2 and CXCL8/CXCR2 networks. *J Cereb Blood Flow Metab* **30**, 459–473 (2010).

270. Lee, K. M.-C. *et al.* CCL17 in Inflammation and Pain. *The Journal of Immunology* **205**, 213–222 (2020).

271. Feng, G. *et al.* CCL17 Aggravates Myocardial Injury by Suppressing Recruitment of Regulatory T Cells. *Circulation* **145**, 765–782 (2022).

272. Stark, L. E., Guan, W., Colvin, M. E. & LiWang, P. J. The binding and specificity of chemokine binding proteins, through the lens of experiment and computation. *Biomed J* **45**, 439–453 (2022).

273. Dabbagh, K. *et al.* Local blockade of allergic airway hyperreactivity and inflammation by the poxvirus-derived pan-CC-chemokine inhibitor vCCI. *Journal of Immunology* **165**, 3418–3422 (2000).

274. Seet, B. T. *et al.* Molecular determinants for CC-chemokine recognition by a poxvirus CC-chemokine inhibitor. *Proc Natl Acad Sci. USA* **98**, 9008–9013 (2001).

275. Beck, C. G. *et al.* The viral CC chemokine-binding protein vCCI inhibits monocyte chemoattractant protein-1 activity by masking its CCR2B-binding site. *Journal of Biological Chemistry* **276**, 43270–43276 (2001).

276. Zhang, L. *et al.* Solution structure of the complex between poxvirus-encoded CC chemokine inhibitor vCCI and human MIP-1beta. *Proc Natl Acad Sci U S A.* **103**, 13985–13990 (2006).

277. Nguyen, A. F. *et al.* Biophysical and computational studies of the vCCI:VMIP-II complex. *Int J Mol Sci* **18**, (2017).

278. Stark, L. E., Guan, W., Colvin, M. E. & LiWang, P. J. The binding and specificity of chemokine binding proteins, through the lens of experiment and computation. *Biomed J* 1–15 (2021) doi:10.1016/j.bj.2021.07.004.

279. LiWang, P., Guan, W., Stark, L., Showalter, L. & Colvin, M. vCCI:Chemokine Interactions: Experimental Biochemistry Meets Computational Prediction. *The FASEB Journal* (2020) doi:10.1096/fasebj.2020.34.s1.07398.

280. Abraham, M. J. *et al.* GROMACS: High performance molecular simulations through multi-level parallelism from laptops to supercomputers. *SoftwareX* **1–2**, 19–25 (2015).

281. Hess, B., Bekker, H., Berendsen, H. J. C. & Fraaije, J. G. E. M. LINCS: A Linear Constraint Solver for Molecular Simulations. *J Comput Chem* **18**, 14631472 (1997).

282. Bussi, G., Donadio, D. & Parrinello, M. Canonical sampling through velocity rescaling. *J Chem Phys* **126**, (2007).

283. Parrinello, M. & Rahman, A. Polymorphic transitions in single crystals: A new molecular dynamics method. *J Appl Phys* **52**, 7182–7190 (1981).

284. Lindorff-Larsen, K. *et al.* Improved side-chain torsion potentials for the Amber ff99SB protein force field. *Proteins* **78**, 1950–1958 (2010).

285. Jorgensen, W. L., Chandrasekhar, J., Madura, J. D., Impey, R. W. & Klein, M. L. Comparison of simple potential functions for simulating liquid water. *J Chem Phys* **79**, 926–935 (1983).

286. Krissinel, E. & Henrick, K. Inference of macromolecular assemblies from crystalline state. *J Mol Biol* **372**, 774–797 (2007).

287. Aryal, P. *et al.* Swapping N-terminal regions among tick evasins reveals cooperative interactions influencing chemokine binding and selectivity. *Journal of Biological Chemistry* **298**, 102382 (2022).

288. Devkota, S. R. *et al.* Engineering broad-spectrum inhibitors of inflammatory chemokines from subclass A3 tick evasins. *Nature Communications 2023 14:1* **14**, 1–12 (2023).

289. Szeto, C., Lobos, C. A., Nguyen, A. T. & Gras, S. TCR Recognition of Peptide-MHC-I: Rule Makers and Breakers. *Int J Mol Sci* **22**, 1–26 (2020).

290. Guo, S. Insulin signaling, resistance, and the metabolic syndrome: insights from mouse models into disease mechanisms. *J Endocrinol* **220**, (2014).

291. de Las Rivas, J. & Fontanillo, C. Protein–Protein Interactions Essentials: Key Concepts to Building and Analyzing Interactome Networks. *PLoS Comput Biol* **6**, 1–8 (2010).

292. de Las Rivas, J. & Fontanillo, C. Protein–Protein Interactions Essentials: Key Concepts to Building and Analyzing Interactome Networks. *PLoS Comput Biol* **6**, 1–8 (2010).

293. Wedemeyer, M. J. *et al.* The chemokine X-factor: Structure-function analysis of the CXC motif at CXCR4 and ACKR3. *J Biol Chem* **295**, 13927–13939 (2020).

294. Eaton, J. R. O. *et al.* The N-terminal domain of a tick evasin is critical for chemokine binding and neutralization and confers specific binding activity to other evasins. *J Biol Chem* **293**, 6134–6146 (2018).

295. White, G. E., Mcneill, E., Christou, I., Channon, K. M. & Greaves, D. R. Site-Directed Mutagenesis of the CC Chemokine Binding Protein 35K-Fc Reveals Residues Essential for Activity and Mutations That Increase the Potency of CC Chemokine Blockade. *Mol Pharmacol* **80**, 328–336 (2011).

296. Arnold, P. L. & Fremont, D. H. Structural Determinants of Chemokine Binding by an Ectromelia Virus-Encoded Decoy Receptor. *J Virol* **80**, 7439–7449 (2006).

297. Seet, B. T. *et al.* Molecular determinants for CC-chemokine recognition by a poxvirus CC-chemokine inhibitor. *Proc Natl Acad Sci. USA* **98**, 9008–9013 (2001).

298. Beck, C. G. *et al.* The viral CC chemokine-binding protein vCCI inhibits monocyte chemoattractant protein-1 activity by masking its CCR2B-binding site. *Journal of Biological Chemistry* **276**, 43270–43276 (2001).

299. Kuo, N.-W. *et al.* Structural Insights into the Interaction between a Potent Anti-inflammatory Protein, Viral CC Chemokine Inhibitor (vCCI), and the Human CC Chemokine, Eotaxin-1. *Journal of Biological Chemistry* **289**, 6592–6603 (2014).

300. Nguyen, A. F. *et al.* Biophysical and computational studies of the vCCI:VMIP-II complex. *Int J Mol Sci* **18**, (2017).

301. Arnold, P. L. & Fremont, D. H. Structural Determinants of Chemokine Binding by an Ectromelia Virus-Encoded Decoy Receptor. *J Virol* **80**, 7439–7449 (2006).

302. White, G. E., Mcneill, E., Christou, I., Channon, K. M. & Greaves, D. R. Site-Directed Mutagenesis of the CC Chemokine Binding Protein 35K-Fc Reveals Residues Essential for Activity and Mutations That Increase the Potency of CC Chemokine Blockade. *Mol Pharmacol* **80**, 328–336 (2011).

303. Aryal, P. *et al.* Swapping N-terminal regions among tick evasins reveals cooperative interactions influencing chemokine binding and selectivity. *Journal of Biological Chemistry* **298**, 102382 (2022).

304. Devkota, S. R. *et al.* Engineering broad-spectrum inhibitors of inflammatory chemokines from subclass A3 tick evasins. *Nat Commun* **14**, (2023).

305. HIV. https://www.who.int/data/gho/data/themes/hiv-aids.

306. Current Trends Update on Acquired Immune Deficiency Syndrome (AIDS) -- United States. https://www.cdc.gov/mmwr/preview/mmwrhtml/00001163.htm.

307. Unexplained Immunodeficiency and Opportunistic Infections in Infants -- New York, New Jersey, California. https://www.cdc.gov/mmwr/preview/mmwrhtml/00001208.htm.

308. Who Is at Risk for HIV and AIDS? | HIV.gov. https://www.hiv.gov/hiv-basics/overview/about-hiv-and-aids/who-is-at-risk-for-hiv/.

309. The Global HIV/AIDS Epidemic | KFF. https://www.kff.org/global-health-policy/fact-sheet/the-global-hivaids-epidemic/.

310. Nájera, R., Herrera, M. I. & de Andrés, R. Human Immunodeficiency Virus and Related Retroviruses. *Western Journal of Medicine* **147**, 702 (1987).

311. Hoorelbeke, B. *et al.* HIV-1 envelope trimer has similar binding characteristics for carbohydrate-binding agents as monomeric gp120. *FEBS Lett* **587**, 860–866 (2013).

312. Moebius, U., Clayton, L. K., Abraham, S., Harrison, S. C. & Reinherz, E. L. The human immunodeficiency virus gp120 binding site on CD4: delineation by

quantitative equilibrium and kinetic binding studies of mutants in conjunction with a high-resolution CD4 atomic structure. *J Exp Med* **176**, 507–517 (1992).

313. The HIV Challenge - IAVI. https://www.iavi.org/news-resources/the-hiv-challenge/the-challenge-of-developing-an-hiv-vaccine.

314. Janssen and Global Partners to Discontinue Phase 3 Mosaico HIV Vaccine Clinical Trial | Johnson & Johnson. https://www.jnj.com/janssen-and-global-partners-to-discontinue-phase-3-mosaico-hiv-vaccine-clinical-trial.

315. Kufel, W. D. Antibody-based strategies in HIV therapy. *Int J Antimicrob Agents* **56**, (2020).

316. Protease Inhibitor-Based Regimens | NIH. https://clinicalinfo.hiv.gov/en/guidelines/hiv-clinical-guidelines-adult-and-adolescent-arv/protease-inhibitor-based-regimens.

317. The Only H.I.V. Vaccine in Advanced Trials Has Failed. What Now? - The New York Times. https://www.nytimes.com/2023/01/18/health/hiv-vaccine-janssen.html.

318. FDA approves first drug for reducing the risk of sexually acquired HIV infection | HIV.gov. https://www.hiv.gov/blog/fda-approves-first-drug-for-reducing-the-risk-of-sexually-acquired-hiv-infection/.

319. PrEP Effectiveness | PrEP | HIV Basics | HIV/AIDS | CDC. https://www.cdc.gov/hiv/basics/prep/prep-effectiveness.html.

320. Unaids. Putting HIV prevention among adolescent girls and young women on the Fast-Track and engaging men and boys.

321. Krakower, D. S., Jain, S. & Mayer, K. H. Antiretrovirals for Primary HIV Prevention: The Current Status of Pre- and Post-Exposure Prophylaxis. *Curr HIV/AIDS Rep* **12**, 127 (2015).

322. Microbicides | HIV.gov. https://www.hiv.gov/hiv-basics/hiv-prevention/potential-future-options/microbicides/.

323. Shattock, R. J. & Rosenberg, Z. Microbicides: Topical Prevention against HIV. *Cold Spring Harb Perspect Med* **2**, (2012).

324. Altman, G. H. *et al. Silk-Based Biomaterials*. *Biomaterials* vol. 24 (2003).

325. Suture Nonabsorbable - Silk 510(k) FDA Premarket Notification K930826 SURGICAL SPECIALTIES, INC. https://fda.report/PMN/K930826.

326. Jewell, M., Daunch, W., Bengtson, B. & Mortarino, E. The development of SERI® Surgical Scaffold, an engineered biological scaffold. *Ann N Y Acad Sci* **1358**, 44–55 (2015).

327. Silk Fabrics in the Management of Atopic Dermatitis. https://www.skintherapyletter.com/atopic-dermatitis/silk-fabrics/.

328. Ricci, G., Patrizi, A., Bellini, F. & Medri, M. Use of textiles in atopic dermatitis: care of atopic dermatitis. *Curr Probl Dermatol* **33**, 127–143 (2006).

329. Lee, J. H., Lee, J. S., Kim, D. K., Park, C. H. & Lee, H. R. Clinical Outcomes of Silk Patch in Acute Tympanic Membrane Perforation. *Clin Exp Otorhinolaryngol* **8**, 117 (2015).

330. Zhang, W. *et al.* Silk Fibroin Biomaterial Shows Safe and Effective Wound Healing in Animal Models and a Randomized Controlled Clinical Trial. *Adv Healthc Mater* **6**, 1700121 (2017).

331. Yucel, T., Lovett, M. L. & Kaplan, D. L. Silk-Based Biomaterials for Sustained Drug Delivery. *J Control Release* **0**, 381–397 (2014).

332. Joseph, B. & Justin Raj, S. Therapeutic applications and properties of silk proteins from Bombyx mori. (2013) doi:10.1080/21553769.2012.760491.

333. Wang, Y. *et al.* In vivo Degradation of Three-Dimensional Silk Fibroin Scaffolds. *Biomaterials* **29**, 3415 (2008).

334. Panda, S. *et al.* Biocompatible CaTiO3-PVDF composite-based piezoelectric nanogenerator for exercise evaluation and energy harvesting. *Nano Energy* **102**, 107682 (2022).

335. Bosio, V. E., Rybner, C. & Kaplan, D. Concentric-mineralized hybrid silk-based scaffolds for bone tissue engineering in vitro models. *J Mater Chem B* (2023) doi:10.1039/D3TB00717K.

336. Bosio, V. E., Brown, J., Rodriguez, M. J. & Kaplan, D. L. Biodegradable porous silk microtubes for tissue vascularization. *J Mater Chem B* **5**, 1227–1235 (2017).

337. Bosio, V. E., Islan, G. A., Martínez, Y. N., Durán, N. & Castro, G. R. Nanodevices for the immobilization of therapeutic enzymes. *http://dx.doi.org/10.3109/07388551.2014.990414* **36**, 447–464 (2015).

338. Mu, X. *et al.* Small tissue chips with big opportunities for space medicine. *Life Sci Space Res (Amst)* **35**, 150–157 (2022).

339. Mu, X., Gerhard-Herman, M. D. & Zhang, Y. S. Building Blood Vessel Chips with Enhanced Physiological Relevance. *Adv Mater Technol* **8**, 2201778 (2023).

340. Liu, J. *et al.* Promotion of Wound Healing Using Nanoporous Silk Fibroin Sponges. *ACS Appl Mater Interfaces* **15**, 12696–12707 (2023).

341. Liu, J. *et al.* A negative-response strain sensor towards wearable microclimate changes for body area sensing networks. *Chemical Engineering Journal* **459**, 141628 (2023).

342. Yavuz, B. *et al.* Sustained Release Silk Fibroin Discs: Antibody and Protein Delivery for HIV Prevention Corresponding Authors: HHS Public Access. *J Control Release* **301**, 1–12 (2019).

343. Florczak, A. *et al.* Silk Particles as Carriers of Therapeutic Molecules for Cancer Treatment. *Materials (Basel)* **13**, 1–33 (2020).

344. Fischer, K., Nguyen, K. & LiWang, P. J. Griffithsin Retains Anti-HIV-1 Potency with Changes in gp120 Glycosylation and Complements Broadly Neutralizing Antibodies PGT121 and PGT126. *Antimicrob Agents Chemother* **64**, (2020).

345. Xue, J. *et al.* The role of individual carbohydrate-binding sites in the function of the potent anti-HIV lectin griffithsin. *Mol Pharm* **9**, 2613–2625 (2012).

346. Xue, J. *et al.* The griffithsin dimer is required for high-potency inhibition of HIV-1: evidence for manipulation of the structure of gp120 as part of the griffithsin dimer mechanism. *Antimicrob Agents Chemother* **57**, 3979–3989 (2013).

347. O'Keefe, B. R. *et al.* Broad-Spectrum In Vitro Activity and In Vivo Efficacy of the Antiviral Protein Griffithsin against Emerging Viruses of the Family Coronaviridae. *J Virol* **84**, 2511 (2010).

348. Alsaidi, S. *et al.* Griffithsin and Carrageenan Combination Results in Antiviral Synergy against SARS-CoV-1 and 2 in a Pseudoviral Model. *Mar Drugs* **19**, (2021).

349. Meuleman, P. *et al.* Griffithsin Has Antiviral Activity against Hepatitis C Virus. *Antimicrob Agents Chemother* **55**, 5159 (2011).

350. Derby, N. *et al.* Griffithsin carrageenan fast dissolving inserts prevent SHIV HSV-2 and HPV infections in vivo. *Nat Commun* **9**, (2018).

351. Ishag, H. Z. A. *et al.* Griffithsin inhibits Japanese encephalitis virus infection in vitro and in vivo. *Arch Virol* **158**, 349 (2013).

352. Zhao, Y. *et al.* An algal lectin griffithsin inhibits Hantaan virus infection in vitro and in vivo. *Front Cell Infect Microbiol* **12**, (2022).

353. Zhao, B., Mankowski, M. K., Snyder, B. A., Ptak, R. G. & LiWang, P. J. Highly Potent Chimeric Inhibitors Targeting Two Steps of HIV Cell Entry. *J Biol Chem* **286**, 28370 (2011).

354. Kagiampakis, I. *et al.* Potent Strategy To Inhibit HIV-1 by Binding both gp120 and gp41. *Antimicrob Agents Chemother* **55**, 264 (2011).

355. Li, M. *et al.* Human Immunodeficiency Virus Type 1 env Clones from Acute and Early Subtype B Infections for Standardized Assessments of Vaccine-Elicited Neutralizing Antibodies . *J Virol* **79**, 10108–10125 (2005).

356. Naldini, L., Blomer, U., Gage, F. H., Trono, D. & Verma, I. M. Efficient transfer, integration, and sustained long-term expression of the transgene in adult rat brains injected with a lentiviral vector. *Proceedings of the National Academy of Sciences* **93**, 11382–11388 (1996).

357. Harrison, T., Graham, F. & Williams, J. Host-range mutants of adenovirus type 5 defective for growth in HeLa cells. *Virology* **77**, 319–329 (1977).

358. Graham, F. L., Smiley, J., Russell, W. C. & Nairn, R. Characteristics of a human cell line transformed by DNA from human adenovirus type 5. *Journal of General Virology* **36**, 59–72 (1977).

359. Platt, E. J., Wehrly, K., Kuhmann, S. E., Chesebro, B. & Kabat, D. Effects of CCR5 and CD4 cell surface concentrations on infections by macrophagetropic isolates of human immunodeficiency virus type 1. *J Virol* **72**, 2855–2864 (1998).

360. Rockwood, D. N. *et al.* Materials fabrication from Bombyx mori silk fibroin. *Nature Protocols 2011 6:10* **6**, 1612–1631 (2011).

361. Summerfield, A., Meurens, F. & Ricklin, M. E. The immunology of the porcine skin and its value as a model for human skin. *Mol Immunol* **66**, 14–21 (2015).

362. Khiao In, M. *et al.* Histological and functional comparisons of four anatomical regions of porcine skin with human abdominal skin. *Anat Histol Embryol* **48**, 207–217 (2019).

363. Zhou, X. *et al.* Identification of Cell Markers and Their Expression Patterns in Skin Based on Single-Cell RNA-Sequencing Profiles. *Life* **12**, (2022).

364. Lucas, A. M., Stettenheim, P. R. & Project, A. A. *Avian Anatomy Integument Part I.*

365. Panico, A., Paladini, F. & Pollini, M. Development of regenerative and flexible fibroin-based wound dressings. *J Biomed Mater Res B Appl Biomater* **107**, 7–18 (2019).

366. Brown, J. E. *et al.* Thermal and Structural Properties of Silk Biomaterials Plasticized by Glycerol. *Biomacromolecules* **17**, 3911–3921 (2016).

367. Lawrence, B. D., Omenetto, F., Chui, K. & Kaplan, D. L. Processing methods to control silk fibroin film biomaterial features. *J Mater Sci* **43**, 6967–6985 (2008).

368. FDA Approves First Injectable Treatment for HIV Pre-Exposure Prevention | FDA. https://www.fda.gov/news-events/press-announcements/fda-approves-first-injectable-treatment-hiv-pre-exposure-prevention.

369. Vaginal Microbicides:Development for the Prevention of HIV Infection PDF | FDA. https://www.fda.gov/regulatory-information/search-fda-guidance-documents/vaginal-microbicidesdevelopment-prevention-hiv-infection-pdf.

370. Study suggests dapivirine vaginal ring is safe to use as HIV prevention during breastfeeding | Department of Epidemiology. https://epi.washington.edu/news/study-suggests-dapivirine-vaginal-ring-is-safe-to-use-as-hiv-prevention-during-breastfeeding/.

371. Baeten, J. M. *et al.* Use of a Vaginal Ring Containing Dapivirine for HIV-1 Prevention in Women. *N Engl J Med* **375**, 2121–2132 (2016).

372. Karim, Q. A. *et al.* Effectiveness and safety of tenofovir gel, an antiretroviral microbicide, for the prevention of HIV infection in women. *Science* **329**, 1168–1174 (2010).

373. Marrazzo, J. M. *et al.* Tenofovir-based preexposure prophylaxis for HIV infection among African women. *N Engl J Med* **372**, 509–518 (2015).

374. Delany-Moretlwe, S. *et al.* Tenofovir 1% vaginal gel for prevention of HIV-1 infection in women in South Africa (FACTS-001): a phase 3, randomised, double-blind, placebo-controlled trial. *Lancet Infect Dis* **18**, 1241–1250 (2018).

375. Mayo, A. J. *et al.* Acceptability of the Dapivirine Vaginal Ring for HIV-1 Prevention and Association with Adherence in a Phase III Trial. *AIDS Behav* **25**, 2430–2440 (2021).

376. Naidoo, K. *et al.* Efficacy and Action of the Dapivirine Vaginal Ring as Understood by Women Participating in an Open Label Extension Study. *AIDS Behav* **27**, 75–81 (2023).

377. Full report — In Danger: UNAIDS Global AIDS Update 2022 | UNAIDS. https://www.unaids.org/en/resources/documents/2022/in-danger-global-aids-update.

378. Crakes, K. R. *et al.* PPARα-targeted mitochondrial bioenergetics mediate repair of intestinal barriers at the host-microbe intersection during SIV infection. doi:10.1073/pnas.1908977116/-/DCSupplemental.

379. Lagakos, S. W. & Gable, A. R. Methodological challenges in biomedical HIV prevention trials. *Methodological Challenges in Biomedical HIV Prevention Trials* 1–258 (2008) doi:10.17226/12056.

380. Saag, M. S. Preventing HIV in Women — Still Trying to Find Their VOICE. *New England Journal of Medicine* **372**, 564–566 (2015).

381. Coburn, J. M., Na, E. & Kaplan, D. L. Modulation of vincristine and doxorubicin binding and release from silk films. *J Control Release* **220**, 229–238 (2015).

382. Griffithsin-based Rectal Microbicide for PREvention of Viral ENTry (PREVENT) - Full Text View - ClinicalTrials.gov. https://clinicaltrials.gov/ct2/show/NCT04032717.

383. Lusvarghi, S. & Bewley, C. A. Griffithsin: An antiviral lectin with outstanding therapeutic potential. *Viruses* vol. 8 Preprint at https://doi.org/10.3390/v8100296 (2016).

384. Tyo, K. M. *et al.* Sustained-release Griffithsin nanoparticle-fiber composites against HIV-1 and HSV-2 infections. *J Control Release* **321**, 84–99 (2020).

385. Barton, C. *et al.* Activity of and Effect of Subcutaneous Treatment with the Broad-Spectrum Antiviral Lectin Griffithsin in Two Laboratory Rodent Models. *Antimicrob Agents Chemother* **58**, 120 (2014).

386. Tyo, K. M. *et al.* Rapid-Release Griffithsin Fibers for Dual Prevention of HSV-2 and HIV-1 Infections. *Antimicrob Agents Chemother* **64**, (2020).

387. Minooei, F., Fried, J. R., Fuqua, J. L., Palmer, K. E. & Steinbach-Rankins, J. M. In vitro Study on Synergistic Interactions Between Free and Encapsulated Q-Griffithsin and Antiretrovirals Against HIV-1 Infection. *Int J Nanomedicine* **16**, 1189–1206 (2021).

388. Teleshova, N. *et al.* Results of a phase 1, randomized, placebo-controlled first-in-human trial of griffithsin formulated in a carrageenan vaginal gel. *PLoS One* **17**, (2022).

389. Franzén Boger, M. *et al.* A topical rectal douche product containing Q-Griffithsin does not disrupt the epithelial border or alter CD4+ cell distribution in the human rectal mucosa. *Sci Rep* **13**, (2023).

390. Cai, Y. *et al.* Griffithsin with A Broad-Spectrum Antiviral Activity by Binding Glycans in Viral Glycoprotein Exhibits Strong Synergistic Effect in Combination with A Pan-Coronavirus Fusion Inhibitor Targeting SARS-CoV-2 Spike S2 Subunit. *Virol Sin* **35**, 857 (2020).

391. Ahan, R. E. *et al.* A Highly Potent SARS-CoV-2 Blocking Lectin Protein. *ACS Infect Dis* **8**, 1253–1264 (2022).

392. PHASE 1 CLINICAL TRIALS OF A Q-GRIFFITHSIN NASAL SPRAY FOR SARS-CoV-2 PROPHYLAXIS - CROI Conference. https://www.croiconference.org/abstract/phase-1-clinical-trials-of-a-q-griffithsin-nasal-spray-for-sars-cov-2-prophylaxis/.

393. Gao, X. *et al.* A medical adhesive used in a wet environment by blending tannic acid and silk fibroin. *Biomater Sci* **8**, 2694–2701 (2020).

394. CFR - Code of Federal Regulations Title 21.

395. Li, Y., Liao, M. & Zhou, J. Catechol-cation adhesion on silica surfaces: molecular dynamics simulations. *Phys Chem Chem Phys* **19**, 29222–29231 (2017).

396. Semaming, Y., Pannengpetch, P., Chattipakorn, S. C. & Chattipakorn, N. Pharmacological properties of protocatechuic Acid and its potential roles as complementary medicine. *Evid Based Complement Alternat Med* **2015**, (2015).

397. Abruzzo, A. *et al.* Mucoadhesive Buccal Films for Local Delivery of Lactobacillus brevis. *Pharmaceutics 2020, Vol. 12, Page 241* **12**, 241 (2020).

398. Yin, J., Fang, Y., Xu, L. & Ahmed, A. High-throughput fabrication of silk fibroin/hydroxypropyl methylcellulose (SF/HPMC) nanofibrous scaffolds for skin tissue engineering. *Int J Biol Macromol* **183**, 1210–1221 (2021).

399. Umuhoza, D. *et al.* Strategies for Tuning the Biodegradation of Silk Fibroin-Based Materials for Tissue Engineering Applications. *ACS Biomater Sci Eng* **6**, 1290–1310 (2020).

400. Bory, C. *et al.* Effect of polyethylene glycol-modified adenosine deaminase (PEG-ADA) therapy in two ADA-deficient children: measurement of erythrocyte deoxyadenosine triphosphate as a useful tool. *Adv Exp Med Biol* **309A**, 173–176 (1991).

401. Verbeken, G. *et al.* Glycerol treatment as recovery procedure for cryopreserved human skin allografts positive for bacteria and fungi. *Cell Tissue Bank* **13**, 1 (2012).

402. Marshall, L. *et al.* Effect of glycerol on intracellular virus survival: implications for the clinical use of glycerol-preserved cadaver skin. *Burns* **21**, 356–361 (1995).

403. Rajagopalan, L. & Rajarathnam, K. Structural Basis of Chemokine Receptor Function—A Model for Binding Affinity and Ligand Selectivity. *Biosci Rep* **26**, 325 (2006).

404. Hughes, C. E. & Nibbs, R. J. B. A guide to chemokines and their receptors. *FEBS Journal* vol. 285 2944–2971 Preprint at https://doi.org/10.1111/febs.14466 (2018).

405. Chemokine. *Br J Pharmacol* **158**, S35 (2009).

406. Wennerås, C. *et al.* Eosinophil Trafficking. *Eosinophils in Health and Disease* 121–166 (2013) doi:10.1016/B978-0-12-394385-9.00006-7.

407. Giancarlo, B., Silvano, S., Albert, Z., Alberto, M. & Paola, A. Migratory response of human natural killer cells to lymphotactin. *Eur J Immunol* **26**, 3238–3241 (1996).

408. Fox, J. C. *et al.* Structural and agonist properties of XCL2, the other member of the C-chemokine subfamily. *Cytokine* **71**, 302 (2015).

409. Lopez, A., Huang, Y. & Zheng, J. CX3CR1 Chemokine Receptor. *xPharm: The Comprehensive Pharmacology Reference* 1–4 (2007) doi:10.1016/B978-008055232-3.60169-2.

410. Knerlich-Lukoschus, F. Mechanisms of CNP following SCI: Chemokines in neuronal-glial cell interaction. *Spinal Cord Injury Pain* 315–338 (2022) doi:10.1016/B978-0-12-818662-6.00004-2.

411. Moser, B. & Loetscher Background, P. CHEMOKINE REVIEWS Lymphocyte traffic control by chemokines. (2001).

412. Palomino, D. C. arolina T. & Marti, L. C. avalheiro. Chemokines and immunity. *Einstein* **13**, 469 (2015).

413. Ohta, T. *et al.* Crucial roles of XCR1-expressing dendritic cells and the XCR1-XCL1 chemokine axis in intestinal immune homeostasis. *Sci Rep* **6**, (2016).

414. Blanchet, X., Langer, M., Weber, C., Koenen, R. & von Hundelshausen, P. Touch of chemokines. *Front Immunol* **3**, 25939 (2012).

415. Saeki, H. & Tamaki, K. Thymus and activation regulated chemokine (TARC)/CCL17 and skin diseases. *J Dermatol Sci* **43**, 75–84 (2006).

416. Imai, T. *et al.* Molecular cloning of a novel T cell-directed CC chemokine expressed in thymus by signal sequence trap using Epstein-Barr virus vector. *J Biol Chem* **271**, 21514–21521 (1996).

417. Yoshie, O. & Matsushima, K. CCR4 and its ligands: from bench to bedside. *Int Immunol* **27**, 11–20 (2015).

418. Lupancu, T. J., Eivazitork, M., Hamilton, J. A., Achuthan, A. A. & Lee, K. M. C. CCL17/TARC in autoimmunity and inflammation-not just a T-cell chemokine. *Immunol Cell Biol* **101**, 600–609 (2023).

419. Semple, B. D., Bye, N., Rancan, M., Ziebell, J. M. & Morganti-Kossmann, M. C. Role of CCL2 (MCP-1) in traumatic brain injury (TBI): evidence from severe TBI patients and CCL2-/- mice. *J Cereb Blood Flow Metab* **30**, 769–782 (2010).

420. Altinoz, E. *et al.* Neuroprotection against CCl4 induced brain damage with crocin in Wistar rats. *Biotech Histochem* **93**, 623–631 (2018).

421. Gyoneva, S. & Ransohoff, R. M. Inflammatory reaction after traumatic brain injury: Therapeutic potential of targeting cell-cell communication by chemokines. *Trends Pharmacol Sci* **36**, 471 (2015).

422. Ciechanowska, A. *et al.* Traumatic brain injury in mice induces changes in the expression of the XCL1/XCR1 and XCL1/ITGA9 axes. *Pharmacological Reports* **72**, 1579 (2020).

423. Ivanovska, M. *et al.* CCL-11 or Eotaxin-1: An Immune Marker for Ageing and Accelerated Ageing in Neuro-Psychiatric Disorders. *Pharmaceuticals* **13**, 1–17 (2020).

424. Ashutosh *et al.* CXCL8 protects human neurons from amyloid-β-induced neurotoxicity: Relevance to Alzheimer's disease. *Biochem Biophys Res Commun* **412**, 565 (2011).

Appendix A
Supplemental Materials for Chapter 2

Supplementary table 2.1: CC chemokine nomenclature

Nomenclature	Colloquial name	Nomenclature	Colloquial name
CCL1	I-309	CCL15	HCC-2
CCL2	MCP-1	CCL16	HCC-4
CCL3	MIP-1α	CCL17	TARC
CCL4	MIP-1β	CCL18	PARC
CCL5	RANTES	CCL19	MIP-3β
CCL6	C10	CCL20	MIP-3α
CCL7	MCP-3	CCL21	6-Ckine
CCL8	MCP-2	CCL22	MDC
CCL9	MIP-1γ	CCL23	MIP-3
CCL10	IP-10	CCL24	Eotaxin-2
CCL11	Eotaxin-1	CCL25	TECK
CCL12	MCP-5	CCL26	Eotaxin-3
CCL13	MCP-4	CCL27	CTACK
CCL14	HCC-1	CCL28	MEC
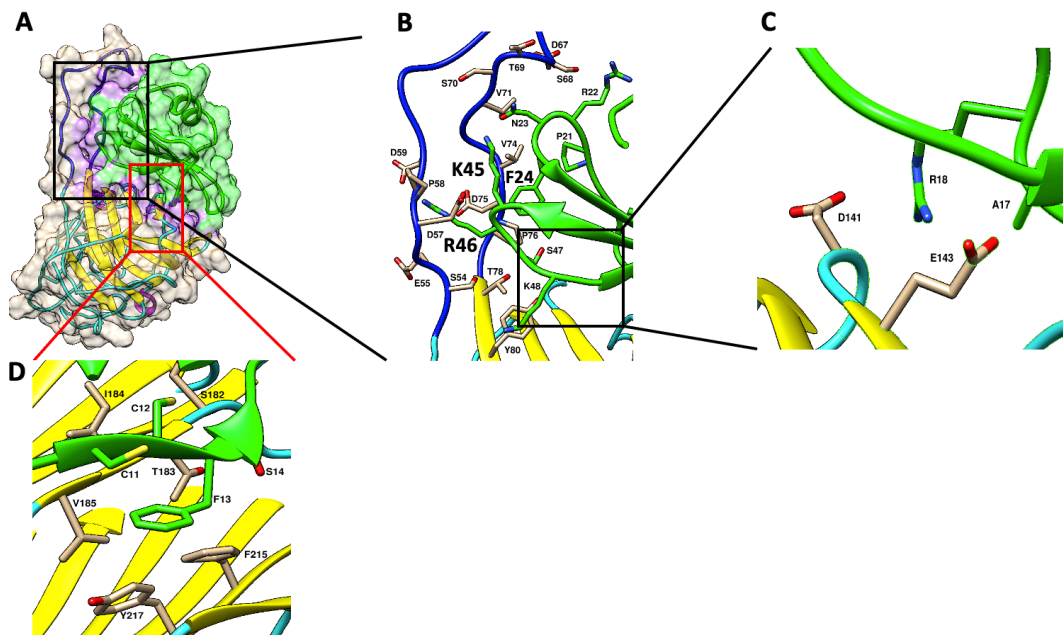
Supplementary Figure 2.1: Key residues identified in the vCCI-CCL4 complex through

Images from (A) vCCI-CCL4 complex from Figure 2 highlighting (B) F24 and 40s loop, (C) R18, and (D) F13 of CCL4 while bound to rabbitpox vCCI. The vCCI residues (beige) and CCL4 residues (green) involved in the interface are represented in stick form with hydrogens removed to show side chains.
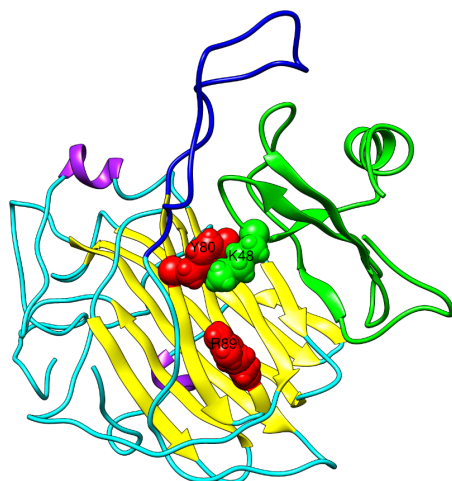
Supplementary Figure 2.2: rabbitpox vCCI with CCL4 WT

Rabbitpox vCCI with CCL4 WT (PDB ID: 2FFK, computationally mutated back to the wild type CCL4, and simulated with MD for 1μs), highlighting Y80 and R89 of vCCI, and K48 of CCL4.
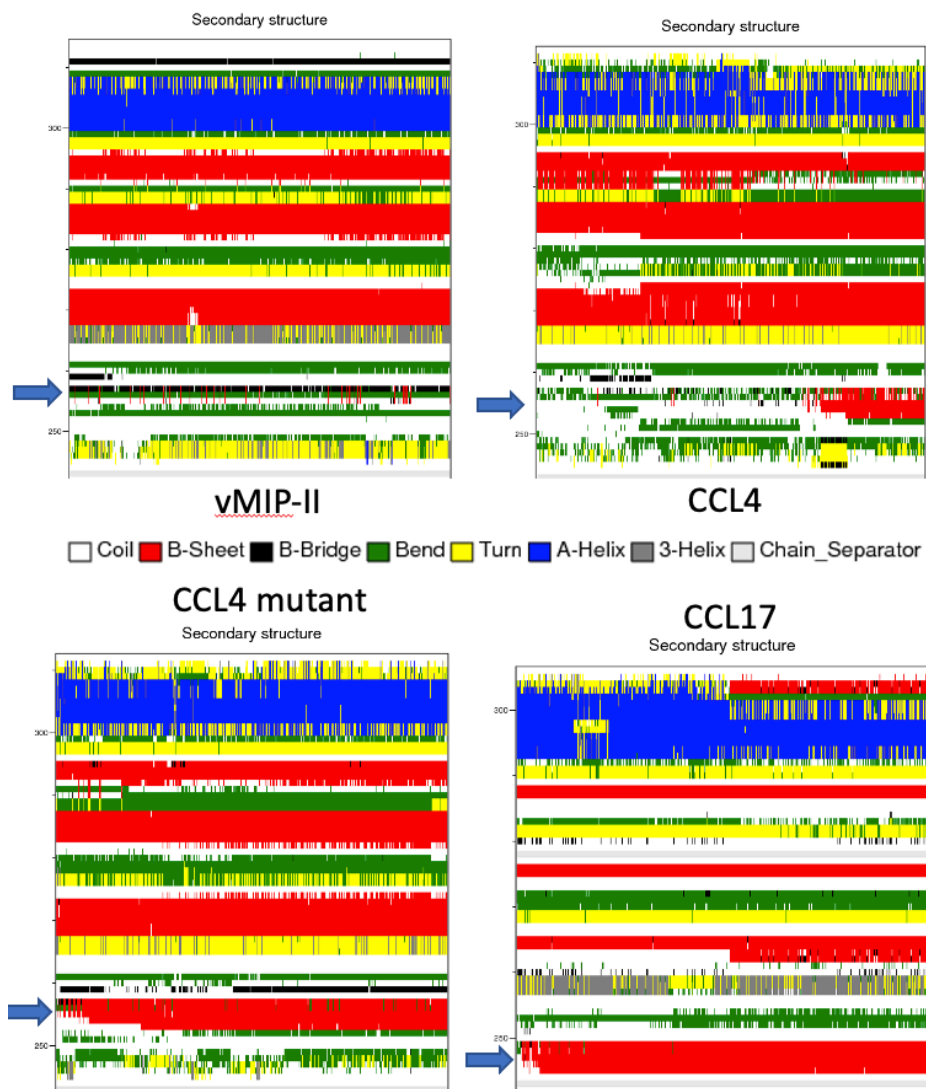
Supplementary Figure 2.3: Plots of the secondary structure of chemokines reveals additional β strand formation upon complex with vCCl.

Secondary structure plots for vMIP-II, CCL4 WT, CCL4 variant (K45A/R46A/K48A), and CCL17 throughout the simulation. The x-axis represents simulation time and the y-axis represents chemokine residue. The color legend for each secondary structure is shown between the two rows of plots. Arrows on the left of each image indicate where the additional b strand around residues 8-14 forms upon complex with vCCl. The secondary structure for each 2 ns frame in the MD trajectories was computed using the algorithm *Define Secondary Structure of Proteins* (DSSP) [Kabsch W, Sander C (1983). "Dictionary of protein secondary structure: pattern recognition of hydrogen-bonded and geometrical features". Biopolymers. 22 (12): 2577–637. doi:10.1002/bip.360221211].

A
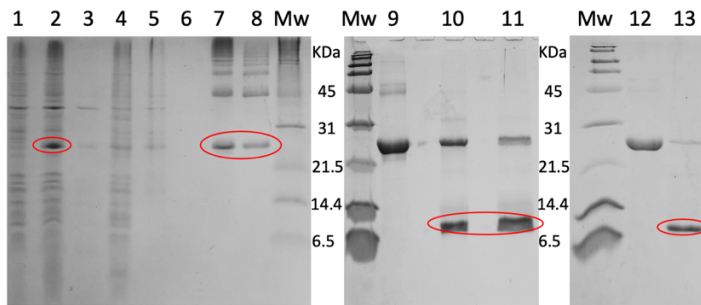
B

C
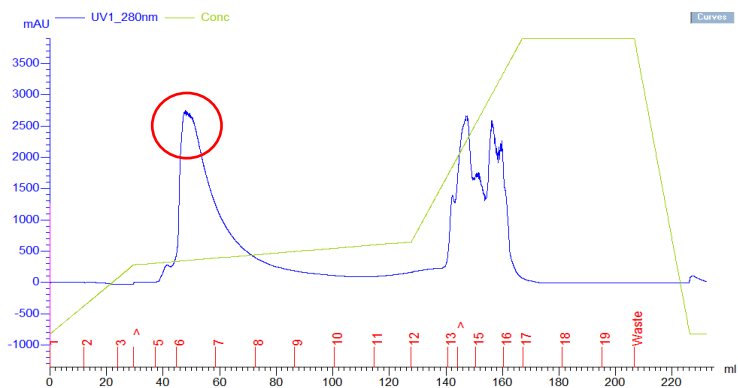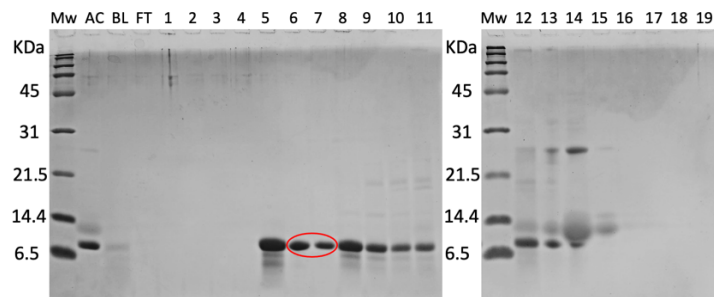
Supplementary Figure 3.1: Purification of vMIP-II-LPMTG-CHis. A. Expression of Trx-vMIP-II-LPMTG-CHis, Ni-NTA column purification, and cleavage. Lane 1: Pre-induction. Lane 2: 3 hr post-induction at 37°C. Lane 3: Pellet of cell lysate. Lane 4: Flow through of Ni-NTA column. Lane 5 and 6: The first and second wash of Ni-NTA column. Lane 7 and 8: Elution from Ni-NTA column. Lane 9 and 12: After dialysis and before adding EK to cleave the protein. Lane 10: After adding EK for 1 day. Lane 11: After adding EK for 2 days. Lane 13: After adding EK for 3 days. B. The C4 column trace after the protein cleavage. The peak of the target protein, vMIP-II-LPMTG-CHis, is circled. C. The SDS-PAGE gel of the fractions from the C4 column. Left lane is the molecular weight marker; second lane is the protein after cleavage for 3 days; third lane is the sample before loading to the C4 column (the protein is diluted); the fourth lane is the flow through of the C4 column, followed by the fractions of the C4 column. The fraction 6 and 7 circled in the gel are the main fractions of vMIP-II-LPMTG-CHis.
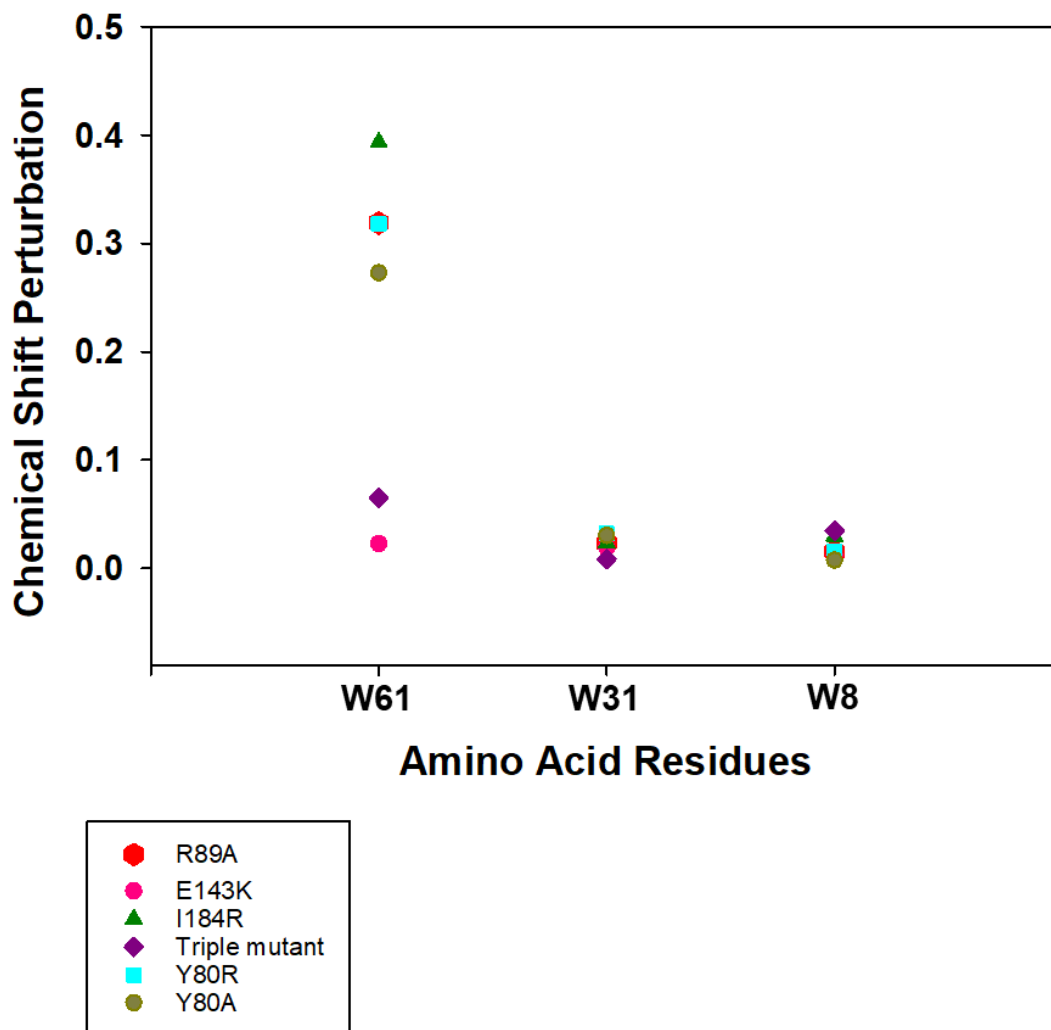
Supplementary Figure 4.1: Overlay of chemical shift perturbation of Tryptophan side chain residues of 15N-vMIP upon the formation of complex with (A) ^{14}N-vCCl-Y80A (light green), (B) ^{14}N-vCCl-E143K (pink), (C) ^{14}N-vCCl-R89A (red), (D) ^{14}N-vCCl-I184R (dark green), (E) ^{14}N-vCCl-Y80R (cyan), (F) ^{14}N-vCCl-TM (triple mutant- Y80R-E143K-I184R) (purple).
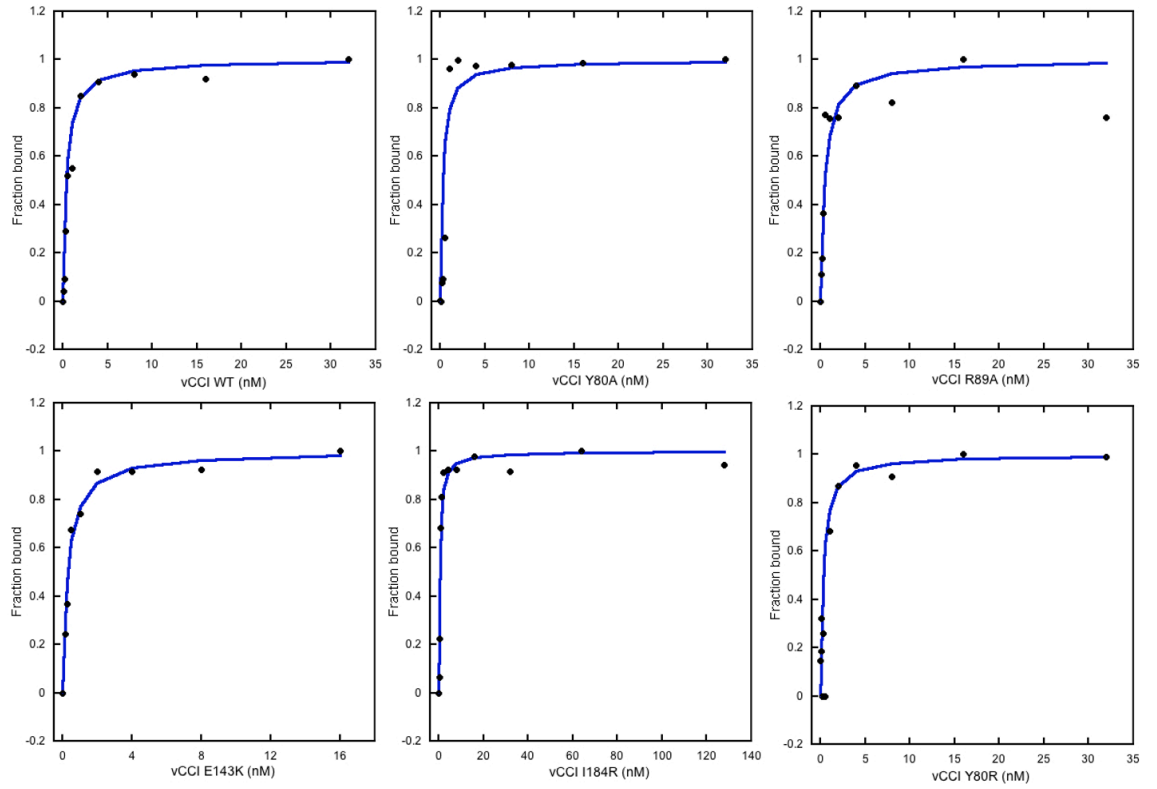
Supplementary Figure 4.2: The binding curve of vCCI WT and its variant from fluorescence anisotropy assay
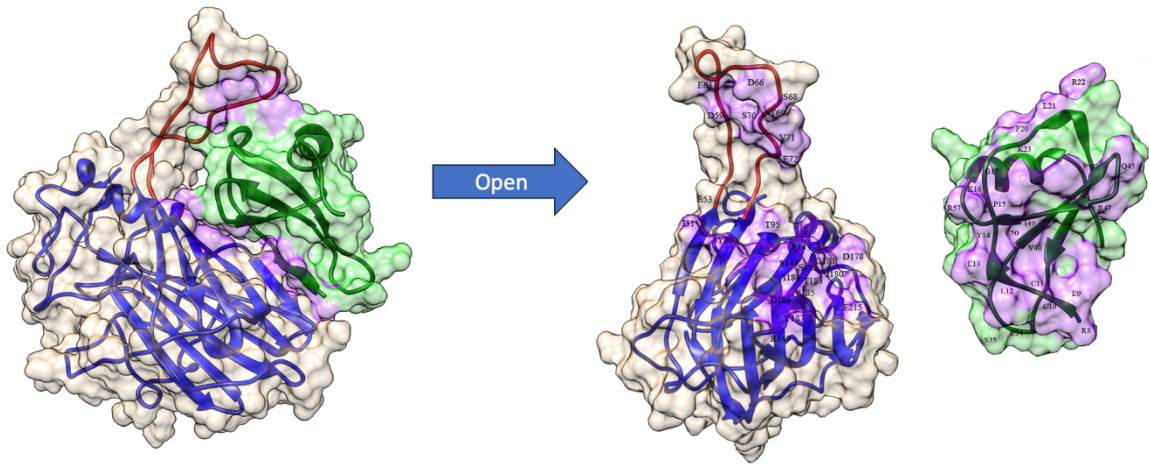
vCCI WT – CCL17 WT

vCCI WT – CCL17 G17R/V44K/Q45R
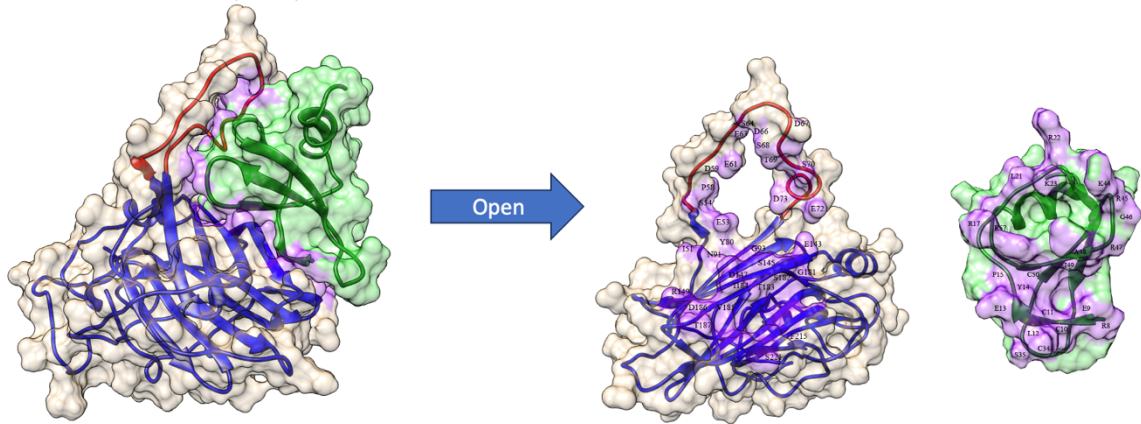
Supplementary Figure 5.1: Images of vCCI:CCL17 wild type (top) and vCCI:CCL17 triple mutant (bottom) after 1 microsecond of molecular dynamics simulation. The vCCI is shown with a blue secondary structure ribbon and cream-colored surface and the CCL17 is shown with a green secondary structure and light green surface. Surface regions of close contact between the vCCI and CCL17 are colored purple.
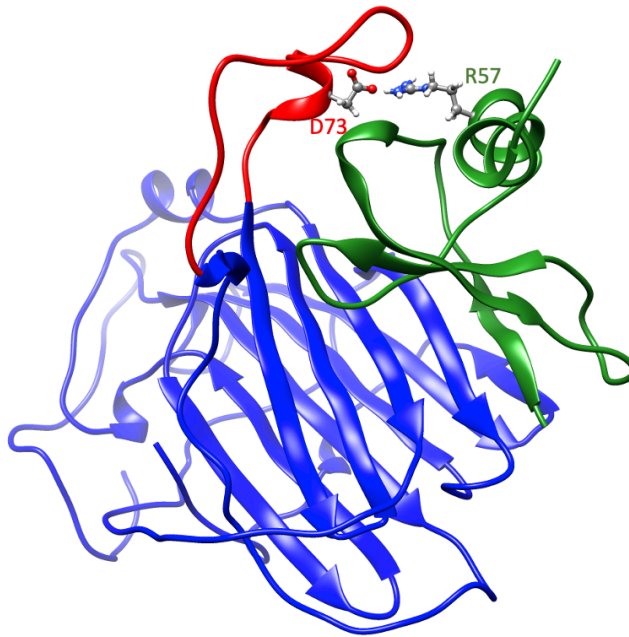
Supplementary Figure 2: Image of vCCI:CCL17 triple mutant after 800ns of molecular dynamics simulation showing the interaction between the chemokine R57 and the vCCI D73 (residues shown with space-filling model).